LIFE MODELING OF NOTCHED CM247LC DS NICKEL-BASE SUPERALLOY

A Thesis
Presented to
The Academic Faculty

by

Zachary Joseph Moore

In Partial Fulfillment
of the Requirements for the Degree
Master of Science in the
George W. Woodruff School of Mechanical Engineering

Georgia Institute of Technology
August 2008

LIFE MODELING OF NOTCHED CM247LC DS NICKEL-BASE SUPERALLOY

Approved by:

Dr. Richard W. Neu, Advisor
George W. Woodruff School of
Mechanical Engineering
Georgia Institute of Technology

Dr. David L. McDowell
George W. Woodruff School of
Mechanical Engineering
Georgia Institute of Technology

Dr. W. Steven Johnson
School of Materials Science and Engineering
Georgia Institute of Technology

Date Approved: 8 May 2008

ACKNOWLEDGEMENTS

The formulation of this thesis would not have been possible without the help and guidance of a multitude of individuals. Their support has augmented my graduate studies tremendously. I would like to express my deepest gratitude and heartfelt thanks to all involved in helping this project come to fruition.

I would like to thank my advisor, Dr. Richard W. Neu, for his support, guidance, and encouragement throughout my research. His efforts were essential to the completion of this thesis and it was an honor to work with him. I would also like to thank my committee members, Dr. David McDowell and Dr. Steven Johnson, for their time and efforts reviewing and improving the contents of this thesis.

The support and friendship of my coworkers, including Robert Kupkovits, Michael Hirsch, Kyle Webber, and Jeremy Dawkins, amongst others, was enormously helpful. The assistance of Cortney Crane and Mr. Robert Cooper has facilitated my research and their help is greatly appreciated.

This research was made possible by the financial support of Siemens Power Generation. I would like to thank all of the individuals at Siemens, especially Mr. Phillip Gravett, for their interactions and support.

Last and most importantly, I would like to thank my family. Specifically, I would like to express my gratitude for my fiancée, Nina Zobenica, whose love and support has helped me finalize this work and my parents and siblings for their years of encouragement throughout my studies.

TABLE OF CONTENTS

LIST OF TABLES

LIST OF FIGURES

LIST OF SYMBOLS

Experimental Measures, Conditions, and Symbols:

N	Number of cycles endured: [*cycles*]
N_i	Number of cycles to crack initiation: [*cycles*]
$N/2$	Half-life cycle: [*cycles*]
N_f	Number of cycles to failure: [*cycles*]
N_t	Transition life: [*cycles*]
T_n	Nominal test temperature: [$^\circ C$]
ΔT	Temperature range: [$^\circ C$]
t_{cc}	Total time for loading and unloading: [*s*]
t_{tc}	Total cycle time: [*s*]
t_{hc}	Compressive hold time: [*s*]
t_{ht}	Tensile hold time: [*s*]
a_i	Crack initiation depth: [*mm*]
P_0	Stabilized maximum load: [*kN*]
R	Load ratio
R_E	Ratio between tensile and compressive stiffness
E	Elastic modulus: [*MPa*]
E_T	Tensile stiffness: [*MPa*]
E_C	Compressive stiffness: [*MPa*]
v	Poisson's Ratio
$\Delta\varepsilon$	Local uniaxial strain range: [*MPa*]
ε_t	Total strain: $\left[\frac{mm}{mm}\right]$ or [%]

ε_{el}	Elastic strain: $\left[\frac{mm}{mm}\right]$ or $[\%]$
ε_{pl}	Plastic strain: $\left[\frac{mm}{mm}\right]$ or $[\%]$
$\dot{\varepsilon}$	Strain rate: $\left[\frac{1}{s}\right]$ or $\left[\frac{\%}{s}\right]$
ε^{t}	Elastic-plastic-creep strain: $\left[\frac{mm}{mm}\right]$ or $[\%]$
ε^{f}	Far field strain: $\left[\frac{mm}{mm}\right]$ or $[\%]$
ε^{et}	Elastic strain: $\left[\frac{mm}{mm}\right]$ or $[\%]$
ε^{p0}	Mechanically induced plastic strain: $\left[\frac{mm}{mm}\right]$ or $[\%]$
ε^{ct}	Creep strain: $\left[\frac{mm}{mm}\right]$ or $[\%]$
ε_{i}	Principal strains: $\left[\frac{mm}{mm}\right]$ or $[\%]$
e	Nominal strain: $\left[\frac{mm}{mm}\right]$ or $[\%]$
σ	Local stress: $[MPa]$
$\Delta\sigma$	Local uniaxial stress range: $[MPa]$
σ_{ar}	Fully reversed stresses in a notched specimen: $[MPa]$
σ_{m}	Mean stress: $[MPa]$
σ_{max}	Maximum uniaxial stress: $[MPa]$
σ^{t}	Elastic-plastic-creep stress: $[MPa]$
σ^{f}	Far field stress: $[MPa]$

σ_i	Principal stresses: $[MPa]$
S	Nominal stress: $[MPa]$
ΔS	Nominal uniaxial stress range: $[MPa]$
S_{ar}	Fully reversed stresses for smooth specimen: $[MPa]$
k_t	Theoretical elastic stress concentration factor
k_{tg}	Stress concentration factor based on gross cross-sectional area
k_{tn}	Stress concentration factor based on net cross-sectional area
k_f	Fatigue notch factor
k_σ	Stress concentration factor
k_ε	Strain concentration factor
$K_{t,\,eq}$	Equivalent stress concentration factor
ρ	Notch radius: $[mm]$
q	Notch sensitivity
α	Notch sensitivity empirical constant: $[mm]$
K_Ω	Strain energy density concentration factor
Ω_e	Total strain energy density at notch tip from linear elastic solution: $[MPa]$
Ω_f	Total strain energy density in the far field from linear elastic solution: $[MPa]$
K_{th}	Crack propagation threshold: $\left[MPa\sqrt{mm}\right]$
σ_0	Endurance limit: $[MPa]$
L	Length scale: $[mm]$

Microstructural Measures and Material Descriptions:

γ	Matrix phase of a Ni-base superalloy
γ'	Precipitate phase of a Ni-base superalloy
[001]	Primary crystallographic direction

Fatigue Analysis Variables:

σ'_f	Fatigue strength coefficient: [MPa]
b	Fatigue strength exponent
ε'_f	Fatigue ductility coefficient
c	Fatigue ductility exponent
n	Ramberg-Osgood strain hardening exponent
K	Ramberg-Osgood strength coefficient: [MPa]
n'	Ramberg-Osgood cyclic strain hardening exponent
K'	Ramberg-Osgood cyclic strength coefficient: [MPa]

Analytical Modeling Variables:

$\boldsymbol{\sigma}$	Elastic-plastic stress tensor: [MPa]
$\boldsymbol{\sigma}^*$	Elastic stress tensor: [MPa]
σ_{eq}	Equivalent stress based on the Hill criterion: [MPa]
$\boldsymbol{\sigma}_{dev}$	Deviatoric elastic-plastic stress tensor: [MPa]
$\boldsymbol{\sigma}^*_{dev}$	Deviatoric elastic stress tensor: [MPa]
$\boldsymbol{\varepsilon}$	Elastic-plastic strain tensor: $\left[\frac{mm}{mm}\right]$ or [%]
$\boldsymbol{\varepsilon}^*$	Elastic strain tensor: $\left[\frac{mm}{mm}\right]$ or [%]
$\boldsymbol{M}$	Tensor of Hill parameters
$\boldsymbol{H}$	Elastic compliance tensor: $\left[\frac{1}{MPa}\right]$
F, G, H, L, M, N	Hill parameters

E_R	Reference modulus: [MPa]
σ_0	Reference stress: [MPa]
α	Multiaxial R-O flow parameter
n	Multiaxial R-O flow exponent
$\boldsymbol{D}$	Elastic-plastic direction tensor
$\boldsymbol{D}^*$	Elastic direction tensor
σ_{YS}^{L}	Yield strength in the L direction: [MPa]
σ_{YS}^{T}	Yield strength in the T direction: [MPa]
σ_{YS}^{45}	Yield strength in a 45° direction: [MPa]

LIST OF ABBREVIATIONS

ANN	Artificial Neural Network
ASTM	American Society for Testing and Materials
CC	Continuously Cycled
CVP	Crystal Visco-Plasticity
DS	Directionally-Solidified
EDM	Electrical Discharge Machining
ESED	Equivalent Strain Energy Density
FCC	Face-Centered Cubic
FEA	Finite Element Analysis
HC	Hold in Compression
HCF	High Cycle Fatigue
HT	Hold in Tension
ISV	Internal State Variable
L	Longitudinal
LCF	Low Cycle Fatigue
MCF	Medium Cycle Fatigue
MNM	Multiaxial Neuber Model
MPRL	Mechanical Properties Research Laboratory
ODS	Oxide-Dispersion-Strengthened
PC	Polycrystalline
PDAS	Primary Dendritic Arm Spacing
R-O	Ramberg-Osgood

SC	Single-Crystal
SDAS	Secondary Dendritic Arm Spacing
SSR	Slow Strain Rate
SWT	Smith-Watson-Topper
T	Transverse
T/C	Thermocouple
TCD	Theory of Critical Distance
TF	Thermal Fatigue
TMF	Thermomechanical Fatigue
UMAT	User-defined Material Subroutine

SUMMARY

Directionally solidified (DS) nickel-base superalloys are used in high temperature gas turbine engines because of their high yield strength at extreme temperatures and strong low cycle fatigue (LCF) and creep resistance. Costly inspecting, servicing, and replacing of damaged components has precipitated much interest in developing models to better predict service life. Turbine blade life modeling is complicated by the presence of notches, dwells, high temperatures and temperature gradients, and highly anisotropic material behavior. This work seeks to develop approaches for predicting the life of hot sections of gas turbines blade material CM247LC DS subjected to LCF, dwells, and stress concentrations while taking into consideration orientation and notch effects. Experiments were conducted on an axial servo-hydraulic MTS® testing machine. High temperature LCF tests were performed on smooth and notched round-bar specimens in both longitudinal and transverse orientations with and without dwells. Experimental results were used to develop and validate an analytical life prediction model. An analytical model based on a multiaxial Neuber approach predicts the local stress-strain response at a notch and other geometric stress concentrations. This approach captures anisotropy through a multiaxial generalization of the Ramberg-Osgood relation using a Hill's type criterion. The elastic notch response is determined using an anisotropic elastic finite element analysis (FEA) of the notch. The limitations of the simpler analytical life-modeling method are discussed in light of FEA using an anisotropic elastic-crystal viscoplastic material model. This life-modeling method provides a quick alternative to

time demanding elastic-plastic FEA allowing engineers more design iterations to improve reliability and service life.

CHAPTER 1

INTRODUCTION

1.1 Background and Motivation

Land-based gas-powered turbines operate under extreme conditions as super-heated pressurized gases aimed at the blades which power the turbine that turns the compressor and electric generator. The turbine blades are exposed to extremely high temperatures (upwards 1300°*C*) and significant loads. For this reason, Ni-base superalloys are used for their high low cycle fatigue (LCF) resistance, creep resistance, and corrosion resistance. Operating efficiency increases as the combustion temperature rises, so gas turbine producers are continuously trying to develop improved superalloys that can be used at higher temperatures. This motivated the development of the directional solidification technique.

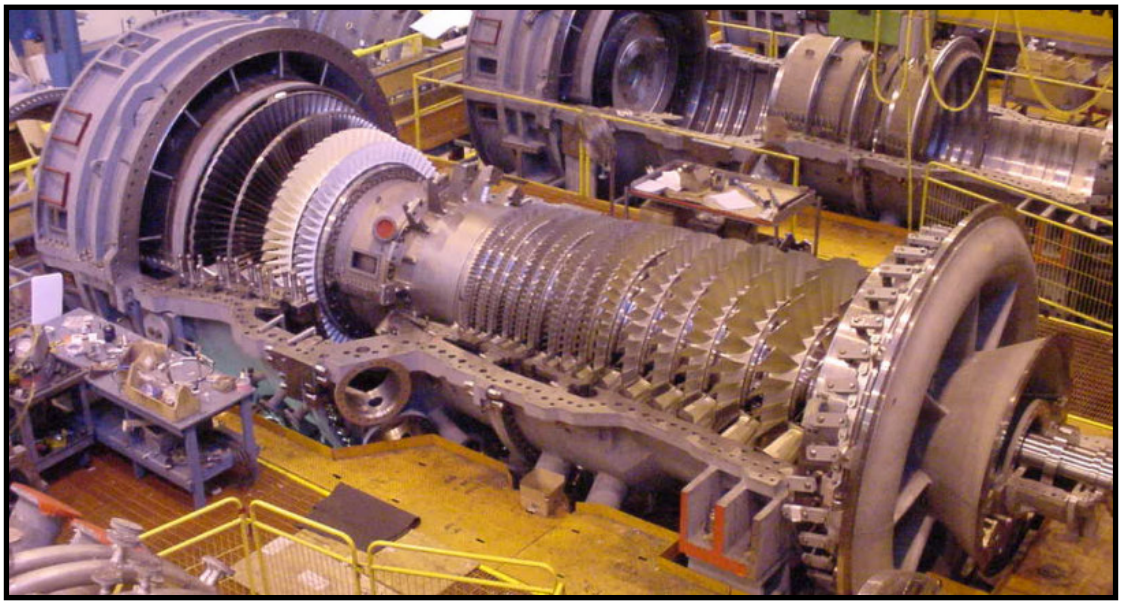

Figure 1.1: *Picture of a land-based gas turbine engine.*

Directionally solidified (DS) and single crystal (SC) Ni-base superalloys are replacing conventionally cast polycrystalline (PC) superalloys in many gas turbine components. Investment casting techniques have been modified to enhance the creep strength of Ni-base superalloys beyond what is achievable by means of purely altering the alloying chemistry. Directional solidification reduces the number of grain boundaries transverse to the primary loading axis, obtaining improved creep resistance and resulting in a highly anisotropic material. The low modulus in the longitudinal orientation also results in improved fatigue resistance in displacement-control conditions. CM247LC DS is one such alloy and is used by Siemens Power Generation in their land-based gas turbine engines.

Accurate material models are necessary to allow gas turbine manufacturers to better engineer their product by improving efficiency and reliability. Turbine components are exposed to a number of conditions that limit life. Efficiency demands have continued to increase operating temperatures. Blades and vanes are actively cooled via blowing air through cooling holes. These holes and the geometric irregularities of the blades act as stress concentrations. Start-up, operation, and shut-down sequences act as dwells in the components introducing a variety of time-dependent effects. CM247LC DS is a highly anisotropic material introducing orientation effects. All of these complexities amongst others must be dealt with in developing accurate models.

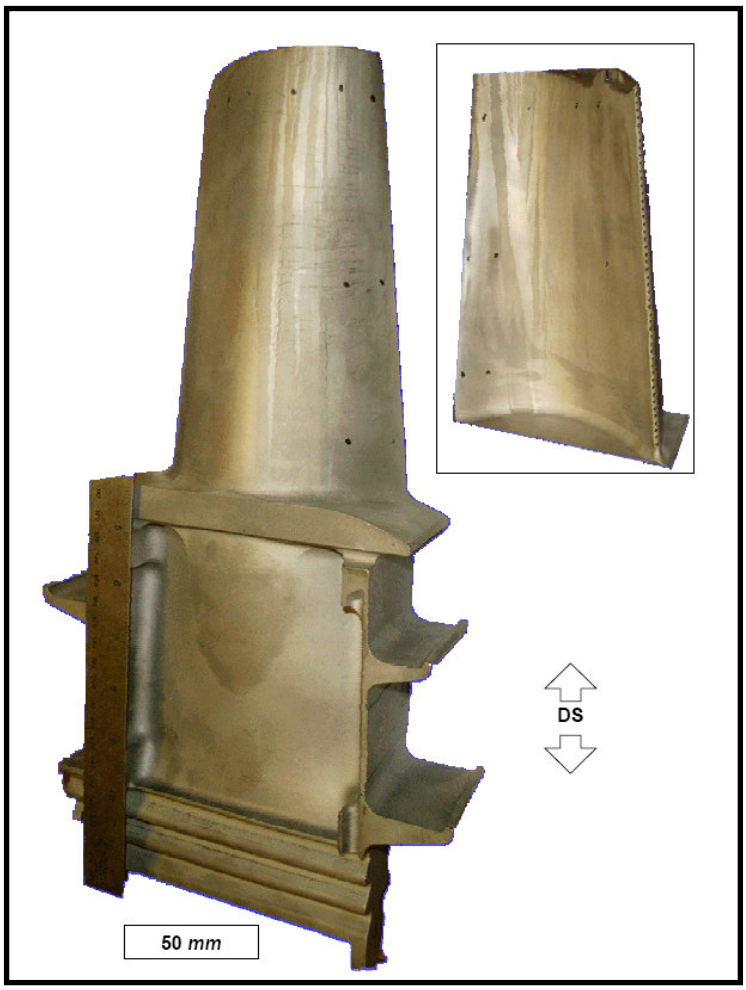

***Figure 1.2**: Suction and pressure sides of a DS gas turbine blade [1].*

1.2 Research Objectives

The goals of this research are:

(1) Perform experiments that define high temperature LCF, notch, and creep-fatigue behavior of CM247LC DS. Experiments are necessary to supplement existing material data to provide sufficient description of material performance and to develop and validate the analytical model

(2) Develop and validate a simplified analytical life model for CM247LC DS considering: high temperature LCF, dwells, stress concentrations, and orientation.

Full elastic-plastic simulations of complicated geometries are very computationally expensive. A simplified analytical approach is much quicker and can predict the material response accurately. A multiaxial Neuber-based approach will be used to predict the response at a notch while taking into consideration orientation, time-dependent effects, and temperature.

(3) Characterize the material and notch response using computational simulations. Numerical simulations performed on different notch geometries are used to validate analytical model predictions, characterize the notch response, and determine the limitations of the simplified approach.

1.3 Overview of the Thesis

The content and organization of this work is as follows. Chapter 2 contains a detailed literature review involving research in the area of DS alloys, multiaxial notch methods, and constitutive models. The experimental methods are discussed in Chapter 3 followed by experimental results and microscopy in Chapter 4. Chapter 5 discusses the analytical model. In Chapter 6, computational modeling is discussed. Afterwards, Chapter 7 and 8 contain the conclusions and recommendations for future studies.

CHAPTER 2

LITERATURE REVIEW

2.1 Application of DS Ni-base Superalloys

Nickel-based superalloys are used in hot sections of gas turbine engines because of their high strength and temperature resistance. In order for electric power generation companies to improve efficiency and reliability of gas turbine blades, advancement of durability and predictability of these materials is required. The performance of gas turbine engines is closely related to the low cycle fatigue (LCF) resistance and the creep capability of the material at increasingly higher temperatures. These advances come with improved alloy compositions and improved processing [2]. Ni-base superalloys possess excellent mechanical strength at high temperatures mostly due to γ' (Ni_3Al) hardening precipitates.

Difficult-to-machine components are made by investment casting, also known as "lost wax casting." Variations of the process produce three different grain patterns: polycrystalline (commonly referred to as equiaxed), directionally-solidified (DS), and single-crystal (SC) alloys. A polycrystalline grain pattern consists of a multitude of grains resulting in an isotropic cast. A directionally-solidified casting restricts the path of grain growth in the part. Directional solidification to produce turbine blades was first developed by Ver Snyder and Guard [3]. The single-crystal technique is the most challenging and most expensive method. In both DS and SC blades the [001] crystallographic orientation is set parallel to the blade principal axis. As this direction presents the lowest modulus of elasticity, lower thermal stresses are generated during

operation [4]. Elastic modulus as a function of orientation for a DS Ni-base superalloy is shown in Figure 2.1. As a result of grain orientation, DS and SC alloys are anisotropic. DS alloys are transversely isotropic because they possess a longitudinal and transverse direction. The multitude of randomly oriented columnar grains produce aggregate material properties for the transverse orientation. SC alloys are cubic. SC alloys have marginally better performance properties than DS alloys but are much more expensive because SC alloys have a lower casting yield than DS alloys [3].

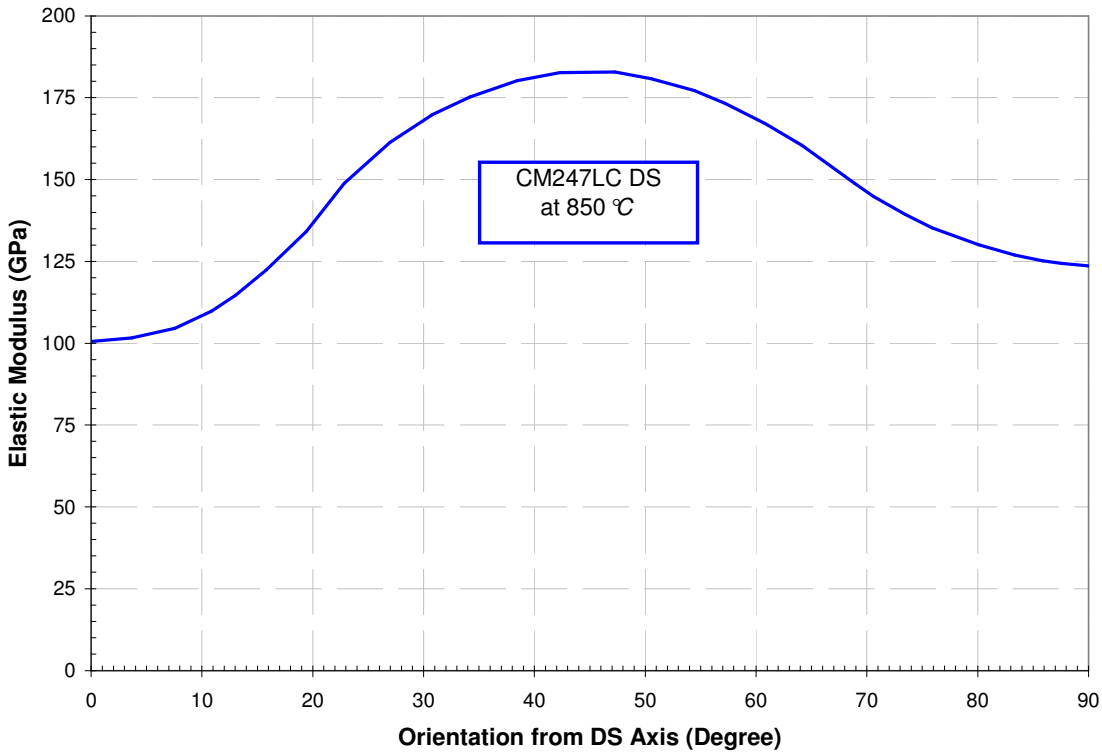

Figure 2.1: *Elastic modulus of CM247LC DS at 850°C for different orientations [5].*

Ni-base superalloys are dual-phase intermetallic consisting of a soft γ matrix phase and hard γ' precipitates. The γ matrix phase is face-centered cubic (FCC)

austenitic Ni solid solution with strengthening elements. The γ' precipitate phase is an ordered FCC super-lattice of Ni_3Al with both cuboidal and spherical shapes. This precipitate phase is the main strengthening mechanism in many Ni-based superalloys. Primary dendrite stems grow parallel to the solidification direction. Secondary and tertiary dendrite arms grow outward along [100] and [010] directions [1]. A depiction of dendrite geometry with primary dendritic arm spacing (PDAS) and secondary dendritic arms spacing (SDAS) is shown in Figure 2.2. The collection of long dendrites within grains act as a fracture toughening mechanism as propagating cracks are often deflected towards grain boundaries, resulting in significant out-of-plane crack extension [3].

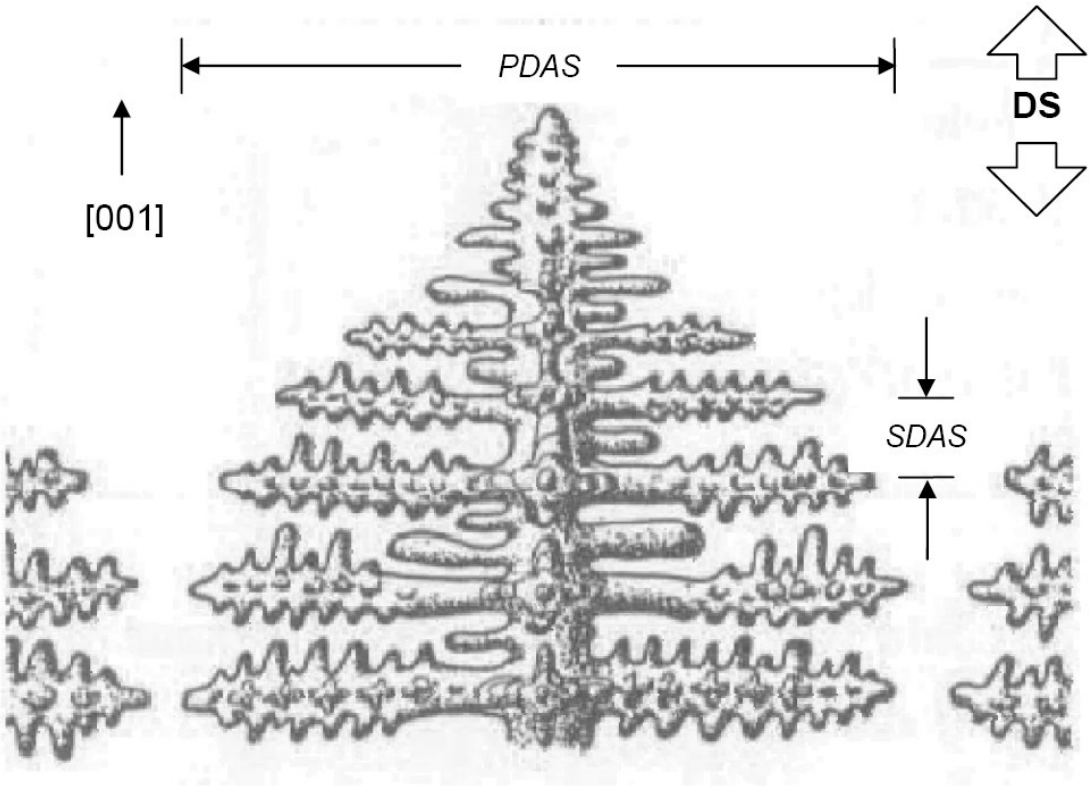

Figure 2.2: *Depiction of typical dendrite geometry [1, 6].*

2.2 Brief Description of CM247LC DS

CM247LC DS alloy is a directionally-solidified Ni-base superalloy produced by Cannon-Muskegon and used by Siemens Power Generation in land-based gas turbine blades [7]. Most CM247LC DS applications are in aeroturbines (22 blade and vane components servicing 11 engines) while 3 blade and vane airfoils are currently produced for 3 different industrial turbines. Current industrial turbine application development efforts involving components approaching 51-64 *cm* (20-25 *in*) in length will result in considerably more usage of the alloy [5].

This alloy contains a high volume fraction (~65%) of the reinforcing γ' phase [7, 8]. The alloy microstructure consists of columnar grains with boundaries parallel to the [001] growth direction, with an average width of 0.5 *mm* and a grain aspect ratio of about 10 [7].

CM247LC DS was derived from the base MarM247 and developed to improve DS castability, alloy ductility, fatigue strength, and carbide stability [5]. The material compositions of several DS Ni-base superalloys including CM247LC DS are shown in Table 2.1. In comparison to the base MarM247 composition, the carbon content of the alloy was reduced to avoid the formation of grain boundary carbides. Additionally, other elements such as B, Si, or Zr have also been reduced in composition in order to improve DS grain boundary cracking resistance without decreasing strength [9]. Some industrial turbine producers of natural gas fueled turbines have utilized CM247LC DS turbine blades and vanes in newly designed and up-rated turbines. When cast as large DS components (12-25 *in* long) the alloy exhibits superior castability, solution characteristics, and strength attainment. CM247LC DS has less chromium content than

some superalloys, but when natural gas is the predominant fuel, the material corrosion requirements are significantly less than those cases where low grade fuels are used [5]. The precipitation hardening results in an increase in yield strength at high temperatures. This is extremely beneficial to high temperature performance and is why superalloys are used in high temperature and mechanically demanding environments.

Table 2.1: *Chemical composition of several polycrystalline and DS casting alloys [5].*

First and Second Generation Polycrystalline and DS Casting Alloys
Chemical Composition by Weight Percent

	Al	B	C	Cb	Co	Cr	Hf	Mo	Re	Ta	Ti	W	Zr	Ni
IN 738 LC	3.6	0.01	0.01	0.7	8.4	16	-	1.7	-	1.7	3.4	2.5	0.05	Bal.
IN 939	1.9	0.01	0.15	1	19	22.5	-	-	-	1.4	3.7	2	0.1	Bal.
IN 792	3.4	0.015	0.14	-	9	12.7	1	2	-	4.2	4.1	4.2	0.05	Bal.
Renè 80	3	0.015	0.17	-	9.5	14	-	4	-	-	5	4	0.03	Bal.
MM 002	5.5	0.015	0.15	-	10	9	1.5	-	-	2.5	1.5	10	0.05	Bal.
CM 247 LC	5.6	0.015	0.07	-	9.2	8.1	1.4	0.5	-	3.2	0.7	9.5	0.015	Bal.
CM 186 LC	5.7	0.015	0.07	-	9	6	1.4	0.5	3	3	0.7	8	0.005	Bal.
MAR M 247	5.5	0.015	0.15	-	10	8	1.5	0.6	-	3	1	10	0.03	Bal.
GTD 111	3	0.01	0.1	-	9.4	14	0.15	1.5	-	3	5	3.7	0.01	Bal.

2.3 Prior Research on Forms of CM247LC DS

A great deal of research has been performed on CM247LC DS and other similar DS Ni-base superalloys in the past two decades. Advancements in technology and the popularity of DS and SC alloys resulted in great interest in this field of research. A greater understanding of the advanced materials is sought to better predict service lives and reliability. The hotter more extreme conditions turbine components can withstand, the more efficient the power generation process is. This provides significant monetary incentive for gas turbine companies to invest in research. DS and SC superalloys exhibit complex behavior that has been heavily investigated

Erickson and Harris (both from Cannon-Muskegon) [5, 10, 11] studied DS and SC superalloys for industrial gas turbine engines. The 1984 patent for CM247LC DS lists Harris as the alloy's inventor [12]. This study includes a great deal concerning

Larson-Miller plots and stress-rupture strength of CM247LC DS with comparisons to MarM247 demonstrating the superior performance of CM247LC DS. This comparison is extended to include SC, DS, and equiaxed superalloys. LCF data is provided for CM247LC DS at 0° (L), 90° (T), and 45° orientations and is compared to similar DS turbine alloys. LCF data at 850°*C* for CM247LC DS is shown in Figure 2.3. The 45° orientation possesses the shortest LCF life and has lives similar to equiaxed CM247LC.

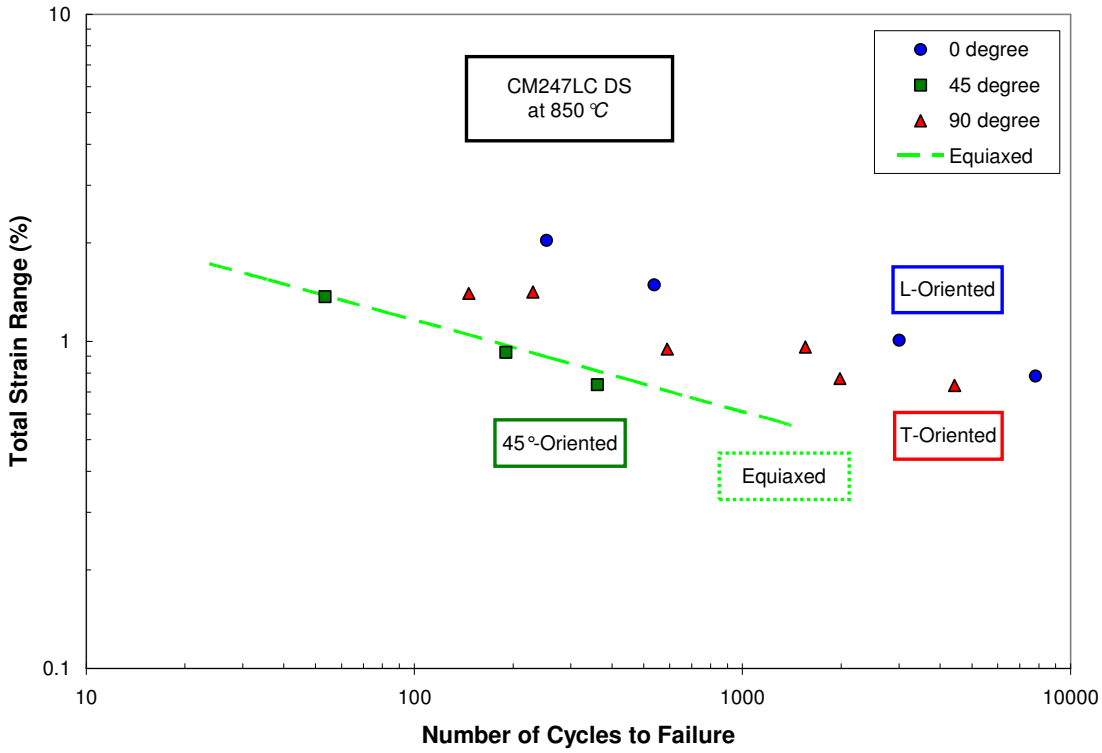

Figure 2.3: *LCF of CM247LC DS at 850°C as a function of specimen orientation [5].*

Eßer [13] gives an overview of DS of blades for industrial gas turbines. A multitude of material mechanical properties was obtained. CM247LC DS exhibited the highest values of tensile strength as it was calculated for a variety of temperatures

compared to IN6203 DS and IN792 DS. Yield strength as a function of temperature and orientation is shown in Figure 2.4. Creep rupture tests were performed on CM247LC DS as well. The material showed a higher creep rupture strength and ductility in the L orientation than the T orientation. The creep rupture strength was shown to be much higher than a conventionally cast version. Gas turbine blades are subjected to impacts by foreign objects during service so notch impact tests were performed on three Ni-base alloys. CM247LC DS outperformed other DS superalloys in this test because of its high ductility.

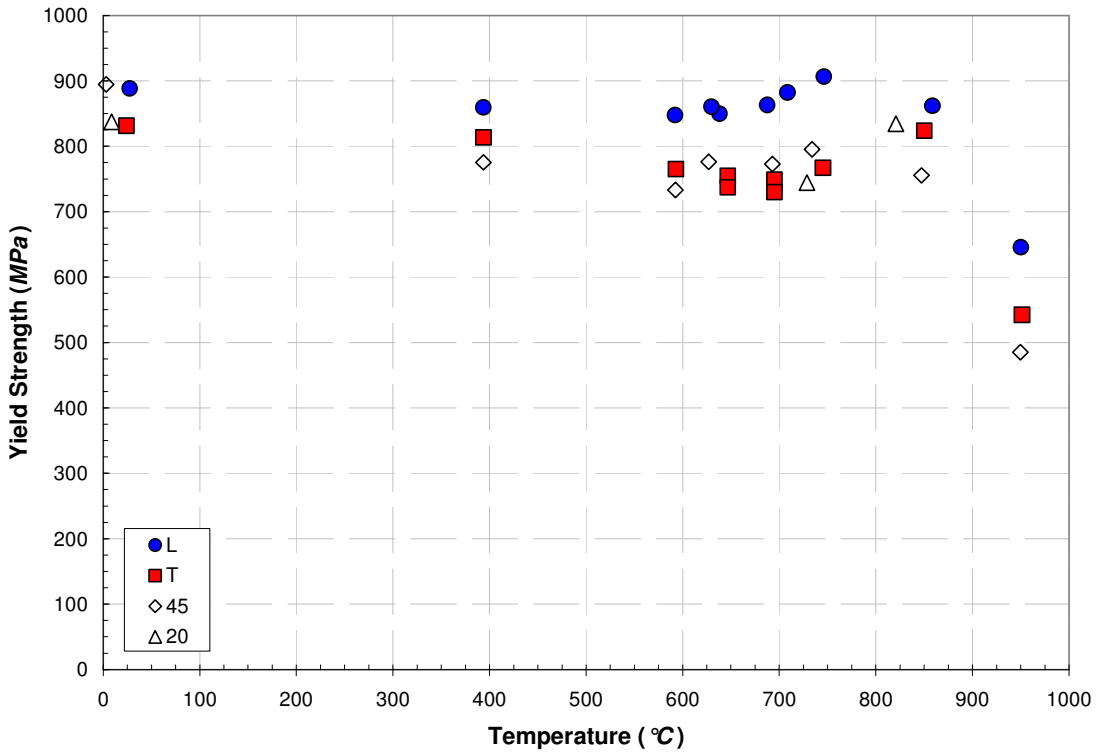

Figure 2.4: *Yield strength of CM247LC DS as a function of temperature and orientation [13].*

In 1996, Marchionni et al. [8] investigated the cyclic deformation of CM247LC DS by performing LCF tests and analyzing the cyclic stress response, LCF properties, and fatigue fracture process. The origin of failure under LCF is mainly related to the geometrical discontinuities on the specimen surface including: shrinkage pores, crevices created by oxidation effects, fracture of carbides located at the specimen surface, and indentations arising from sources like machining marks. Approximately 3% softening was seen until close to failure [7, 8]. LCF tested and as-received materials did not show a significant coarsening of the γ' particles during fatigue testing at 850°*C* and 950°*C*. Because only a small fraction of precipitates were sheared under conditions of strain-controlled LCF tests it is suggested that the dislocation networks which formed at the γ-γ' interface could impede other dislocations form penetrating the precipitates, thereby resulting in a stable cyclic stress response. Basquin and Coffin-Manson relationships fit the LCF data well. These constants are reported in Table 2.2. The fatigue failure mechanisms in Ni-base superalloy involve crack initiation at near-surface flaws. CM247LC DS exhibits superior fatigue resistance when compared to oxide-dispersion-strengthened (ODS) superalloys likely due to its higher ductility.

Table 2.2: *Basquin and Coffin-Manson constants for CM247LC DS [7, 8].*

Temperature (°*C*)	Grain Orientation	σ'_f (*MPa*)	b	ε'_f	c
850	L	176	0.15	0.075	0.68
950	L	140.7	0.17	0.13	0.75
950	T	99	0.17	0.048	0.69

Maldini et al. [7] evaluated the creep and fatigue properties of CM247LC DS, compared it to ODS MA6000 and IN738LC alloys, and analyzed the creep and fatigue

damage mechanisms. Creep results showed that CM247LC DS has a very short primary stage and that the majority of the creep life is tertiary creep. This dominant tertiary creep is associated with an increase of the flux of mobile dislocations with the strain due to an increase either of mobile dislocation density or the recovery rate. Creep-fatigue tests were also performed and it was observed that the cyclic stressing decreases the rupture life of the alloy and the rupture properties. The fatigue failure mechanism begins when a crack initiates along the slip bands that intersect the defects (e.g., pores on the specimen surface). Although the precise role of oxygen can not be specified, the diffusion of this element along the deformed zone could also facilitate shear decohesion while the pore induces a local stress concentration. Once the crack is formed, its subsequent growth direction is perpendicular to the applied load. CM247LC DS showed superior fatigue resistance and creep properties over IN738LC and ODS MA6000.

Blümm et al. [9] investigated the effect of grain orientation and grain size on the thermal fatigue (TF) behavior of CM247LC DS. TF is one of the life limiting factors for turbine blades and vanes because non-uniform expansion or contraction across the section of the blades produces transient thermal strain and stress fields during start-up and shut-down procedures. TF crack initiation life curves and mechanisms revealed that columnar grains perpendicular to the principal loading axis (T orientation) significantly reduced the TF crack initiation resistance. In the L orientation, crack propagation was mostly transgranular. In the T orientation, crack propagation was mostly intergranular. More cracks were observed in the T orientation because more grain boundaries perpendicular to loading direction were present. As a result of grain orientation a greater

crack propagation rate was observed in the T orientation. All cracks were oriented perpendicular to the principal loading direction.

In 1994, Vasseur and Rèmy [14] investigated the high temperature LCF and TMF of the ODS Ni-base superalloy MA 760 and compared to CM247 DS. They found that fatigue life is dependent on strain rate so there is an interaction of time-independent plasticity with time-dependent processes such as creep, oxidation, and microstructure. The cracks usually nucleated at grain boundaries and were transgranular. The weakness of the ODS superalloy's grain boundaries reduces the potential high temperature fatigue life and was shown to be inferior to the CM247 DS.

Engler-Pinto et al. [4] studied the interaction between creep and TMF of CM247LC DS. TMF and creep experiments were performed on the alloy. During tensile creep at 900°*C* the γ' precipitates on the alloy are rafted perpendicularly to the loading axis and this enhances inelastic strain during TMF cycling (i.e., pre-creeping decreases the TMF life). It was concluded that the modification of the γ-γ' structure should be considered as an additional parameter which shortens the TMF life. Pre-TMF cycling, however, has no effect on the creep rupture lifetime because its microstructure and thus its mechanical properties are not changed by pre-TMF cycling.

In 1992, Hasebe et al. [15] studied the similar alloy MarM247 DS, specifically the effect of solidification direction on cyclic constitutive relation and LCF resistance. The fatigue life of the 0° specimen was the largest, while the 45° specimen was the smallest and the 90° specimen falls in between, as shown in Figure 2.5. The transition fatigue life where plastic strain has the same amplitude as elastic strain appears to be less than 10 cycles, so the predominant role of the elastic strain on fatigue life can be understood from

the shortness of the transition fatigue life. The plastic strain range uniquely correlates the LCF life (i.e., plastic strain collapses the $\Delta\varepsilon$-N curve for all three orientations as shown in Figure 4.6a). Employing the plastic strain as a comparative parameter for predicting LCF life is difficult because the plastic strain range is an order smaller than the elastic strain range which introduces scatter. The stress range was also found to uniquely correlate fatigue life regardless of orientation as shown in Figure 4.6b. A constitutive relationship is based on writing Young's modulus as a function of orientation. This is then incorporated into a stress-strain relationship (e.g., Ramberg-Osgood) and used to predict fatigue life. Solidification direction has a significant effect on high temperature LCF and this difference is mainly due to the minimum stress amplitude in the more compliant orientations. The cyclic stress-strain relationship is relatively elastic so it follows that a cyclic constitutive equation taking into account the anisotropy of the Young's modulus predicted LCF life very well.

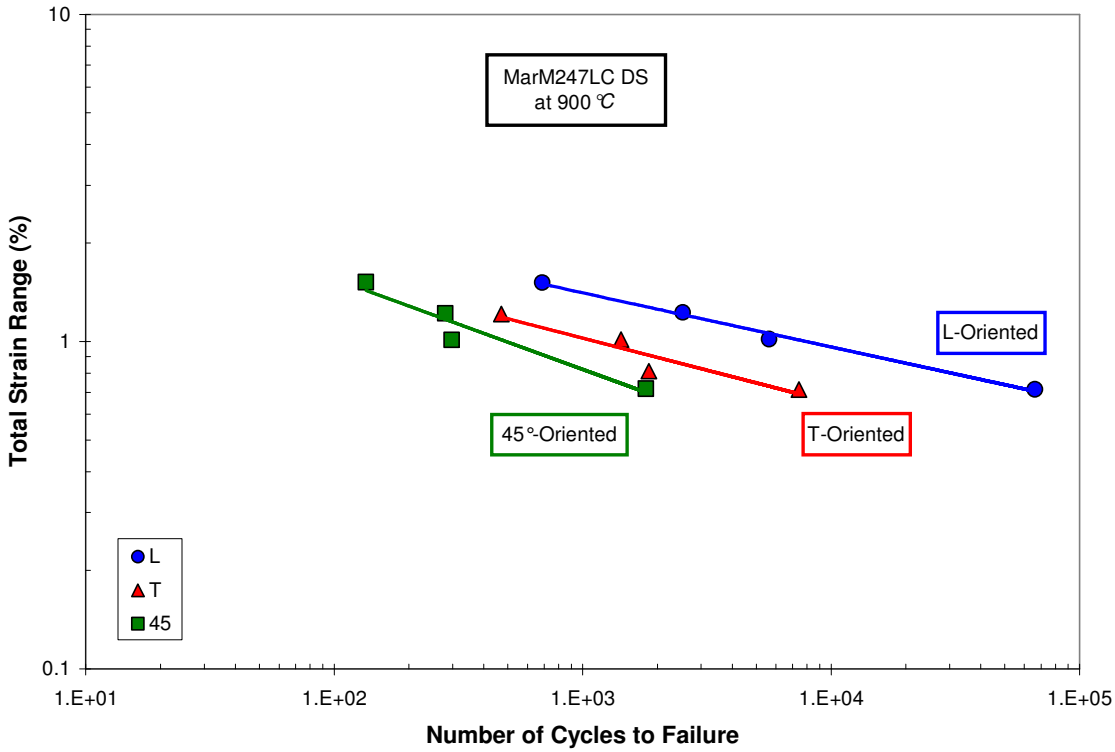

Figure 2.5: *LCF of MarM247LC DS at 900°C as a function of orientation [15].*

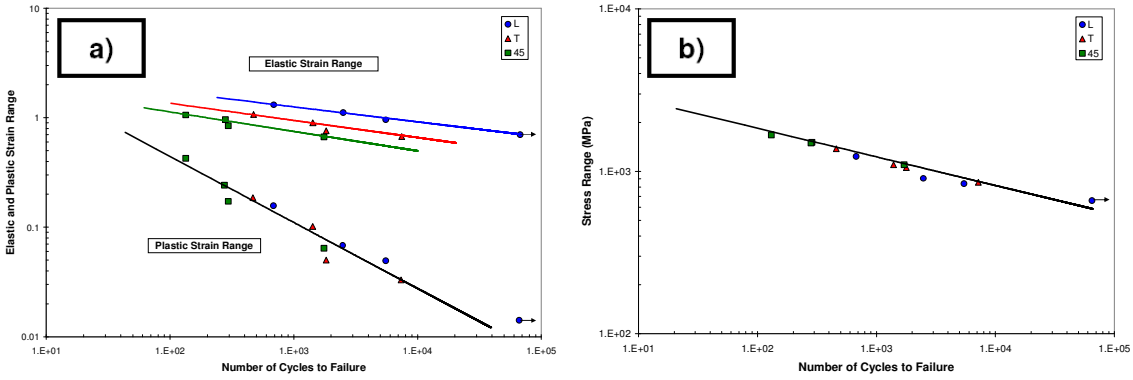

Figure 2.6: *Correlation of failure cycles of MarM247LC DS at 900°C with a) elastic and plastic strain ranges and b) stress range [15].*

Gordon [1] studied the crack initiation of DS GTD-111, a similar DS turbine alloy. This study included performing a multitude of experiments including LCF tests, creep-fatigue tests, TMF tests, and environmental tests. The investigation discussed the

orientation, mean strain, frequency, temperature, dwell, creep, and environmental effects on this particular DS superalloy. Numerical simulations using a crystal plasticity constitutive model developed by Shenoy et al. [16] were performed. A mechanistically-based crack initiation model was developed and discussed for the superalloy. Ibanez et al. [3] studied creep deformation and rupture behavior of GTD 111 DS. Creep deformation was modeled using a power law and the θ-projection approach. This alloy has a short primary stage and the majority of creep life is tertiary creep. Creep rupture behavior was modeled by using Larson-Miller parameter and Monkman-Grant relation. An artificial neural network (ANN) approach was also used. Fracture was seen to be exclusively transgranular under all conditions tested but fracture surfaces of L specimens at higher temperature showed more dimple fracture and those from the T direction at lower temperature showed a highly faceted character. Cracks nucleate in the interdendritic region probably at the interface between matrix and carbides or at porosity-type defects. The Monkman-Grant relationship, the Larson-Miller parameter, the θ-projection, and ANN successfully predicted the time to rupture usually within a factor of 1.5-2.

2.4 Stress Concentration Analysis

Classical Notch Analysis

The severity of a notch is characterized by the theoretical elastic stress concentration factor (sometimes referred to as the stress concentration factor) k_t. The

stress concentration factor is the ratio of the local notch stress (σ) to the nominal stress (S).

$$k_t = \frac{\sigma}{S} \tag{2.1}$$

Stress concentration factors are known for numerous common geometries and loading types [17]. The nominal stress can be selected based on gross or net cross-sectional area, resulting in stress concentration factors of k_{tg} and k_{tn}, respectively. For the purpose of this study, all stress concentrations are based on net cross-sectional area so k_t=k_{tn}. For three-dimensional problems, stress concentrations will change for different materials because Poisson's ratio impacts the multiaxial response. The relationship, however, is similar to the planar problem's

$$k_{ti} = \frac{\sigma_{i\max}}{S_{i\max}} \tag{2.2}$$

where i is the loading direction of interest.

For fatigue problems, k_t is often not an adequate measure of stress concentration's effect. Instead, a fatigue notch factor (k_f) is used [18, 19]. This factor relates fully reversed stresses for smooth specimen (S_{ar}) to the stresses in a notched specimen (σ_{ar}) for a particular fatigue life (N).

$$k_f(N) = \frac{S_{ar}(N)}{\sigma_{ar}(N)} \tag{2.3}$$

The fatigue notch factor describes the reduction in life as a result of the presence of a notch and is determined empirically from smooth and notched fatigue life data. Values of 10^6 and 10^7 *cycles* for N are most commonly used for k_f. When the notch has a large radius (ρ), k_f may be essentially equal to k_t. For small radii, k_f is usually considerably smaller than k_t. There are four commonly used explanations for this phenomenon: (1) materials are not sensitive to peak stress but to an average stress that acts over a finite region, (2) the statistical probability of a microstructural defect is reduced with extremely sharp notches, (3) the crack may start quickly in a sharply notched member but propagates slowly due to the rapidly decreasing stress outside of the notch, and (4) reversed yielding at the notch reduces the actual stress amplitudes at the notch. The concept of notch sensitivity (q) was developed to describe the relationship between k_t and k_f,

$$q = \frac{k_f - 1}{k_t - 1} \tag{2.4}$$

Many attempts have been made to estimate q and k_f. Peterson [17] used an empirical material constant (α) and notch radius (ρ) to describe q,

$$q = \frac{1}{1 + \frac{\alpha}{\rho}} \tag{2.5}$$

Another frequently used empirical formulation for q, known as the Kuhn-Hardrath formula [20], represents a simplification of an equation developed by Neuber,

$$q = \frac{1}{1 + \sqrt{\frac{\beta}{\rho}}} \tag{2.6}$$

where β is an alternative material constant.

One of the most commonly used approaches to approximating the response in the presence of stress concentrations is the approach introduced in 1961 by Neuber [21] known most commonly as Neuber's rule. Neuber showed that for a symmetrically notched prismatic body, the theoretical elastic stress concentration factor is given (approximately for other geometries) by the geometric mean of the stress and strain concentration factors (k_σ and k_ε, respectively), for the case of uniaxial (plane stress) loading,

$$k_t = \sqrt{k_\sigma k_\varepsilon} \tag{2.7}$$

The stress and strain concentration factors can be written in terms of local and nominal stress (σ and S, respectively) and strain (ε and e, respectively) components

$$k_\sigma = \frac{\sigma}{S} \qquad k_\varepsilon = \frac{\varepsilon}{e} \tag{2.8}$$

If fully plastic yielding (i.e., plastic deformation is unrestrained near notch root) does not occur and the nominal stress-strain response is elastic,

$$e = \frac{S}{E} \tag{2.9}$$

Substituting Eq. 2.8 and Eq. 2.9 into Eq. 2.7 gives,

$$k_t = \sqrt{\frac{\sigma}{S}\frac{\varepsilon E}{S}} \tag{2.10}$$

Finally, Neuber's rule can be written with nominal components on one side (right), and local components on the other (left),

$$\sigma\varepsilon = \frac{k_t^2 S^2}{E} \tag{2.11}$$

Using a stress-strain relationship (e.g., Ramberg-Osgood given in Eq. 2.12),

$$\varepsilon = \frac{\sigma}{E} + \left(\frac{\sigma}{K}\right)^{1/n} \tag{2.12}$$

the strain state can be substituted into the Neuber rule yielding an equation with only the local stress component unknown,

$$\frac{k_t^2 S^2}{E} = \frac{\sigma^2}{E} + \sigma\left(\frac{\sigma}{K}\right)^{1/n} \tag{2.13}$$

Solving Eq. 2.13 for σ and Eq. 2.12 for ε gives the local stress-strain for a nominal stress. For notches where k_t is unknown, finite element analysis can be used to obtain the elastic local stress response, σ^*, denoted here as a pseudo stress. Then Eq. 2.11 is written,

$$\sigma\varepsilon = \frac{\left(\sigma^*\right)^2}{E} \tag{2.14}$$

This can be rewritten so the product of the elastic-plastic stress and strain (σ and ε, respectively) is equivalent to the product of the elastic stress and strain (σ* and ε*, respectively).

$$\sigma\varepsilon = \sigma^*\varepsilon^* \tag{2.15}$$

In 1969, Topper et al. [22] was the first to extend this rule to cyclic loading. Each load reversal is modeled independently, creating a stabilized hysteresis loop using cyclically stabilized components (n' and K'). For fatigue analysis, k_f is commonly used instead of k_t because it accounts for size effects and for small notches k_t is unnecessarily conservative. The cyclic Neuber's rule is written as

$$\Delta\sigma\Delta\varepsilon = \frac{k_f^2 \Delta S^2}{E} \tag{2.16}$$

The cyclic Neuber rule can be then combined with a cyclic stress-strain relationship (e.g., R-O given in Eq. 2.17),

$$\frac{\Delta\varepsilon}{2} = \frac{\Delta\sigma}{2E} + \left(\frac{\Delta\sigma}{2K'}\right)^{1/n'} \tag{2.17}$$

yielding an equation with only one local component unknown,

$$\frac{k_f^2 \Delta S^2}{2E} = \frac{\Delta\sigma^2}{2E} + \Delta\sigma\left(\frac{\Delta\sigma}{2K'}\right)^{1/n'} \tag{2.18}$$

Another widely used method is based on the equivalent strain energy density (ESED) rule proposed by Molski and Glinka [23] in 1981. This method uses the full area underneath the stress-strain curve, the strain energy density, to calculate the local stress-strain history at a notch. This method is usually less conservative than the Neuber's rule alternative. Neuber's rule reduces to a triangular area underneath the stress-strain curve whereas Glinka's energy approach uses the total area, as illustrated in Figure 2.7. A similar equation can be written for Glinka's rule, assuming the material follows a R-O stress-strain relationship,

$$\frac{k_f^2 \Delta S^2}{4E} = \frac{\Delta\sigma^2}{4E} + \frac{\Delta\sigma}{n'+1}\left(\frac{\Delta\sigma}{2K'}\right)^{1/n'} \tag{2.19}$$

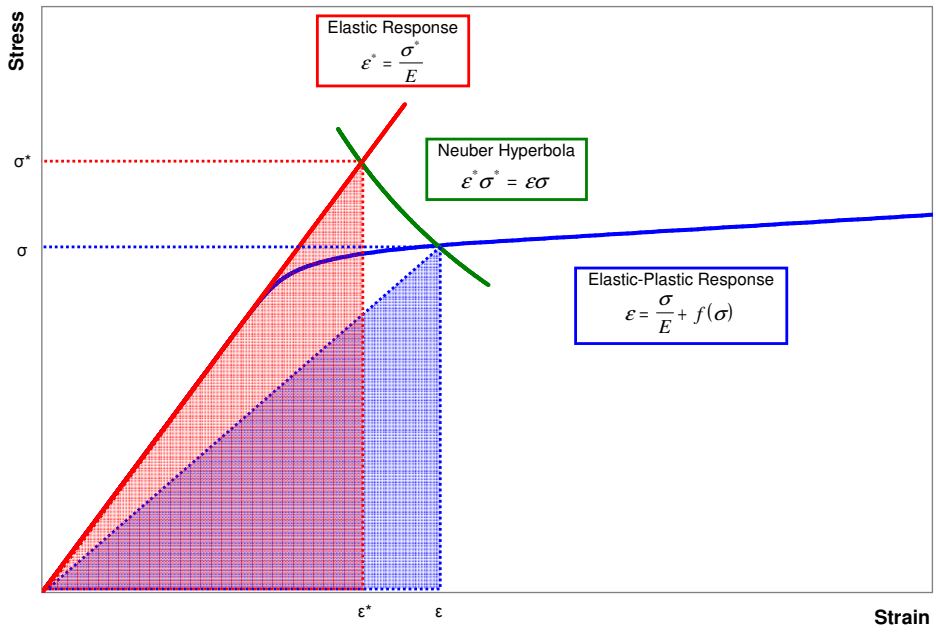

Figure 2.7: *Geometric interpretation of Neuber's rule in one dimension [2, 21].*

In the treatment above, plane stress was assumed, resulting in a uniaxial state of stress at the notch. If the notch radius is small compared to the thickness, the out-of-plane stress component is not zero. This is particularly true of axisymmetric geometries where ρ is small compared to the dimensions of the shaft. A detailed development of the plane strain approach is covered in Dowling [19].

Multiaxial Notch Analysis

In 1985, Hoffmann and Seeger [24] applied the Neuber method to multiaxial stress-strain states of isotropic materials by assuming proportional load conditions. They

showed that well known approximation formulas valid for uniaxial situations can be extended to multiaxial stress states in case of proportional loading by replacing the uniaxial quantities by equivalent quantities including equivalent strain (ε_{eq}), equivalent stress (σ_{eq}), and equivalent stress concentration factor ($K_{t,\,eq}$). The equivalent stress concentration factor is written in terms of the nominal stress (S) and theoretical elastic equivalent notch stress (σ_{eq})

$$K_{t,eq} = \frac{\sigma_{eq}}{S} \tag{2.20}$$

The multiaxial Neuber rule can then be written in terms of equivalent components

$$\sigma_{eq}\varepsilon_{eq} = \frac{K_{t,eq}^2 S^2}{E} \tag{2.21}$$

A material law written in terms of multiaxial variables is substituted into the Neuber rule for either equivalent stress or strain reducing the number of unknowns to one. With this substitution, it is possible to solve for both equivalent stress and strain. To correlate equivalent components to the principal stresses (σ_i) and strains (ε_i), the flow rule of Prandtl-Reuss is used to relate plastic strain increments $d\varepsilon_i^p$ to the deviatoric stresses σ_i^{dev}

$$d\varepsilon_i^p = \frac{3}{2}\frac{d\varepsilon_{eq}^p}{\sigma_{eq}} \bullet \sigma_i^{dev} \tag{2.22}$$

These equations represent the exact solution for isotropic hardening under the assumption of von Mises' yield criterion. If the ratio between the deviatoric stress components remains constant during loading, the Prandtl-Reuss law reduces to Hencky's rule, which assumes the plastic strains to be a function of the deviatoric stresses

$$\varepsilon_i^p = \frac{3}{2}\frac{\varepsilon_{eq}^p}{\sigma_{eq}} \bullet \sigma_i^{dev} \tag{2.23}$$

The ratio between deviatoric stress components does not change substantially due to the geometric constraint prevailing in the vicinity of the notch; Hencky's rule gives approximate results with sufficient accuracy. Hencky's equations can be transformed and all the principal stresses and strains at the notch root can be calculated.

Köttgen et al. [25] discusses pseudo stress and strain based approaches to multiaxial notch analysis. Pseudo stress and pseudo strain are used to describe the linear elastic solution at the notch. They are fictitious quantities that are only used as an intermediate values in computation. The mathematical nature of Hill's yield criterion imposes certain restriction on the type of loading which may be analyzed. When a certain local stress component is activated by more than one external load, the mixed terms are missing in the anisotropic structural yield surface based on Hill's criterion. The proposed models were validated by proportional and non-proportional FE simulations.

In 2003, Mücke and Bernhardi [2] extended Neuber's rule to fully multiaxial loading by developing a tensorial generalization of both Neuber's rule and the Ramberg-Osgood stress-strain relationship. This model was applied to directionally-solidified nickel-based superalloys with transverse isotropy and single crystal materials with cubic anisotropy. The multiaxial generalization followed that of Hoffmann and Seeger [24],

$$\sigma_{eq}^{*}\varepsilon_{eq}^{*} = \sigma_{eq}\varepsilon_{eq} \tag{2.24}$$

Written in tensorial form, the corresponding formulation for anisotropic materials [2],

$$\boldsymbol{\sigma}^{\mathbf{*dev}} : \boldsymbol{\varepsilon}^{*}\left(\boldsymbol{\sigma}^{\mathbf{*dev}}\right) = \boldsymbol{\sigma}^{\mathbf{dev}} : \boldsymbol{\varepsilon}\left(\boldsymbol{\sigma}^{\mathbf{dev}}\right) \tag{2.25}$$

where strains of the elastic and the elastic-plastic solution are related to the deviatoric stresses. The use of deviatoric stresses comes from Hoffman and Seeger's [24] use of Hencky's rule which express plastic strains as a function of deviatoric stresses and equivalent stress and strain components. Anisotropic materials require a generalization of the Ramberg-Osgood (R-O) relation for the multiaxial anisotropic case. This is done by using an anisotropic equivalent stress (σ_{eq})

$$\sigma_{eq} = \sqrt{\boldsymbol{\sigma}^{\mathbf{dev}} : \mathbf{M} : \boldsymbol{\sigma}^{\mathbf{dev}}} \tag{2.26}$$

which is based on the Hill criterion. $\boldsymbol{M}$ is a tensor of Hill parameters. The multiaxial Ramberg-Osgood law for anisotropic materials can be written as

$$\boldsymbol{\varepsilon} = \mathbf{H} : \boldsymbol{\sigma} + \frac{\alpha}{E_R}\left(\frac{\sigma_{eq}}{\sigma_0}\right)^{n-1} \mathbf{M} : \boldsymbol{\sigma}^{\mathbf{dev}} \tag{2.27}$$

Elastic anisotropy is represented by the compliance ***H*** whereas the plastic anisotropy is represented by the anisotropy tensor ***M***. In the same manner as the classical Neuber approach, the Neuber rule and the stress-strain relationship, both now generalized to the multiaxial case, can be combined to formulate the constitutive model based on a multiaxial Neuber rule that states

$$\boldsymbol{\sigma}^{*\mathbf{dev}} : \boldsymbol{\varepsilon}^{*}\left(\boldsymbol{\sigma}^{*\mathbf{dev}}\right) = \boldsymbol{\sigma}^{\mathbf{dev}} : \boldsymbol{\varepsilon}\left(\boldsymbol{\sigma}^{\mathbf{dev}}\right) \tag{2.28}$$

Time-Dependent Notch Analysis

In 1978, Chaudonneret [26] suggested that Neuber's rule could be expressed in its differential form as long as the applied stress increases monotonically and is a continuous function of time. Chaudonneret and Culie [27] demonstrated that the differential form of Neuber's rule could be successfully used to predict the notch root stresses and strains in creeping bodies under static and cyclic loading.

In 1984, Kurath [28] utilized a modified form of Neuber's rule to simulate the notch root stress-strain time-dependent behavior in components made of titanium, and acceptable fatigue life predictions were obtained.

Moftakhar et al. [29] proposed an extension of Neuber's rule to estimate creep induced multiaxial strains and stresses at the notch. The assumption was made that strain

energy density at the notch tip does not change when going from a linear elastic solution (σ^* and ε^*) to an elastic-plastic solution (σ and ε) to a time-dependent elastic-plastic-creep solution (σ^t and ε^t).

$$\sigma^* \varepsilon^* = \sigma\varepsilon = \sigma^t \varepsilon^t \tag{2.29}$$

This assumption may only be valid for cases where the deformation is strictly localized around the point of stress concentration. When there is non-localized creep deformation, Moftakhar et al. [30] suggested that the total strain energy density changes occurring in the far field produce similar but magnified effects at the notch tip. For this reason, a total strain energy density concentration factor (K_Ω) was used for a measure of this magnification [29],

$$K_\Omega = \frac{\Omega^e}{\Omega^f} = \frac{\sigma^* \varepsilon^*}{\sigma^f \varepsilon^f} \tag{2.30}$$

where Ω_e is the total strain energy density at the notch tip obtained form a linear elastic analysis and Ω_f is the total strain energy density at a predefined point in the far field also obtained from the linear elastic solution.

In 1998, Harkegard and Sorbo [31] reformulated Chaudonneret's model to predict creep stresses and strains in notches under constant nominal stress and strain. The complexity of Chaudonneret's model was reduced.

Nuñez and Glinka [32] introduced a method for the estimation of time-dependent strains and stresses in notches in 2004. This method uses a simplified analytical

approach in order to reduce the complexity of the model and it works for local and non-localized creep. When creep is localized, Moftakhar's relationship between linear elastic and time-dependent elastic-plastic solution can be used,

$$\sigma^* \varepsilon^* = \sigma\varepsilon = \sigma^t \varepsilon^t \tag{2.31}$$

The time-dependent strain can be decomposed into elastic (ε^{et}), mechanically induced plastic (ε^{p0}), and creep (ε^{ct}) contributions,

$$\varepsilon^t = \varepsilon^{et} + \varepsilon^{p0} + \varepsilon^{ct} \tag{2.32}$$

Combining Eq. 2.31 and Eq. 2.32 gives,

$$\sigma^* \varepsilon^* = \sigma^t \varepsilon^{et} + \sigma^t \varepsilon^{p0} + \sigma^t \varepsilon^{ct} \tag{2.33}$$

If ε^{p0} is considered constant during the hold time period, then differentiating Eq. 2.33 with respect to time gives,

$$0 = \sigma^t \dot{\varepsilon}^{et} + \dot{\sigma}^t \varepsilon^{et} + \dot{\sigma}^t \varepsilon^{p0} + \sigma^t \dot{\varepsilon}^{ct} + \dot{\sigma}^t \varepsilon^{ct} \tag{2.34}$$

The elastic strain rate is defined as $\dot{\varepsilon}^{et} = \dot{\sigma}^t / E$. In incremental form this becomes,

$$0 = \frac{2}{E}\frac{\Delta\sigma^{t_n}}{\Delta t_n}\sigma^{t_{n-1}} + \frac{\Delta\sigma^{t_n}}{\Delta t_n}\varepsilon^{c_n} + \frac{\Delta\sigma^{t_n}}{\Delta t_n}\varepsilon^{c_n} + \frac{\Delta\varepsilon^{c_n}}{\Delta t_n}\sigma^{t_{n-1}} \tag{2.35}$$

The decrement of stress due to creep thus becomes,

$$\sigma^{t_n} = \frac{-\sigma^{t_{n-1}}\Delta\varepsilon^{c_n}}{\frac{2}{E}\sigma^{t_{n-1}} + \varepsilon^{p0} + \varepsilon^{c_n}} \tag{2.36}$$

As expected, the stress increment ($\Delta\sigma^{t_n}$) is negative because of stress relaxation at the notch tip induced by creep. The increment of creep strain, $\Delta\varepsilon^{c_n}$, can be directionally obtained from a creep law (e.g., the power law proposed by Norton [33] given in Eq. 2.37),

$$\dot{\varepsilon}^c(\sigma,t) = A\sigma^{\alpha}t^{\beta} \tag{2.37}$$

where A, α, and β are temperature-dependent material constants. The incremental form of this creep law can be written as

$$\Delta\varepsilon^{c_n} = \Delta t_n \dot{\varepsilon}^c(\sigma,t) \tag{2.38}$$

For non-localized creep, a similar formulation is used but with an additional term including a strain energy density concentration factor (K_Ω)

$$\sigma\varepsilon + K_{\Omega}\Omega^{cf} = \sigma^{t}\varepsilon^{t} \tag{2.39}$$

Here, Ω_{cf} is the total strain energy density contributed as a result of the local and the far field creep given as

$$\Omega^{cf} = \sigma^{f}\varepsilon^{cf} \tag{2.40}$$

where σ^{f} is the far field stress and ε^{cf} is the total creep in the far field.

Non-Local Methods

Taylor [34] summarizes the methodology of the collection of theories known as the theory of critical distances (TCD). The theory was first proposed in 1958 by Neuber [35] when he proposed that the controlling parameter should be the elastic stress averaged in some critical volume surrounding the stress concentration. Modern theories use a length scale (L), which is a parameter with the dimensions of length that is incorporated into the theoretical model. For fatigue problems, a commonly used length scale can be written in terms of the crack propagation threshold (K_{th}) and fatigue limit (σ_0), both determined at the same load ratio (R) as the component being assessed,

$$L = \frac{1}{\pi}\left(\frac{K_{th}}{\sigma_0}\right)^{2} \tag{2.41}$$

For metal fatigue, L can be related to the length of non-propagating cracks. For example, Eq. 2.41 uses the size of a non-propagating crack in a smooth specimen as the characteristic length. Alternatively, some models use physical lengths related to the microstructure of the material. There are four main types of TCD: 1) the point method, 2) the line method, 3) the imaginary crack method, and 4) finite fracture mechanics. The first two methods are stress-based approaches and the latter two are fracture mechanics based approaches.

Dowling [36] derived an expression for the characteristic length by analyzing cracks growing from a circular hole in an infinite plate. When the crack is small compared to the hole's radius, the solution is the same as for a surface crack in an infinite body except for the stress being amplified by the stress concentration factor,

$$K_{short} = 1.12 k_t S \sqrt{\pi l} \tag{2.42}$$

where l is the crack length measured from the hole surface, S is the nominal stress, and K_{short} is the stress intensity factor for the short crack. When the crack has grown far from the hole, the solution is the same as for a single long crack of length a that includes both the notch and crack,

$$K_{long} = f(g) S \sqrt{\pi a} \tag{2.43}$$

where *f(g)* depends on the specific geometry of the component and K_{long} is the stress intensity factor for a long crack. The transition length is determined by setting the short crack and long crack solutions equal to each other,

$$L = \frac{c}{\left(\frac{1.12k_{tg}}{f(g)}\right)^2 - 1} \tag{2.44}$$

where c is the notch depth. The resulting values of L are typically in the range of 0.1ρ to 0.2ρ.

Susmel and Taylor [37] discuss how TCD can be applied to predicting the fatigue lifetime of notched components in the medium cycle fatigue regime (MCF). TCD was originally devised to address the high cycle fatigue (HCF) problem but it can be extended into the MCF regime. In order for TCD to be applied to MCF regime, the material characteristic length (L) is a function of the number of cycles to failure. One method estimates $L(N_f)$ considering material properties defined at the two extremes, static failure and the fatigue limit. An alternative approach determined the $L(N_f)$ relationship by means of two calibration fatigue curves, one created by testing smooth specimens and the other by testing notched specimens. The study demonstrated that TCD could be extended to the MCF regime.

In 2005, Bellett et al. [38] extended the use of TCD to 3D geometry using a variety of approaches. The authors showed that for certain types of 3D stress concentrations, the fatigue prediction methods, both elastic-plastic analysis and linear-elastic approaches, gave highly conservative results. It was expected that the highly

stressed material in 3D stress concentrations be much smaller when compared to an equivalent 2D notch geometry. An area method and volume method were used to allow for this effect, but it was found that predictions from volume method were just the same as from point method, line method, and area method. The more complicated volume method and area method do not result in a significant improvement over the simpler point method and line method, and that the slight increase in accuracy is not worth the additional computational complexity.

Mücke and Kiewel [39] addressed a non-local concept for fatigue life prediction of notched components with a method that explicitly accounts for stress and strain gradients. The method was developed from cyclic test data of 1.5CrNiMo but also revalidated using the Nickel-based superalloy MarM247 CC, both showing good agreement. For each notch radius, the relation between local strain amplitude and lifetime was approximately linear on a log-log scale. For this reason a Coffin-Manson type relation was used

$$\frac{N}{N_0} = C(\rho)\varepsilon_a^{n(\rho)} \tag{2.45}$$

where N is the life of a notched specimen, N_0 is the life of a smooth specimen, ρ is the notch radius, and ε_a is the local strain amplitude. Both Coffin-Manson parameters are functions of notch radius and thus implicitly on the strain gradient in the notch. FEA was performed to obtain the strain gradients. It was noticed that even for elastic-plastic behavior the relation between strain amplitude and strain gradient ($\nabla\varepsilon$) can be approximated by a linear relation

$$\nabla\varepsilon = a(\rho)\varepsilon_a \tag{2.46}$$

The relative strain gradient is defined as $\chi_\varepsilon = \nabla\varepsilon / \varepsilon_a$. Therefore, the Coffin-Manson parameters can be expressed in terms of χ_ε instead of ρ. C is written as a linear function of the form, $g(\chi_\varepsilon) = 1 + d\chi_\varepsilon$ and the exponent n has a much larger influence on cyclic life requiring a quadratic function of the form, $f(\chi_\varepsilon) = a\chi_\varepsilon^2 + b\chi_\varepsilon$. These can be substituted into a Coffin-Manson type equation

$$\frac{N}{N_0} = (1 + d\chi_\varepsilon)\varepsilon_{\max}^{f(\chi_\varepsilon)} \tag{2.47}$$

where a, b, and d are constants determined from notched specimen fatigue tests of multiple notch geometries. For MarM247 CC Ni-base superalloy, a stress-based approach is used instead

$$\frac{N}{N_0} = (1 + d'\chi_\sigma)\varepsilon_a^{f(\chi_\sigma)} \tag{2.48}$$

with the polynomial function fit of the exponent of the form $f(\chi_\sigma) = a'\chi_\sigma^2 + b'\chi_\sigma$ and relative local stress gradient $\chi_\sigma = \dfrac{\nabla\sigma}{\sigma_a}$.

The critical plane approach is a method commonly used to assess the plane on which damage and cracking may occur in multiaxial fatigue problems. The critical plane approach to multiaxial fatigue life estimation involves two steps: (1) identification of the orientation of the plane which represents the critical site in the material for the onset of damage based on some criterion and (2) estimation of the number of cycles to initiate a fatigue crack as a function of the magnitude of the parameter describing the critical plane loading [40]. The criterion which the onset of fatigue damage is based is referred to as a critical plane parameter. These parameters can be as simple as maximum normal/shear stress/strain or some combination of criterions. Table 2.3 summarizes common critical plane parameters.

Table 2.3: *Examples of common multiaxial critical plane parameters [41, 42].*

Parameter	Description
Maximum shear stress range	SSR = $\Delta\tau_{max}$ Where $\Delta\tau_{max}$ is the maximum shear stress range
Socie's parameter	$\text{SOC} = \frac{\Delta\gamma}{2} + \frac{\Delta\varepsilon_n}{2} + \frac{\sigma_n^{\max}}{2E}$ Where $\Delta\gamma$ is the shear strain range, $\Delta\varepsilon_n$ is the normal strain range, and $\Delta\sigma_n$ is the normal stress range.
Findley's parameter	FIN = $\tau_a + k\sigma_{max}$
Fatemi-Socie-Kurath parameter	$\text{FSK} = \gamma_a\left(1 + k\left(\frac{\sigma_n^{\max}}{\sigma_y}\right)\right)$
Walls parameter	$\text{Walls} = 50\gamma_{\max}\varepsilon_{\max}\left(\frac{\pi}{\arctan\left(\gamma_{\max}/\varepsilon_{\max}\right) + \pi/2}\right)^{0.5}$
Chu-Conle-Bonnen parameter	CCB = $2\gamma_a\tau_{max} + \varepsilon_a\sigma_{max}$
McDiarmid parameter	McD = $\tau_a + k\sigma_{max}$
Smith-Watson-Topper parameter	SWT = $\varepsilon_a\sigma_{max}$

Naik et al. [42] explains the application of critical plane fatigue parameters on single crystal nickel-based superalloys. Single crystals deform by shearing along {111} planes which are commonly referred to as octahedral planes. Under fatigue loading, cyclic stress produces alternating slip reversals on the critical slip systems which eventually lead to crack initiation. A critical plane fatigue modeling approach is suited for this type of fatigue failure mechanism. Non-local critical plane approaches are achieved by averaging the parameters over a prescribed volume in a similar manner as the VM. Slip, damage, and crack initiation occur over finite distances, making a non-local critical plane approach physically realistic.

Influence of Microstructure at Notches

As noted earlier, the value of k_f and hence the critical volume for non-local analysis can depend on microstructure. Recently there have been some efforts to assess this effect.

The role of microstructure in notch roots for Ni-base superalloys has been explored by Tjiptowidjojo et al. [43]. The microstructural characteristics investigated in this study are grain size distribution and primary, secondary, and tertiary γ' volume fractions and size distributions. An ANN was used to inform the dependence of material parameters in an internal state variable cyclic viscoplasticity model. Simulations included dwell periods at peak strain that resulted in stress relaxation. Simulations showed that finer grain size had a higher flow stress and greater resistance to mean stress relaxation. An increased creep resistance was seen in one microstructure due to the influence of the secondary γ' precipitates in resisting inelastic flow at high temperatures.

The simulations indicated that it is more desirable to increase the number density of small secondary γ' precipitates to resist primary creep deformation associated with cyclic stress relaxation. There is a pronounced effect of microstructure on mean stress relaxation which may impact fatigue life.

The effects of nonmetallic inclusions on LCF in DS nickel-base superalloys was studied by Shenoy et al. [44]. The effects of loading parameters and microstructural parameters on local cyclic plasticity at microstructure-scale notches were evaluated. SEM analysis revealed the two-phase microstructure and many plate-like carbide inclusions. The inclusions are $M_{23}C_6$ and M_6C type carbides with a volume fraction of 1-2%. A high volume of carbides was observed along the fracture surface. Surfaces of longer cracks are surrounded by a thin layer of oxide (~20 μm) and a gamma prime precipitate-free zone (~30 μm), suggesting that oxidation might also play a role in crack propagation at high temperatures. Appreciable casting pores are another possible site for LCF crack formation but were not observed in the material. A framework is introduced for estimating crack initiation in the presence of hard inclusions in DS Ni-base superalloys.

2.5 Computational Modeling

A detailed crystal plasticity model for DS Ni-based superalloy GTD-111 has been developed by Shenoy et al. [16]. DS GTD-111 is a similar turbine superalloy used in land-based gas turbine engines. The crystal plasticity methodology models slip activity in SC superalloys. The foundation of the method is the multiplicative rule used for the deformation gradient given as

$$\mathbf{F} = \mathbf{F}^{\mathbf{e}} \cdot \mathbf{F}^{\mathbf{p}} \tag{2.49}$$

where the deformation gradient, $\boldsymbol{F}$, is composed of elastic, $\boldsymbol{F^e}$, and plastic $\boldsymbol{F^p}$, deformation gradients. This decomposition is illustrated in Figure 2.8. The elastic deformation gradient models the reversible elastic stretch and rigid body rotation of the lattice while the plastic deformation gradient accounts for dislocation motion associated with a change in the shape of the grain but not its crystal lattice.

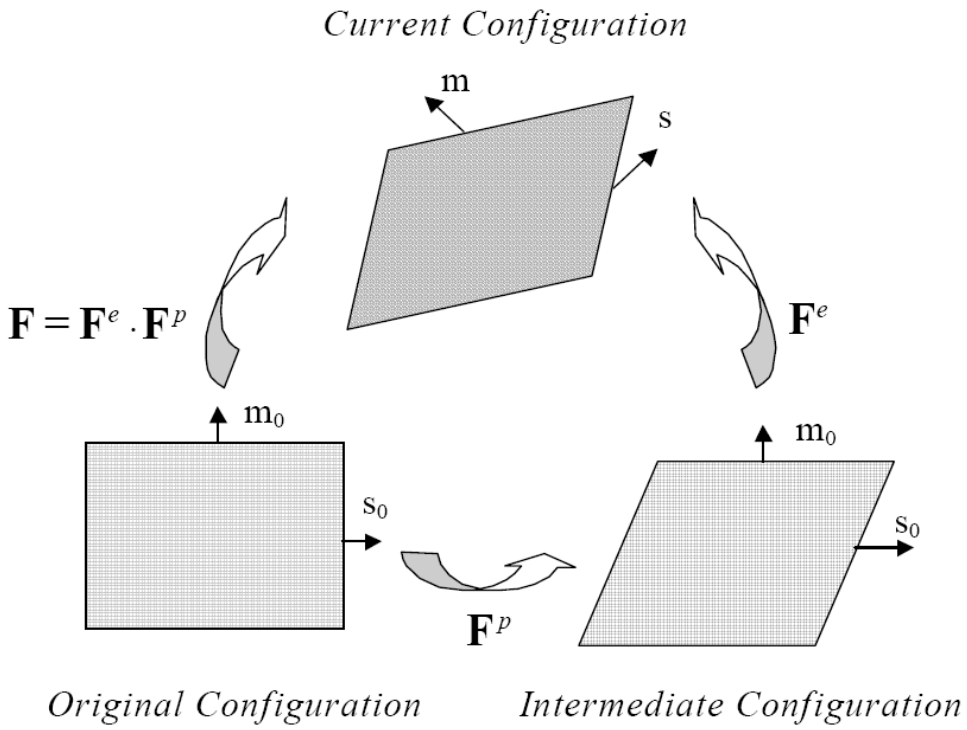

Figure 2.8: *Elastoplastic decomposition of the deformation gradient [16].*

The model explicitly accounts for crystallographic orientations, but does not explicitly account for the matrix and precipitate phases. Twelve octahedral <110> slip

systems are active for the entire range of temperatures. At high temperatures octahedral slip occurs in a zigzag motion in matrix channels separating precipitate particles. This behavior is effectively captured with six macroscopic cubic slip systems, {100}<110> type.

The flow rule for the slip system shearing rate captures temperature, stress, and strain dependence in the material given as

$$\dot{\gamma}^{\alpha} = \dot{\gamma}_0 \Theta(T) \left\langle \frac{\tau_v^{\alpha}}{D^{\alpha}} \right\rangle^{n} \exp\left\{ B_0 \left\langle \frac{\tau_v^{\alpha}}{D^{\alpha}} \right\rangle^{n+1} \right\} \operatorname{sgn}\left(\tau^{\alpha} - \chi^{\alpha}\right) \tag{2.50}$$

where α represents the slip system, and the slip system viscous overstress, τ_v^{α}, is given in terms of the resolved shear stress, τ^{α}, by

$$\tau_v^{\alpha} = \left|\tau^{\alpha} - \chi^{\alpha}\right| - \kappa^{\alpha} \frac{\mu}{\mu_0} \tag{2.51}$$

Here, χ^{α} is the backstress, κ^{α} is the threshold stress on each slip system, μ is the shear modulus, and μ_0 is the shear modulus at absolute zero. The power law exponent, n, is a constant, the coefficient, B_0, is constant, and drag stress, D^{α}, only weakly depends on the history of temperature and viscoplastic deformation. The temperature dependent diffusivity parameter, $\Theta(T)$, is given by

$$\Theta(T)=\begin{cases}\exp\left(-\dfrac{Q_0}{RT}\right) & T\geq\dfrac{T_m}{2}\\ \exp\left(-\dfrac{2Q_0}{RT_m}\left[\ln\left(\dfrac{T_m}{2T}\right)+1\right]\right) & T\leq\dfrac{T_m}{2}\end{cases}\quad\text{for,}\tag{2.52}$$

where Q_0 is the activation energy for thermally activated dislocation bypass of obstacles, R is the universal gas constant, and T_m is the absolute melting point temperature.

The backstress evolution has been written as

$$\dot{\chi}^{\alpha}=h_{\chi}\left|\dot{\gamma}^{\alpha}\right|\operatorname{sgn}\left(\tau^{\alpha}-\chi^{\alpha}\right)-h_{\chi d}\chi^{\alpha}\left|\dot{\gamma}^{\alpha}\right|+\left(\frac{1}{R_{\chi}}\frac{\partial R_{\chi}}{\partial T}+\frac{1}{h_{\chi d}}\frac{\partial h_{\chi d}}{\partial T}\right)\chi^{\alpha}\dot{T}-h_{\chi s}(T)\left|\chi^{\alpha}\right|^{r_{\chi s}}\tag{2.53}$$

The first two terms describe the hardening and dynamic recovery, the third term accounts for changes in material parameters with temperature change, and the last term is the static thermal recovery term. h_{χ}, $h_{\chi d}$, $h_{\chi s}$, $r_{\chi s}$, and $R_{\chi}=h_{\chi}/h_{\chi d}$ are material constants.

The threshold stress corresponds to the size of the viscoplastic flow potential. Therefore the threshold stress may be viewed as the resistance to plastic flow arising from statistical strengthening mechanisms associated with increase of dislocation density and solid solution strengthening. The threshold stress, κ^{α}, is given as

$$\kappa^{\alpha}=\kappa_c^{\alpha}+\kappa_e^{\alpha}\tag{2.54}$$

where

$$\kappa_c^\alpha = \kappa_0^\alpha(T) + h_{pe}\tau_{pe}^\alpha + h_{se}\tau_{se}^\alpha + h_{cb}\left|\tau_{cb}^\alpha\right| \tag{2.55}$$

$$\kappa_e^\alpha = h_0 \sum_{\beta=1}^{N_{slip}} q^{\alpha\beta}\left|\gamma^\beta\right| - h_{\kappa s}\kappa^\alpha \sum_{\beta=1}^{N_{slip}}\left|\gamma^\beta\right| - h_s\Theta(T)\left\langle \kappa^\alpha - \kappa_{th}\right\rangle^{r_s} \tag{2.56}$$

Here, τ_{pe}, τ_{se}, and τ_{cb} are the shear stresses on the primary, secondary, and cube slip systems, respectively. Prior to any deformation, the back stress is initially zero (i.e., $\chi^\alpha(0) = \kappa_e^\alpha(0) = 0$).

In addition to a crystal plasticity model, Shenoy et al. [45] formulated a transversely isotropic continuum viscoplasticity model for DS Ni-base superalloy. This was partially motivated by the fact that crystal plasticity models are often too computationally intensive if the objective is to model the macroscopic behavior of an engineering component. In the same manner as the crystal plasticity model, the constitutive model is implemented as a UMAT subroutine in ABAQUS [46]. The transversely isotropic viscoplasticity model does not explicitly consider 3-D grain structure resulting in a reduction in computational costs.

CHAPTER 3

EXPERIMENTAL METHOD

Experiments were performed as part of this research to develop, calibrate, and validate necessary components of the analytical model. All experiments were isothermal with temperatures of 750°*C* and 950°*C*. Tests were performed on smooth and notched specimens. There were two types of experiments performed, baseline LCF tests and time-dependent fatigue tests. Baseline LCF tests were performed under continuously cycled (CC) conditions at a strain rate ($\dot{\varepsilon}$) of 1.0×10^{-3} 1/*s*. Creep-fatigue tests (fatigue tests with dwells) and slow strain rate (SSR) CC fatigue tests fall under the "time-dependent fatigue test" category. The SSR tests were performed with $\dot{\varepsilon} = 5.0 \times 10^{-5}$ 1/*s*. Some LCF data on smooth and notched specimens was made available by Siemens; all other experiments were conducted in the Mechanical Properties Research Laboratory (MPRL) at Georgia Tech.

3.1 Test Material

The CM247LC DS material was received in three 203.2 *mm* x 127 *mm* x 25.4 *mm* (8 *in* x 5 *in* x 1 *in*) cast slabs with the longitudinal orientation being the long direction of the slab. Blanks were excised from the slabs using wire electrical discharge machining (EDM) method and machined to specification in both longitudinal (L) and transverse (T) directions, as shown in Figure 3.1.

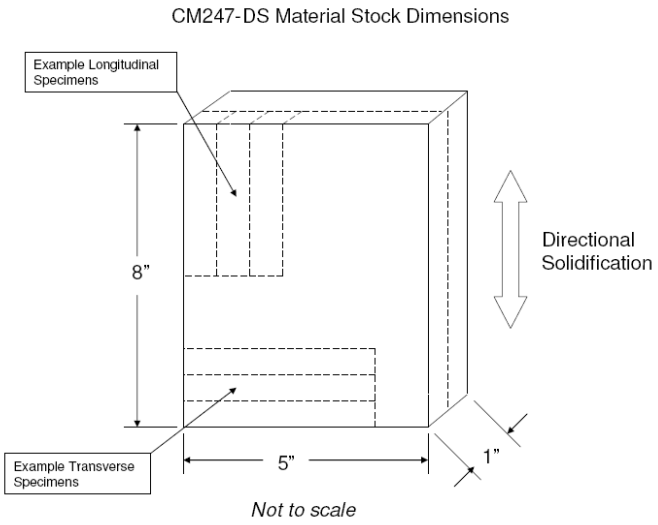

Figure 3.1: *Orientation of L and T specimens.*

Three different fatigue specimen geometries were used: one smooth specimen and two notched specimens. The smooth specimen, shown in Figure 3.2, was designed to meet recommended dimensions of ASTM Standard Practice for Strain-Controlled Fatigue Testing (ASTM E606-04) and will be referred to as k_t=1, or smooth specimen. The gage section has a diameter of 6.35 *mm* (0.25 *in*) and has a length of 12.7 *mm* (0.5 *in*).

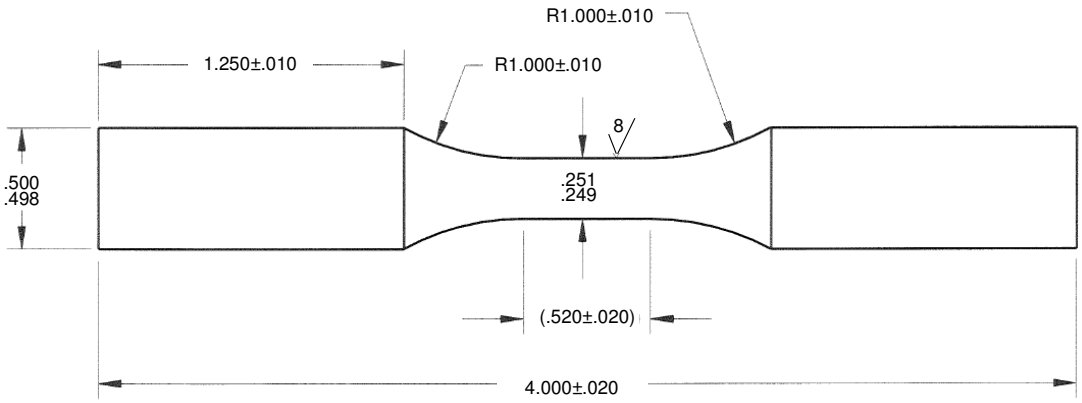

Figure 3.2: *Smooth specimen (units in in.).*

The two different notched geometries were considered as shown in Figure 3.3. The geometry of the notch is the same as previously used by Siemens for notch testing so that the data obtained in previous studies is relevant to the current work. The notches are 60^o v-notches with differing notch root radii. One notch has a k_t of about 2 with a notch radius (ρ) of 0.036 *in* (0.9271 *mm*) and the sharper notch has a k_t of about 3 with a notch radius of 0.012 *in* (0.3175 *mm*). For a 3D notch, the k_t is dependent on material properties and orientation. Therefore, the notches will be referred to as k_t=2 and k_t=3 even though their precise k_t may differ. The diameter of the net section is 6.35 *mm* (0.25 *in*).

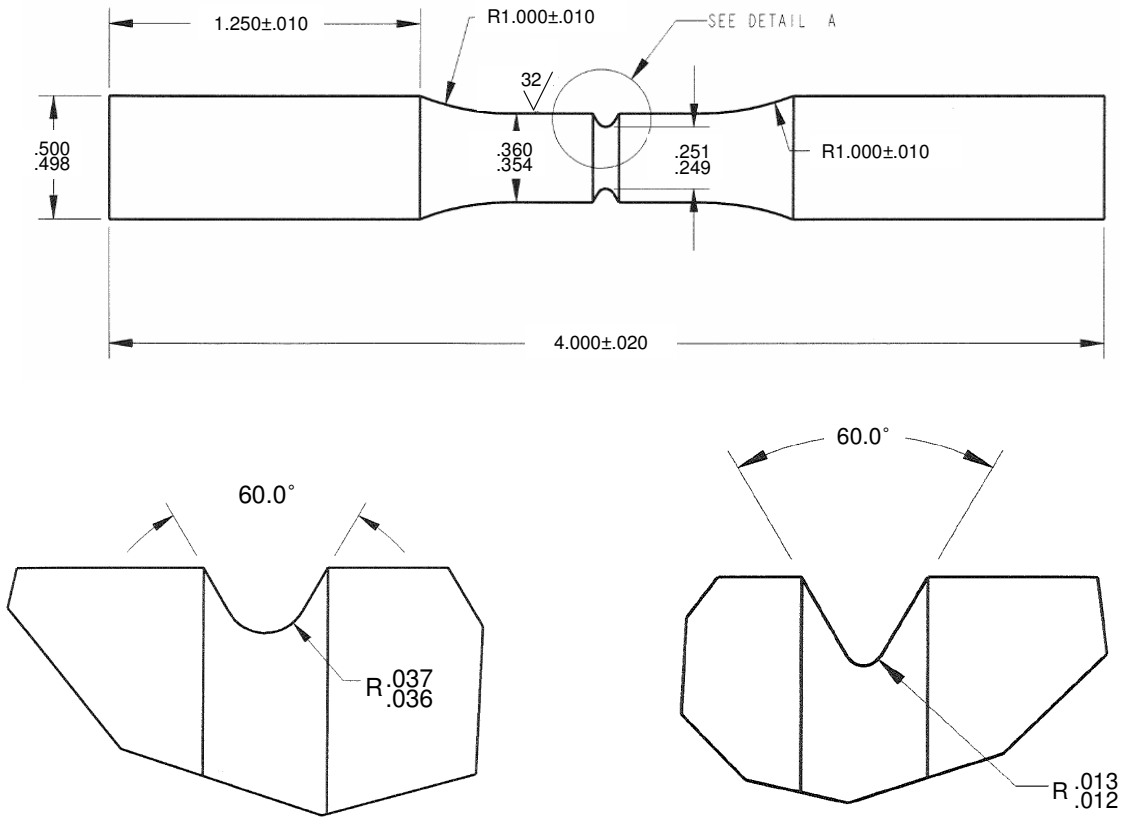

Figure 3.3: *Notched specimens (units in in.).*

The specimens were low stress ground to ensure accuracy in dimensions and to be sure no significant residual stresses were created during the finishing steps of the machining process. Specific machining instructions are given in Table 3.1.

Table 3.1: *Specimen machining instructions.*

Machining Instructions:
1260 RPM
2473 SFPM
Notch - Final 0.020" Low Stress Ground
Wheel—7.5" DIA. A-120-S5-BA2
Water-Base Coolant
Polish—P600-P1000 Circumferential

The specimens were prepared by MAR-TEST Inc. (Cincinnati, OH). In all, 41 test specimens were machined for 38 planned fatigue tests. These 38 planned tests included 17 baseline LCF tests as well as 21 time-dependent creep-fatigue tests. A list of the specimens is given in Table 3.2.

Table 3.2: *List of specimens.*

Specimen Type	*Total*	*L*	*T*
Smooth (k_t=1)	12	8	*4*
Notched (k_t=2)	16	10	*6*
Notched (k_t=3)	13	10	3
Total	41	28	13

Fatigue specimens were visually inspected to ensure that all residual and polishing marks, if any, were along the stress axis, following ASTM Standard E606-04.

Specimens were the degreased in acetone and rinsed with ethanol. Acetone is not used in the final cleaning step because it can leave a residual film on the surface.

3.2 Baseline Low Cycle Fatigue Tests

Baseline LCF tests were performed to determine the effects of high temperature, orientation, stress concentrations on the fatigue of CM247LC DS. Siemens provided similar data for smooth and notched specimens at 500°*C*, 750°*C*, 850°*C*, and 950°*C*. All tests at Georgia Tech were fully reversed (R=-1). Baseline LCF tests were isothermal, continuously cycled, fully reversed and were performed at 750°*C* and 950°*C* in both L and T grain orientations. For the strain-controlled tests the strain rate was 1.0×10^{-3} 1/*s* during loading and unloading ramps. Force-controlled tests had a fixed cycle period of 18 *s*. The cycle time was chosen to be as similar as possible to strain-controlled tests, in an attempt to eliminate the influence of strain rate dependence from the material response. Triangular waveforms were used in all tests.

Sampling frequency of data acquisition was sufficient to insure correct definition of the hysteresis loop. Force (*lbs*), strain, and displacement (*in*) were recorded for the first 10 cycles and every 10^{th} cycle after that. The peak and valley forces were recorded for every cycle.

All LCF tests were performed on a 10 *kip* axial servo-hydraulic MTS® testing machine with a dual-channel controller and TestStar software (Testware SX® 4.0D), shown in Figure 3.4.

Figure 3.4: *Equipment used to perform experiments in the MPRL.*

Smooth specimen tests were conducted under mechanical strain control, isothermal conditions, and static, room temperature laboratory air. Notched specimens were conducted under the same conditions but under load control.

K-type (Omega® model GG-K-26-SLE) thermocouples (T/C) having 0.404 *mm* (0.159 *in*) diameter leads (26 gage) were spot welded to the end of the gage section to monitor temperature within the gage section, as shown in Figure 3.5. The lower specimen was fastened first within the lower hydraulic collet grip (MTS® model 646). The specimen was raised to fit with the top collet and heating coil. A nominal hydraulic pressure of 29 *MPa* (4200 *psi*) was applied to the grips. A high temperature

extensometer (MTS® model 632.52E-14) with 12.7 *mm* (0.5 *in*) gage length was used to measure displacement. The alumina extension rods, 3.5 *mm* (0.138 *in*) in diameter with pointed tips, were seated into dimples formed using an indentation jig by light taps of a hammer. An image of these components is shown in Figure 3.6.

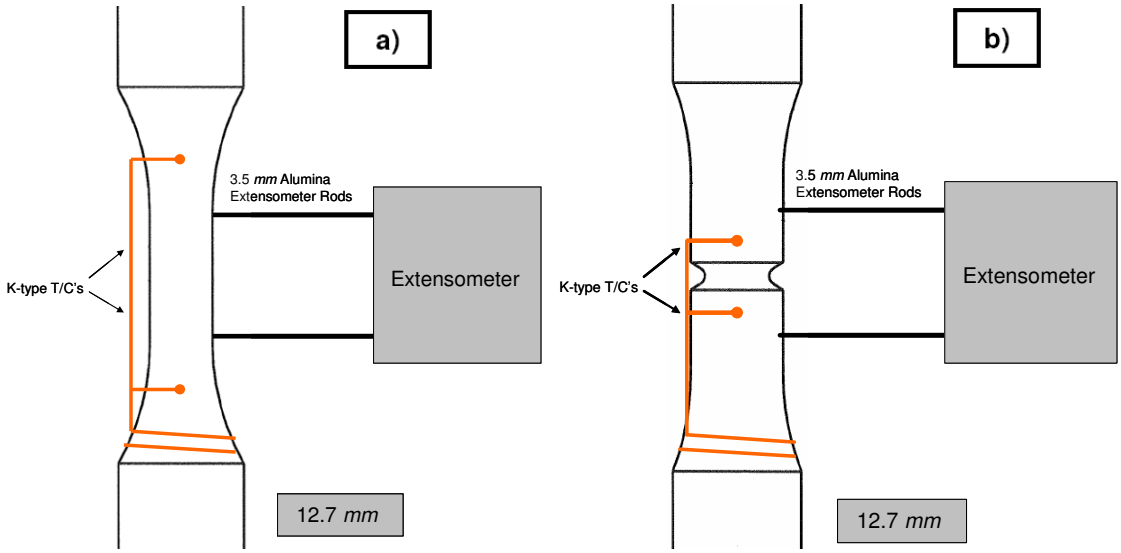

Figure 3.5: *Diagram of T/C placement on a) a smooth specimen and b) a notched specimen.*

A radio frequency (RF) induction heater (Ameritherm® single phase 2 *kW*) was used to heat the specimens. Closed-loop feedback control of the specimen temperature was maintained with a PID controller (Watlow® model 945A-2FK5-A000). The temperature control resolution was ±1 °*C*. Induction heat was chosen so that thermomechanical fatigue (TMF) experiments can be easily performed in future studies. The advantage of induction heat is that temperature can be relatively quickly cycled making it very suitable to TMF tests. Water-cooled grips were used to avoid overheating the collets. Tests were started approximately 5 *min* after the set-point temperature stabilized.

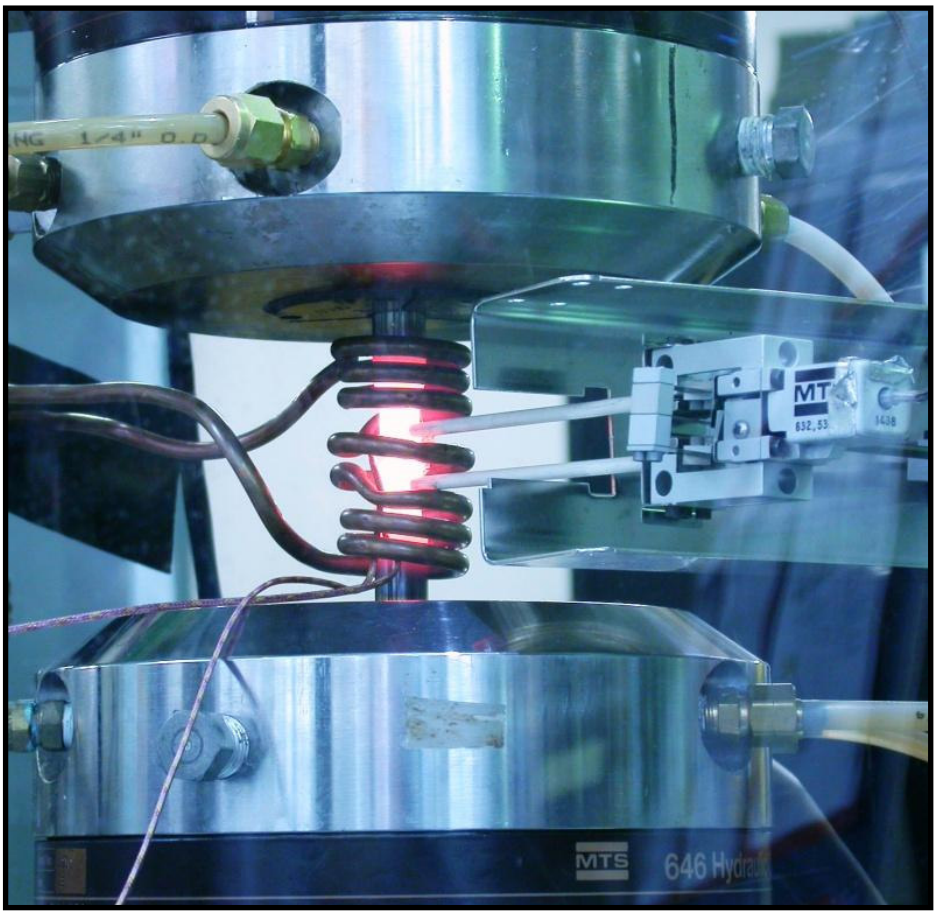

Figure 3.6: *Induction coil and high temperature extensometer during experiment.*

One induction coil, as shown in Figure 3.7, was used for both the lower (750°*C*) and higher (950°*C*) isothermal test temperatures. The coil was made from copper tubing having 4.7 *mm* (3/16 *in*) outer diameter and brass Swagelok® fittings. The inner diameter of each turn was at least 23 *mm* (0.9 *in*) in diameter. All coils had the same diameter. The coil was configured in a symmetric 2½-1-2½ arrangement leaving enough space for the 0.5 *in* high temperature extensometer's alumina extensions to fit between the coils and contact the specimen with adequate room on both sides.

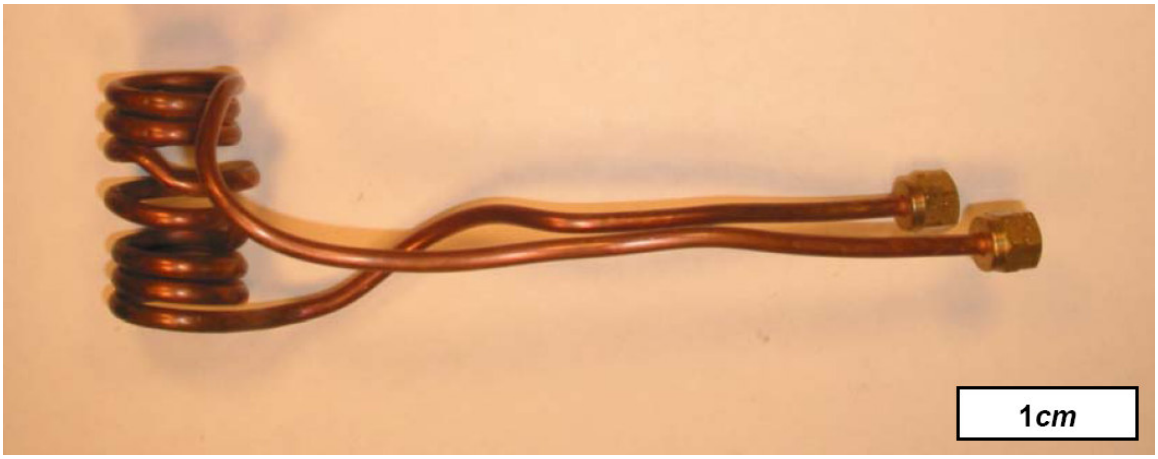

Figure 3.7: *Induction coil used for all experiments.*

According to ASTM standard E606-04, for materials that are fatigue tested at temperatures other than ambient, all temperature throughout the gage section shall be

$$T_n \pm \Delta T$$

where

T_n = nominal test temperature in $°C$ and

$\Delta T = 2°C$ or 1%, whichever is greater

This criterion was achieved by verifying that the induction coil was shaped in such a way that the temperature at the gage section was uniform. Five K-type thermocouples (Omega® model GG-K-26-SLE) were spot-welded to a dummy specimen, three within the gage section and one at each shoulder. The specimen was then fastened into both grips and heated to temperatures of $750°C$ and $950°C$, with cooling water running through the grips. The temperature distribution was recorded and verified that satisfied ASTM standard E606-04 and produced the maximum temperature at the center of the

gage section. This helps guarantee that crack initiation occurs within the extensometer tips. For every experiment, 15.2 *mm* (0.60 *in*) of the specimen ends were gripped by the water cooled collets for consistency and to ensure that the specimen is symmetrically cooled.

3.3 Creep-Fatigue Tests

To capture the effect of dwells in the analytical model creep-fatigue tests were performed. There are two different types of time-dependent tests explored, tests with holds in tension or compression (HT and HC, respectively) and tests that are continuously cycled but at a slower rate than baseline CC tests (SSR).

The tests with dwells were fully reversed with a 10 *min* hold time (t_{hc} for compressive hold and t_{ht} for tensile hold). The loading rate for the rest of the cycle is identical to the LCF tests (i.e., 1.0×10^{-3} 1/*s* for strain-controlled tests and 18 *s*/*cycle* for force-controlled tests. The total time for loading and unloading is t_{cc}. The total time to complete one cycle (t_{tc}) with a compressive hold (HC) is given as

$$t_{tc} = t_{hc} + t_{cc} \tag{3.1}$$

Similarly, for a tensile hold (HT) it calculated as

$$t_{tc} = t_{ht} + t_{cc} \tag{3.2}$$

Holds were performed both in tension and compression to include the effects of each in the analytical model. Tests were conducted at either 750°*C* or 950°*C* to capture the effects of different temperatures on sensitivity to creep.

The remaining time-dependent tests were continuously cycled but at a much slower rate (slow strain rate or SSR). The loading rate was 5.0×10^{-5} 1/*s* for strain-controlled tests and a cycle time of 618 *s* for force-controlled tests. These rates were chosen so that the total cycle time for the SSR tests were nearly the same for the total cycle time of the tests with dwells (HC and HT).

3.4 Crack Initiation Criteria

In order to separate the components of crack initiation and propagation, suitable crack initiation criteria were employed. For Ni-base alloys, a crack initiation depth (a_i) commonly used is 0.5-1.0 *mm*. Two different criteria were used, one for strain-controlled tests and one for the force-controlled tests.

Strain-controlled tests were performed on all the smooth specimens. In order to detect a crack a load drop criteria was used. When a crack grows, the load carrying capacity under strain control diminishes. When this load drop occurs, a crack of sufficient size has initiated. The load corresponding to crack initiation can be estimated as

$$P_i = P_0\left[1-\left(\frac{a_i}{d_0}\right)^2\right] \tag{3.3}$$

where P_0 is the stabilized maximum force and d_0 is the cross-sectional diameters of gage section. For this investigation, the cycle during which the tensile load dropped 5% from P_0 is used to define the crack initiation life ($N_i^{5\%}$ or N_i).

$$0.95 = \frac{P_i(N_i)}{P_0} \tag{3.4}$$

Whenever possible crack initiation life at 10%, 20%, 100% load drop (i.e., $N_i^{10\%}$, $N_i^{20\%}$, N_f, respectively) were also determined. To easily determine these values, a force versus cycles plot was created for each test using the peak and valley data generated.

Force-controlled tests were performed on all the notched specimens. A stiffness drop method was used. A high-temperature extensometer with 0.5 *in* (12.7 *mm*) gage length was used to measure displacement surrounding the notch. In the presence of a significant crack a tension-compression stiffness asymmetry develops. In tension, the specimen becomes less stiff because the crack is open, whereas in compression, the crack is closed and has no effect on stiffness, as illustrated in Figure 3.8. This example demonstrates that as the crack grows the stiffness continues to decrease until failure. Stiffness analysis can be performed at select cycles and the ratio (R_E) between tensile stiffness (E_T) and compressive stiffness (E_C),

$$R_E = \frac{E_T}{E_C} \tag{3.5}$$

can be determined and then plotted versus cycles as illustrated in Figure 3.7b.

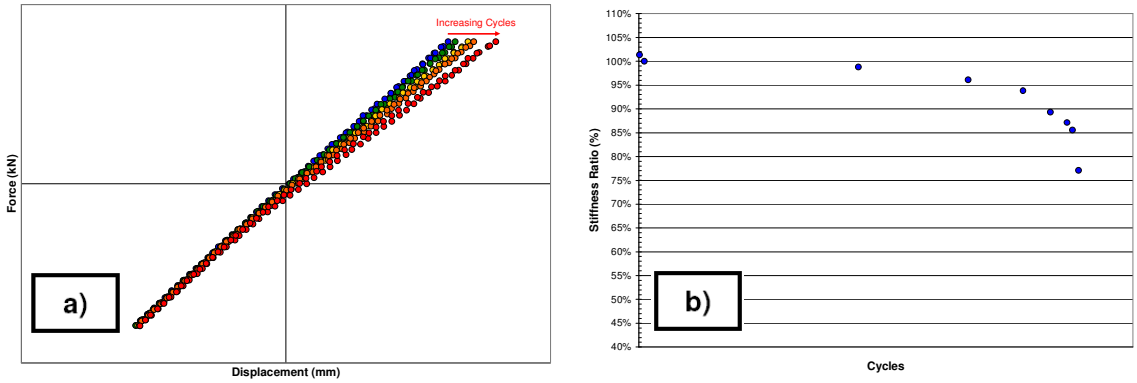

Figure 3.8: *Example of crack size effect on a) the force versus displacement curve and b) the stiffness versus cycles plot.*

The stiffness ratio of the 10th cycle was used as the reference stabilized stiffness. Hence, the stiffness ratio in the first may be in excess of 100% if cyclic softening occurs, as in this example based on actual data. The R_E for all other cycles were scaled by the same amount. In order to select which R_E correlates with a particular crack size, some tests were stopped before N_f and the specimens were loaded at room temperature until fracture. The crack was then measured to correlate the stiffness drop with crack depth, such as shown in Figure 3.9.

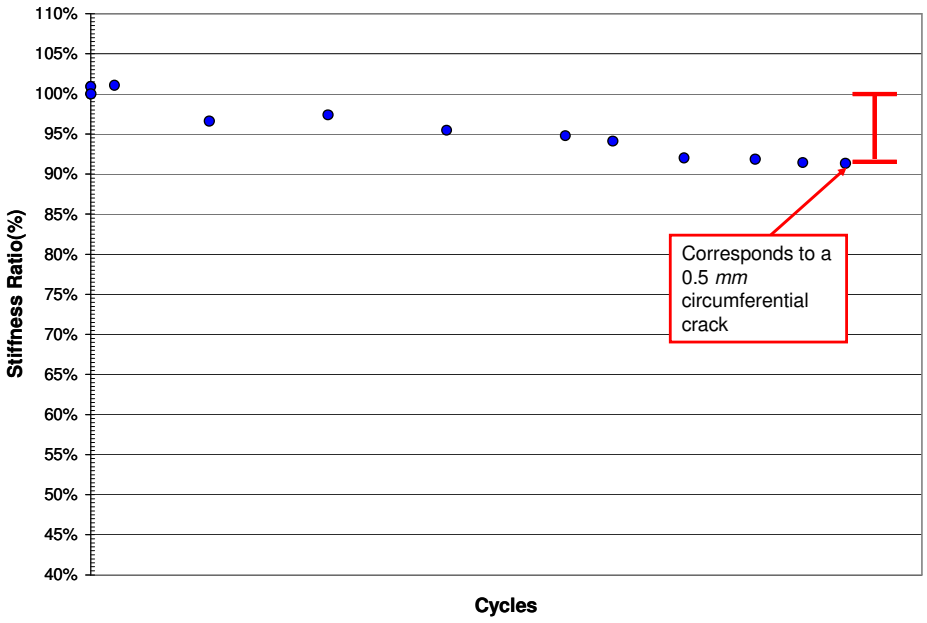

Figure 3.9: *Demonstration of stiffness drop method crack initiation accuracy.*

It was found that a stiffness drop of 10% (i.e., R_E=90%) consistently correlates to a crack size between 0.5 and 1.0 *mm*. This result is dependent on position of the crack relative to the displacement measured from the extensometer as illustrated in Figure 3.10. It also depends on the shape and number of cracks present. If the crack forms on the back of the specimen relative to extensometer placement, the specimen can demonstrate an increase in stiffness as a result of specimen bending. In this case, a R_E=105% was chosen as the N_i because a 5% stiffness increase in tension is indicative of a crack being present. Specimen bending, resulting in an increase in stiffness, occurred in only 15% of the notched tests. The position of the fatigue crack with respect to extensometer placement was analyzed to show the region of crack growth responsible for the apparent increased tensile stiffness and is used in the crack initiation criteria.

Specimen bending was only seen when a thumbnail type crack developed at the back of the specimen with respect to extensometer placement from θ=135°-215°, as illustrated in Figure 3.10.

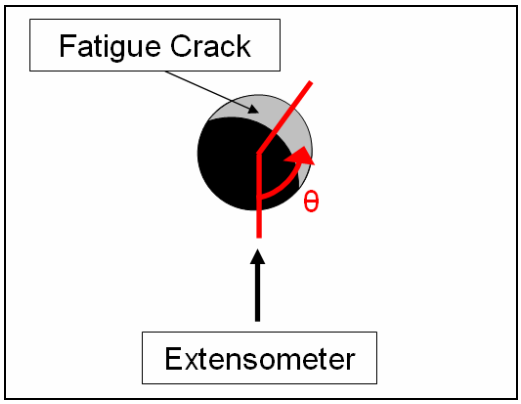

Figure 3.10: *Method for determining location of fatigue crack*

Note that another common method of detecting cracks is the potential drop method. The potential drop works by applying a continuous current (either AC or DC) to the specimen and having a sensitive instrument measure the voltage drop due to crack growth disrupting the resistance of the specimen. This method was not employed because the induction heat would disturb the sensitive potential measurements.

3.5 Metallography Procedure

Specimens were examined using light optical microscopy to observe grain boundaries and grain structure. The preparation procedure to view samples consisted of sectioning, mounting, grinding, and polishing.

Samples were sectioned using a low speed diamond saw. After sectioning, samples were cold-mounted in an epoxy resin. The resin consisted of a resin (Struers®

Epofix resin, HQ) and a hardener (Struers® Epofix hardener, HQ). Once the samples were mounted, they were ground and polished. The procedure for grinding and polishing the samples is shown in Table 3.3.

Table 3.3: *Grinding and polishing steps using Struers® RotoPol-15.*

Step	**Preparation Disc (Material)**	**Force (*N*)**	**Speed (*RPM*)**	**Suspension**	**Lubricant**	**Time (*min*)**
1 (Course Grind)	MD Piano (Resin bonded diamond disc)	30	150	None	Water	5
2 (Fine Grind)	MD Allegro (Composite disc)	25	150	DiaPro Allegro Largo	None	8
3 (Coarse Polish)	MD Mol (Woven wool)	20	150	DiaPro Mol	None	8
4 (Fine Polish)	MD Chem (Porous synthetic)	15	150	OP-S Suspension	None	2

The samples were then etched to expose the grain boundaries and grain structure using Kalling's 2 or Green contrast and is listed as etchant #94 in ASTM Standard E407-99. The components of the etchant used are listed in Table 3.4. The sample was submerged in the etchant for 60 *s* and immediately rinsed in water.

Table 3.4: *Etchant mix.*

Kalling's 2 (a.k.a. Green contrast)	
Chemicals (Formula)	**Quantity**
Copper Chloride ($CuCl_2$)	2 *g*
Ethanol (95%)	80 *mL*
Hydrochloric Acid (HCl)	40 *mL*

CHAPTER 4

EXPERIMENTAL RESULTS AND MICROSCOPY

4.1 Baseline Smooth Specimen LCF Results

There were three test conditions performed at Georgia Tech, longitudinal tests at 750°*C* (L750), transverse tests at 750°*C* (T750), and longitudinal tests at 950°*C* (L950). These tests were each performed on all three different geometry specimens (one smooth and two notched). To protect proprietary information, all data is normalized by a reference yield strength, strain at yield, and life. Normalization factors are the same for all results at both temperatures, so direct comparisons can be made.

Most smooth specimen results at a loading rate of 1.0×10^{-3} 1/*s* were available from the sponsor. Instead of repeating these experiments, a select few tests were conducted to verify the trends. The trend curves represent the average of the Siemens data and Georgia Tech data. Smooth specimen fatigue life results are shown in Figure 4.1. The square data points represent new experiments performed at Georgia Tech while the trend curves represent data provided by Siemens and new data generated at Georgia Tech. In strain control, the L750 orientation is much more fatigue resistant compared its T750 counterpart. The L950 condition has greater life in strain control than the T750 case.

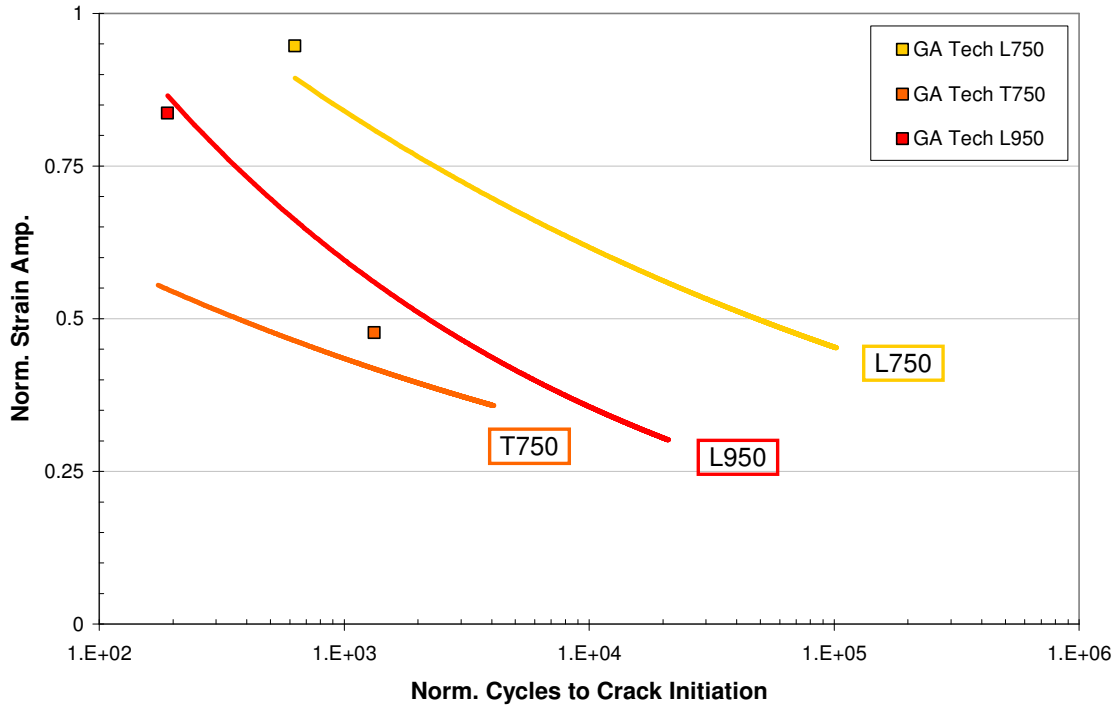

Figure 4.1: *Smooth specimen LCF results.*

The T orientated tests exhibited the largest experimental scatter, likely a result of the numerous grain boundaries perpendicular to the loading direction. Siemens also performed experiments at four temperatures, 500°*C*, 750°*C*, 850°*C*, and 950°*C*. These results are paired with data generated at Georgia Tech and are shown in Figure 4.2 and Figure 4.3.

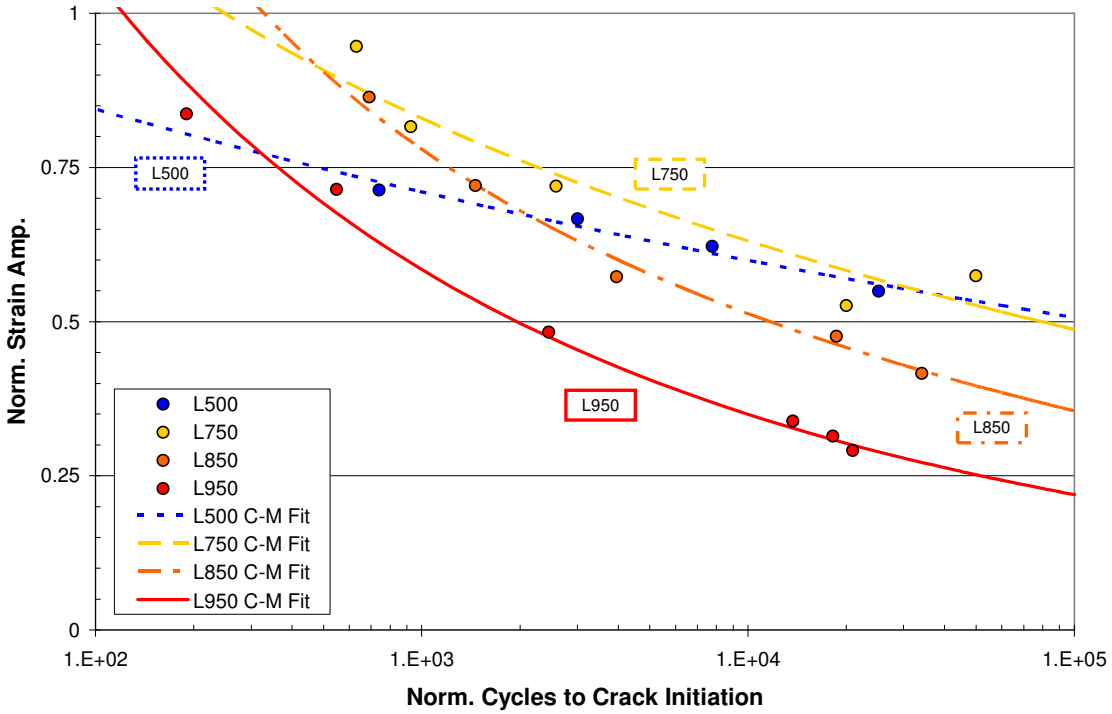

Figure 4.2: *L smooth specimen LCF results with modified Coffin-Manson fits.*

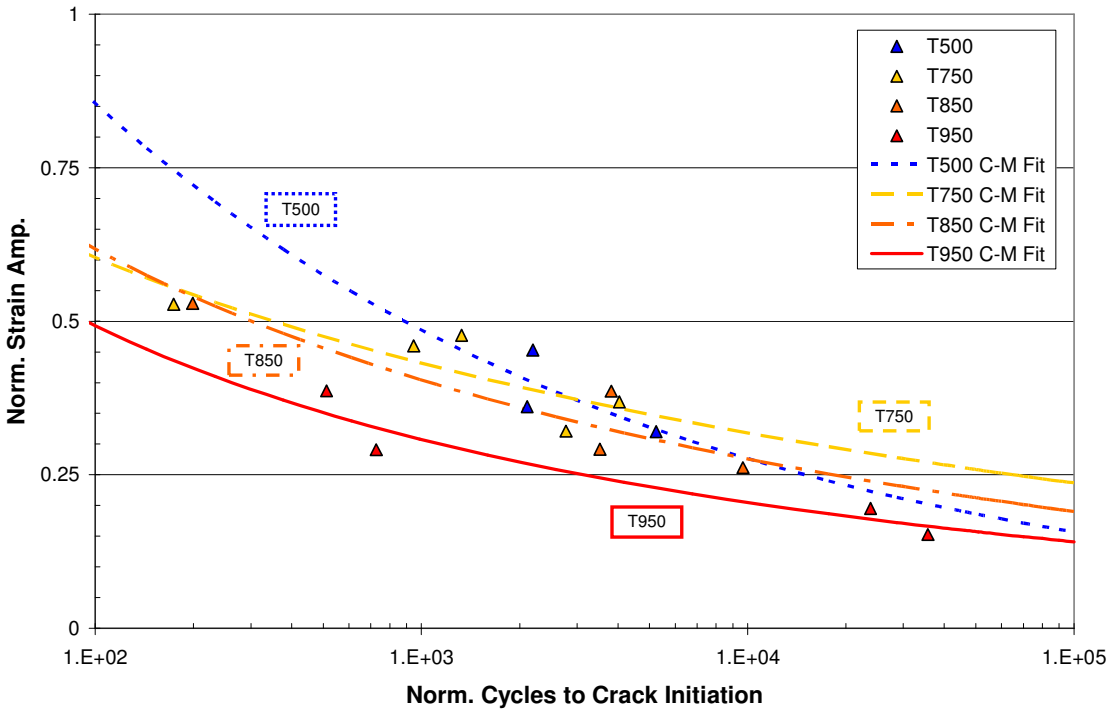

Figure 4.3: *T smooth specimen results with modified Coffin-Manson fits.*

The fatigue lives of the L orientation is much more temperature sensitive than the T orientation. The 500°*C* and the 950°*C* lie in close proximity to each other in the T experiments whereas a significant life decline is evident as the temperature of the L oriented specimens increases past 750°*C*. L500 and L750 have comparable fatigue resistance except in the very low cycle regime where L750 is superior. This is likely due to the improved yield strength in superalloys seen at ~750°*C*, shown in Figure 2.4. Figure 4.4 through Figure 4.6 show the stress-strain hysteresis of the first and half-life cycles for each of the smooth specimen test conditions.

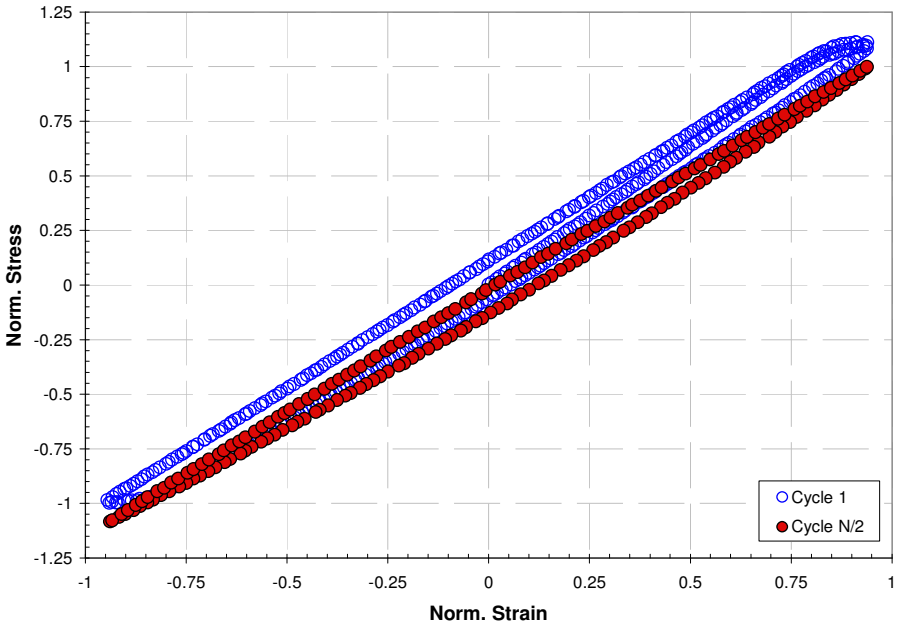

Figure 4.4: *L750 smooth specimen hysteresis at* $\dot{\varepsilon} = 1.0x10^{-3}$ *1/s.*

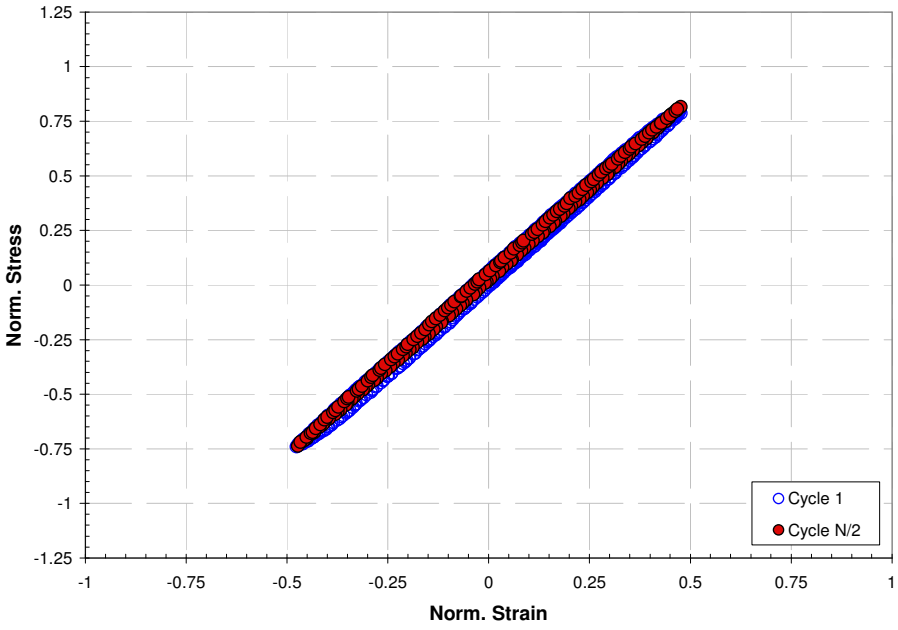

Figure 4.5: *T750 smooth specimen hysteresis at* $\dot{\varepsilon} = 1.0x10^{-3}$ *1/s.*

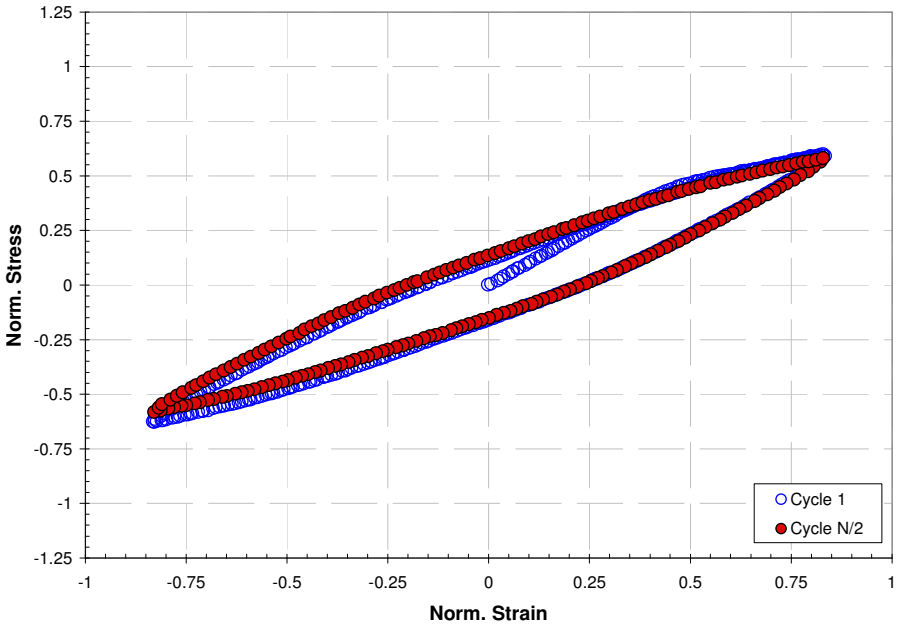

Figure 4.6: *L950 smooth specimen hysteresis at* $\dot{\varepsilon} = 1.0x10^{-3}$ *1/s.*

The strain-life data at each temperature and orientation was fit to the Basquin and Coffin-Manson relationships (also referred to as the modified Coffin-Manson relationship). This classical strain-life relation is a double power fit,

$$\frac{\Delta\varepsilon}{2} = \frac{\sigma'_f}{E}(2N_i)^b + \varepsilon'_f(2N_i)^c \tag{4.1}$$

where σ'_f is the fatigue strength coefficient, E is the elastic modulus, b is the fatigue strength exponent, ε'_f is the fatigue ductility coefficient, and c is the fatigue ductility component. The first term represents the elastic-strain life relation and the second term represents the plastic-strain life relation. The coefficients are determined by means of power law regression analyses for both terms. The fits of L and T data are shown in

Figure 4.2 and Figure 4.3, respectively. The transition life, N_t, is defined as the life corresponding to $\Delta\varepsilon_{el} = \Delta\varepsilon_{pl}$, i.e.,

$$N_t = \frac{1}{2}\left(\frac{\sigma'_f}{E\varepsilon'_f}\right)^{\frac{1}{c-b}} \tag{4.2}$$

Transition lives ranged from $N_t = 0$ to 20 *cycles* for L orientation and $N_t = 0$ to 2 *cycles* for T orientation. These low transition life values are typical of Ni-base superalloys and show that the elastic term dominates for most of the life, even in what is considered here as the LCF regime.

The cyclic behavior of CM247LC DS is very stable. The amount of softening or hardening is determined by comparing the first (1) and half-life ($N/2$) cycles' stress ranges

$$Hardening = \frac{\Delta\sigma_{N/2} - \Delta\sigma_1}{\Delta\sigma_1} \tag{4.3}$$

where negative hardening represents softening. In the L direction at 500°*C* and 750°*C* the hardening is on average 2.1% and 1%, respectively. Softening is observed at higher temperatures on average of 5.5% for 850°*C* and 5.9% for 950°*C*, both consistent with previous work [7, 8]. In the T orientation, similar behavior is observed but with more hardening and less softening. The average hardening for 500°*C* and 750°*C* is 2.9% and 2.8%, respectively. The average softening for 850°*C* is 0.7% and for 950°*C* is 1.4%.

The stress-strain response of CM247LC DS was fitted using a Ramberg-Osgood (R-O) relation. This relationship uses a plastic strain (ε_{pl}) given by a power law. When combined with the elastic strain (ε_{el}) the complete R-O relation for total strain (ε_t) is written as

$$\varepsilon_t = \varepsilon_{el} + \varepsilon_{pl} = \frac{\sigma}{E} + \left(\frac{\sigma}{K}\right)^{1/n} \tag{4.4}$$

where K is the strength coefficient and n is the strain hardening exponent. For cyclic hysteresis loops, a cyclically stabilized strength coefficient (K') and strain hardening exponent (n') are used to represent the stabilized cyclic material response

$$\frac{\Delta\varepsilon}{2} = \frac{\Delta\sigma}{2E} + \left(\frac{\Delta\sigma}{2K'}\right)^{1/n'} \tag{4.5}$$

R-O fits were performed on all tests where enough plastic deformation was present to adequately describe the material behavior.

Cyclic R-O fits were performed by plotting the monotonic response and fit with available cyclically stabilized stress and strain amplitudes (i.e., the tips of the cyclically stabilized hysteresis loops). The monotonic fits were then modified to go through the cyclically stabilized data. This method is shown in Figure 4.7. Using the cyclic R-O fits, the hysteresis loops are reproduced as shown in Figure 4.8. Cyclic R-O stress-strain relationship matches the material response well making it a suitable for use in the analytical model. Fits were also done on experiments with a slow strain rate so that a

rate-dependence can be incorporated into the analytical model. A comparison between stress-strain response of $\dot{\varepsilon}$=5.0x10^{-5} 1/*s* and $\dot{\varepsilon}$=1.0x10^{-3} 1/*s* tests are shown in Figure 4.9. The analytical model requires an adequate description of the stress-strain material response. The cyclic R-O fits accurately reflect the material behavior and because the CM247LC DS is relatively cyclically stable, this behavior should remain consistent for a majority of the fatigue life.

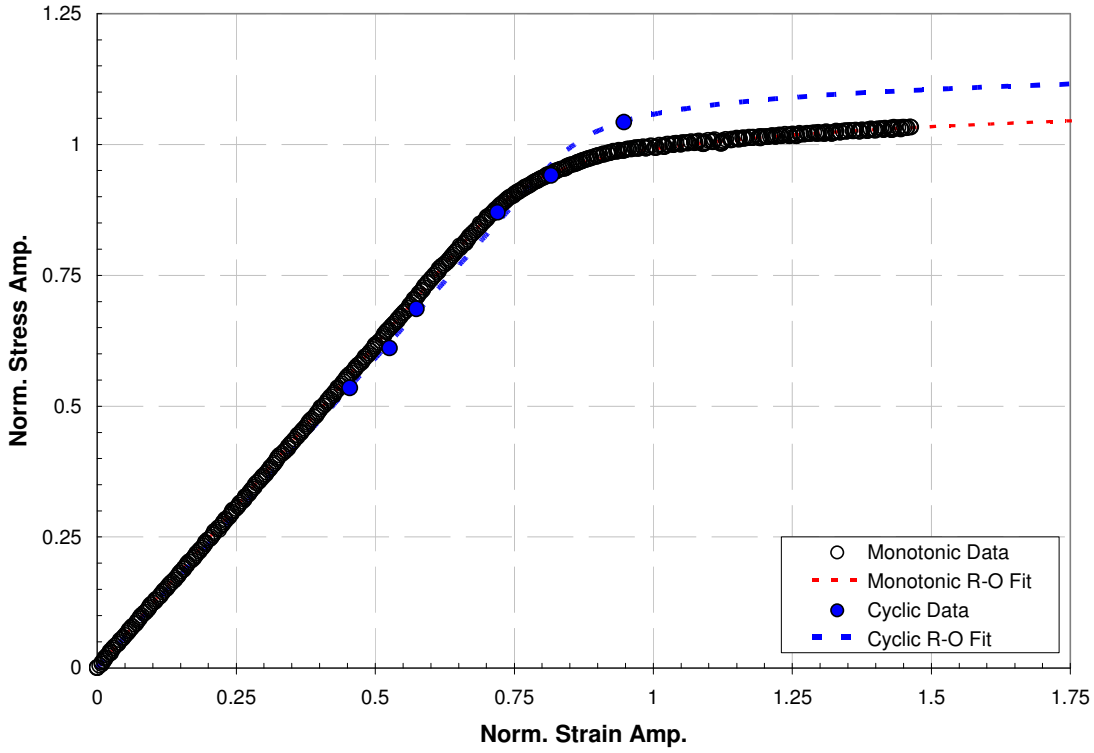

Figure 4.7: *Cyclic Ramberg-Osgood fit of a L750 at* $\dot{\varepsilon}$ *=1.0x10^{-3} 1/s.*

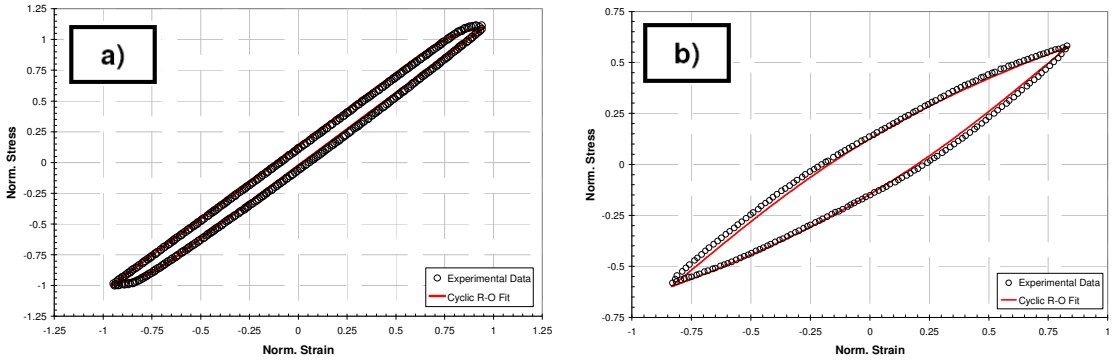

Figure 4.8: *Cyclic R-O fits at* $\dot{\varepsilon} = 1.0x10^{-3}$ *1/s of a) L750 and b) L950.*

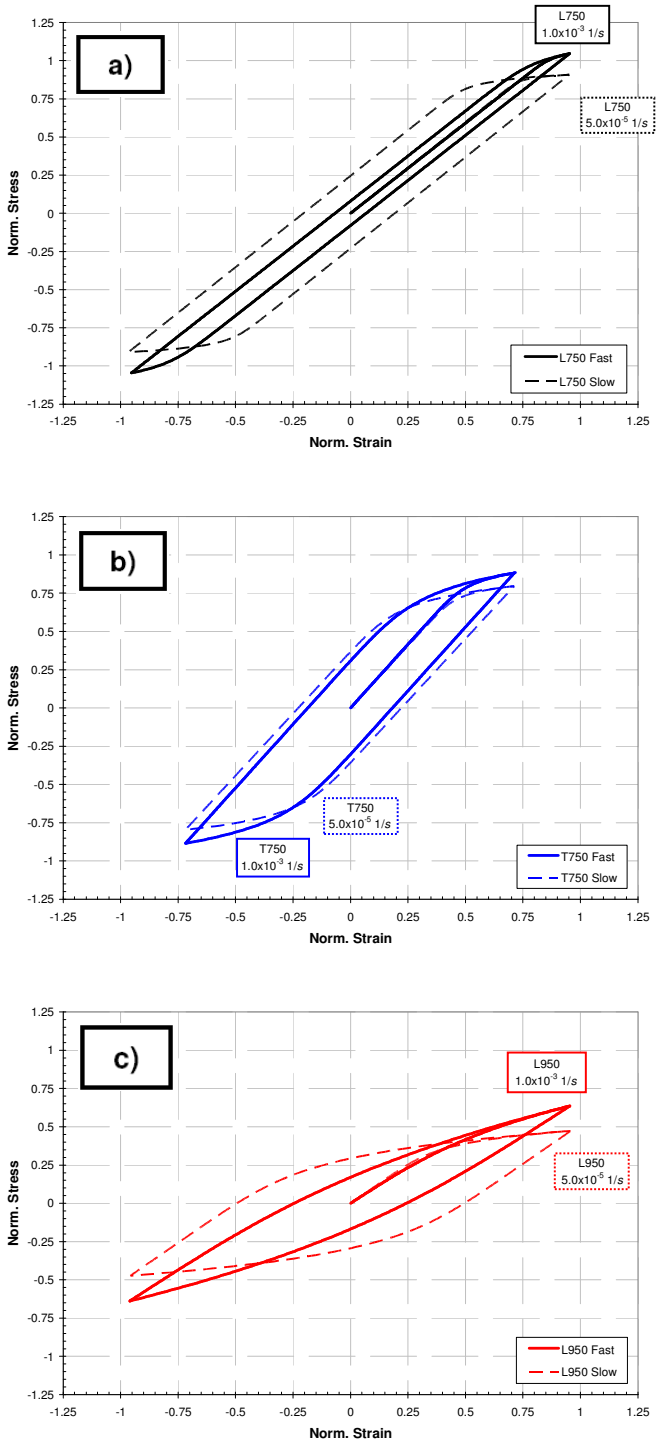

Figure 4.9: *Comparison of stress-strain response at two strain rates for a) L750, b) T750, and c) L950.*

4.2 Baseline Notched Specimen LCF Results

Experiments performed on notched specimens are compared to smooth specimens in Figure 4.10-Figure 4.12 for L and T orientations at temperature of 750°*C* and L orientation at 950°*C*. The results were plotted as nominal stress amplitude based on net section ($\Delta\sigma_N/2$) versus initiation life (N_i) so that reduction of lives due to presence of a stress concentration can be shown. The trend curves are based on both the new Georgia Tech data and Siemens data.

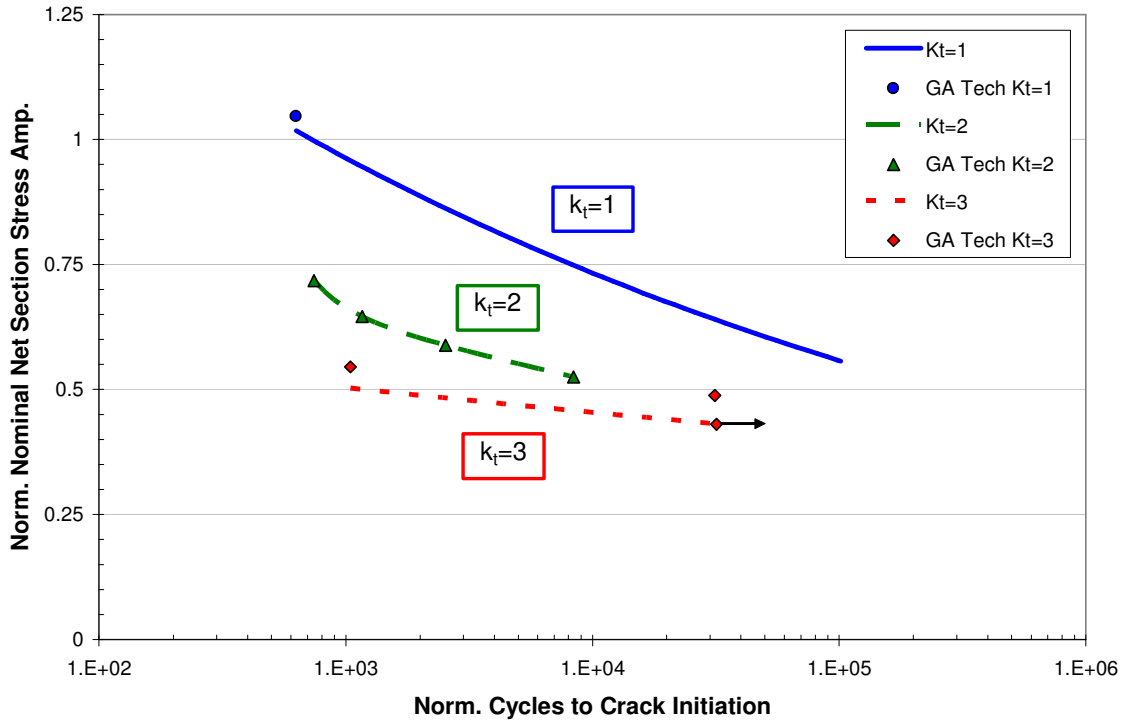

Figure 4.10: *L750 notched results.*

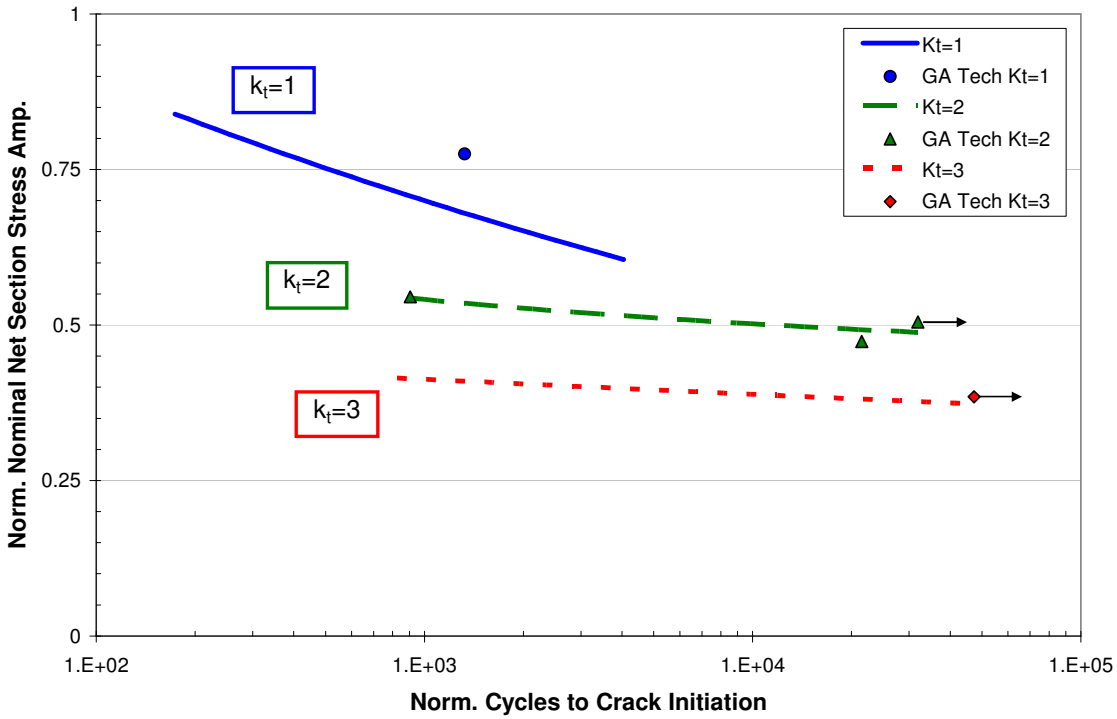

Figure 4.11: *T750 notched results.*

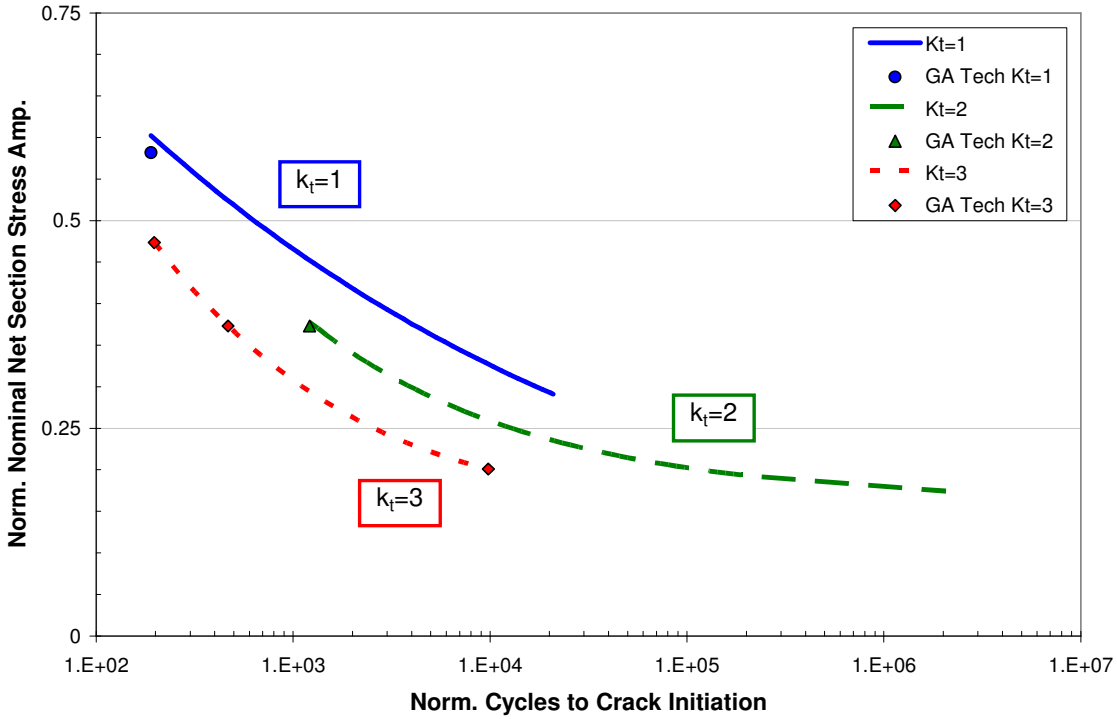

Figure 4.12: *L950 notched results.*

As expected, the presence of a stress concentration reduces the fatigue life of the specimens. The smooth specimens had the best fatigue resistance, with the severely notched (k_t=3) specimens the worst, and notched (k_t=2) specimens falling in between. At 950°*C*, stress concentrations have a reduced effect on life when compared to 750°*C* results. This is likely a result of the reduced yield stress and increased ductility at higher temperatures dulling the effect of the stress concentration. The effect of stress concentrations on T oriented specimens appears very similar to the effect in L orientation. A larger amount of scatter is present in the T orientation. This may be attributed to the probability of a grain boundary being aligned with the notch root. With L oriented

specimens, there is greater uniformity at the notch and a greater consistency with the fatigue results.

The effect of the notches can be best summarized by the fatigue notch factor (k_f). k_f describes the reduction in life as a result of the notch. The k_f values for different lives are shown in Figure 4.13. They are based on the trend curves fit through the smooth and notched specimen data. The fatigue notch factor $k_f(N)$ is the ratio of stresses for smooth specimen (σ_{ar}) to the nominal net-section stresses in a notched specimen (S_{ar}) for a particular fatigue life (N). According to the experimental results, the notch fatigue factor decreases as the life increases. The results show that k_f is much less than k_t for both notch geometries. k_f should always be less than k_t, and approaches k_t as the notch radius (i.e., the size of the notch) becomes very large. Even with limited data available, the trend shows that k_f is reduced with increased cycles for k_t=3 in L750, both notches in T750, and k_t=2 in L950. When k_f becomes 1, the stress concentration has no effect on fatigue life. This effect could be the result of non-propagating cracks in the high cycle fatigue (HCF) regime. The sharp stress gradient as a result of the stress concentration may develop a crack but the low stress levels found just outside the concentration fail to propagate the crack. There is less notch effect in the T orientation for both the k_t=2 and k_t=3 specimens. The decreasing k_f with increasing cycles is the reverse trend of what is typical for steels and aluminums. Materials are usually more sensitive to notches in the HCF regime. In the case of CM247LC DS, N_t is so small that it really is never in the LCF regime so this transition is not observed.

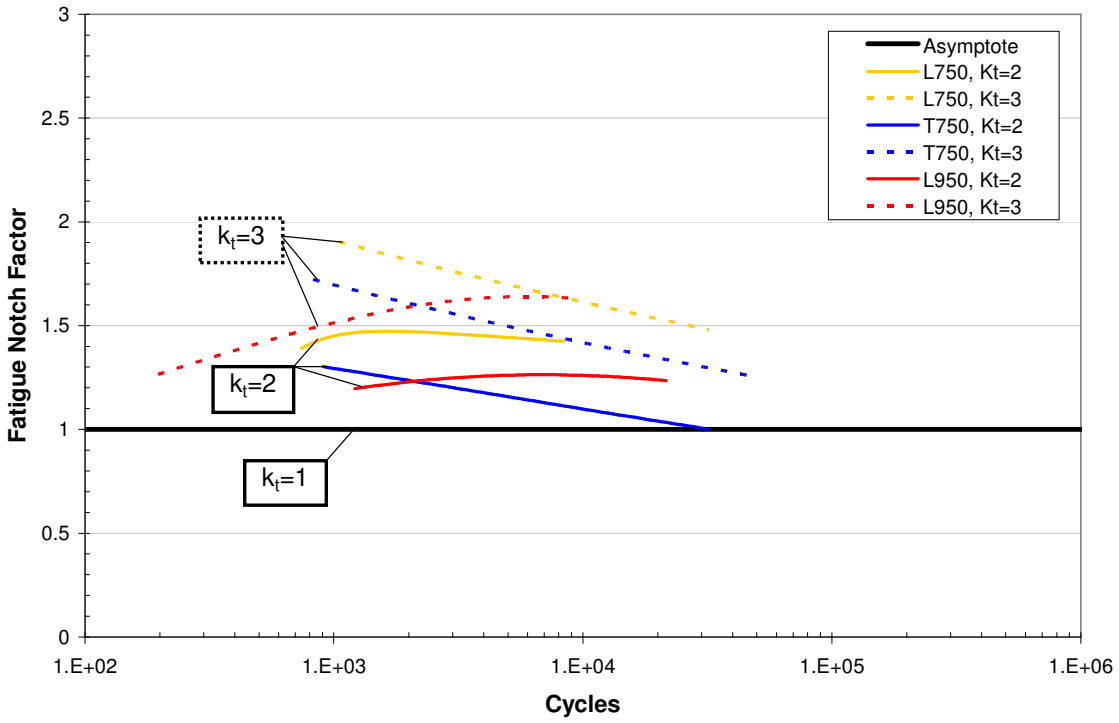

Figure 4.13: *Fatigue notch factors.*

4.3 Creep-Fatigue Results

The rate and dwell effects for smooth specimen tests are shown in Figure 4.14. At 750°*C* in the L orientation, the slow strain rate (SSR) CC test resulted in a decrease in life by a factor of 2 compared to the baseline higher rate CC tests. The hold in compression (HC) decreased life by a factor of 4 from the baseline CC tests. In the SSR case, the mean stress remains near zero, as shown in Figure 4.15. The compressive dwell produces a tensile mean stress of 27% of the stress amplitude, as shown in Figure 4.16, which likely contributes to the life reduction. A test with $\dot{\varepsilon}$=1.0x10^{-3} loading and $\dot{\varepsilon}$=5.0x10^{-5} unloading is shown in Figure 4.17. The SSR unloading developed a compressive mean stress of 6% the stress amplitude due to stress relaxation in tension.

As a result, the fatigue life was a factor of 2 greater than the equivalent SSR test. In the T orientation, a similar trend was observed. The HC specimen stabilized with a tensile mean stress of 17% of the stress amplitude as shown in Figure 4.19. However, the impact on life seemed to be negligible compared to the L orientation. A HT test developed a compressive mean stress of 24% the stress amplitude, as shown in Figure 4.20, increasing fatigue life by a factor of 2.5.

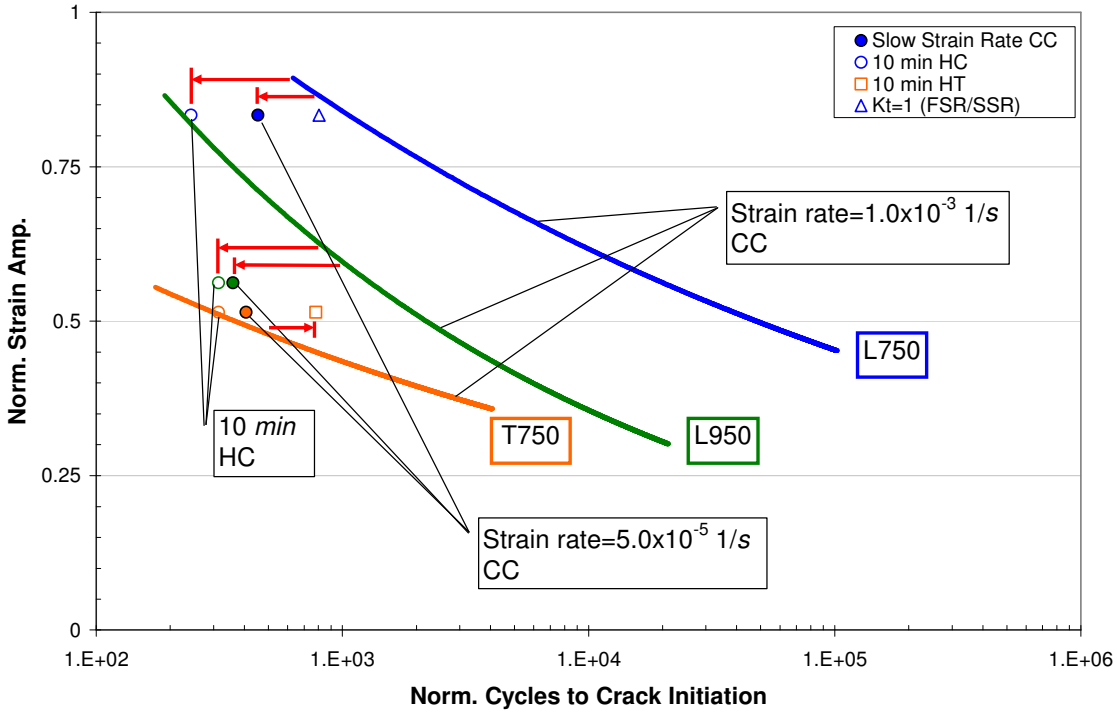

Figure 4.14: *Smooth specimen time-dependent results.*

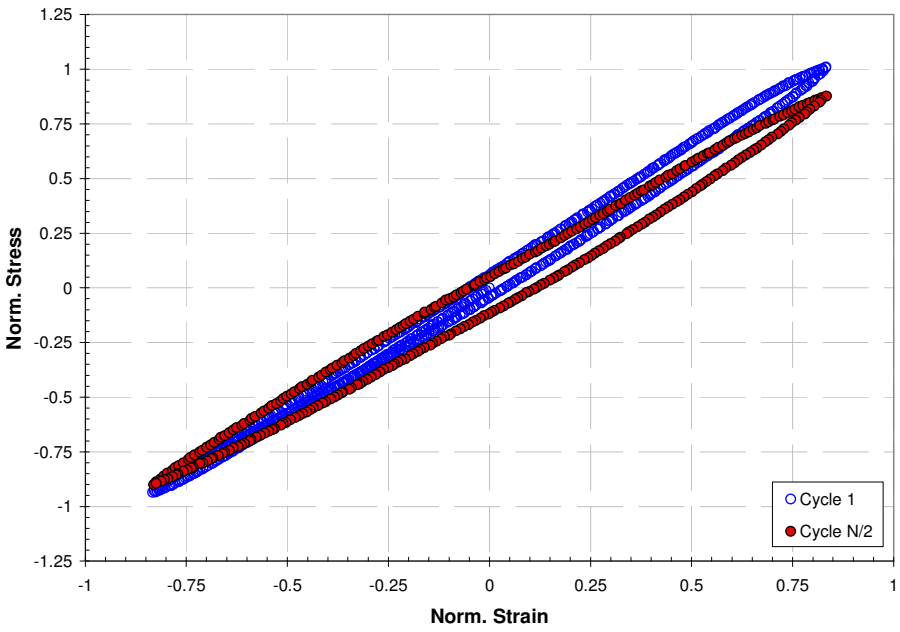

Figure 4.15: *L750 smooth specimen hysteresis at* $\dot{\varepsilon} = 5.0x10^{-5}$ *1/s.*

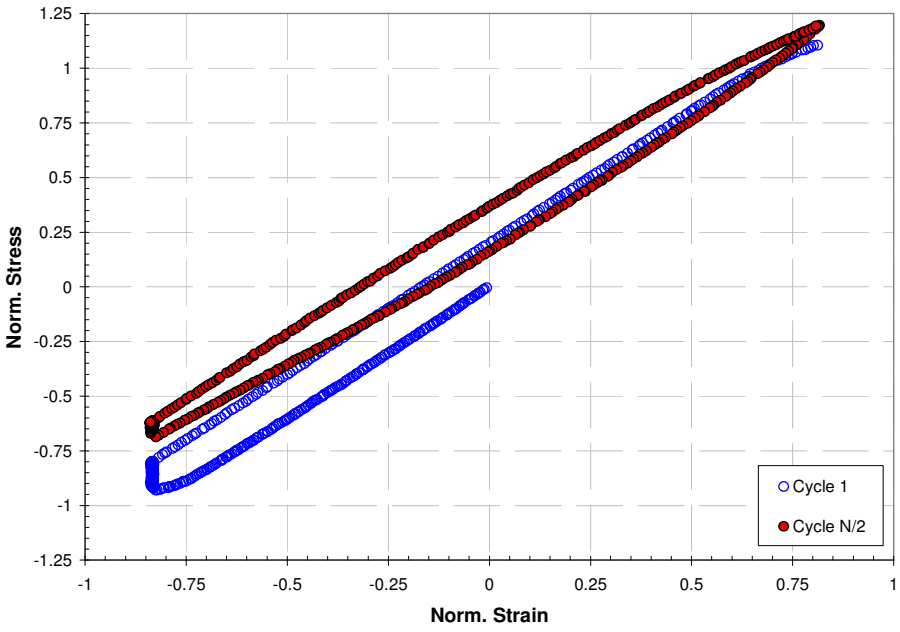

Figure 4.16: *L750 smooth specimen hysteresis with HC.*

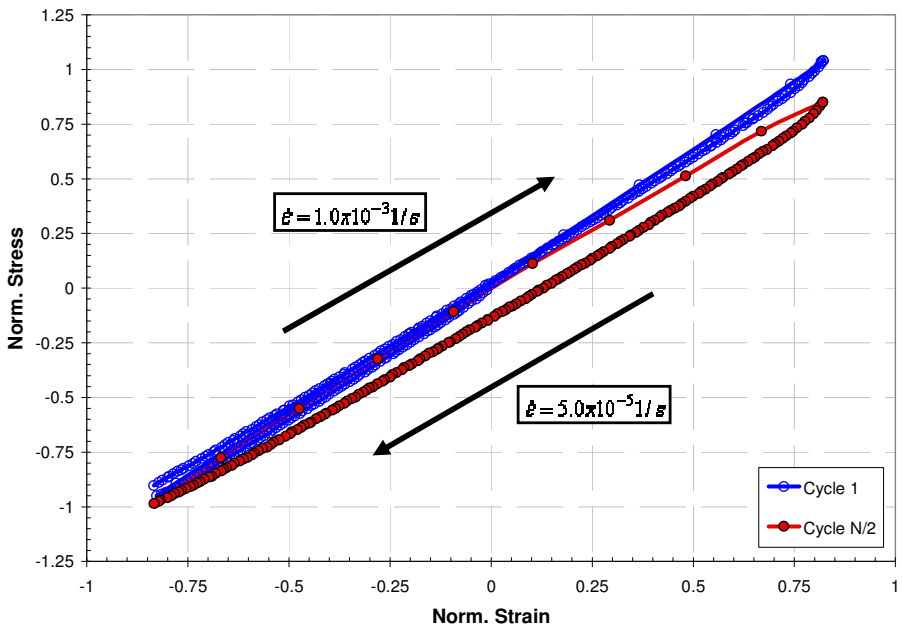

Figure 4.17: *L750 smooth specimen hysteresis with* $\dot{\varepsilon} = 1.0x10^{-3}$ *1/s loading and* $\dot{\varepsilon} = 5.0x10^{-5}$ *1/s unloading.*

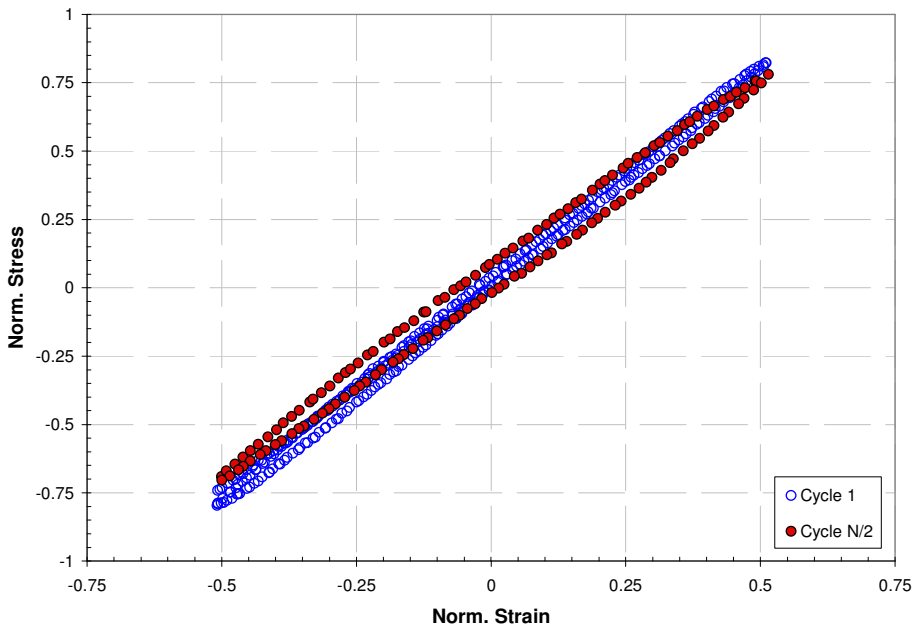

Figure 4.18: *T750 smooth specimen hysteresis at* $\dot{\varepsilon} = 5.0x10^{-5}$ *1/s.*

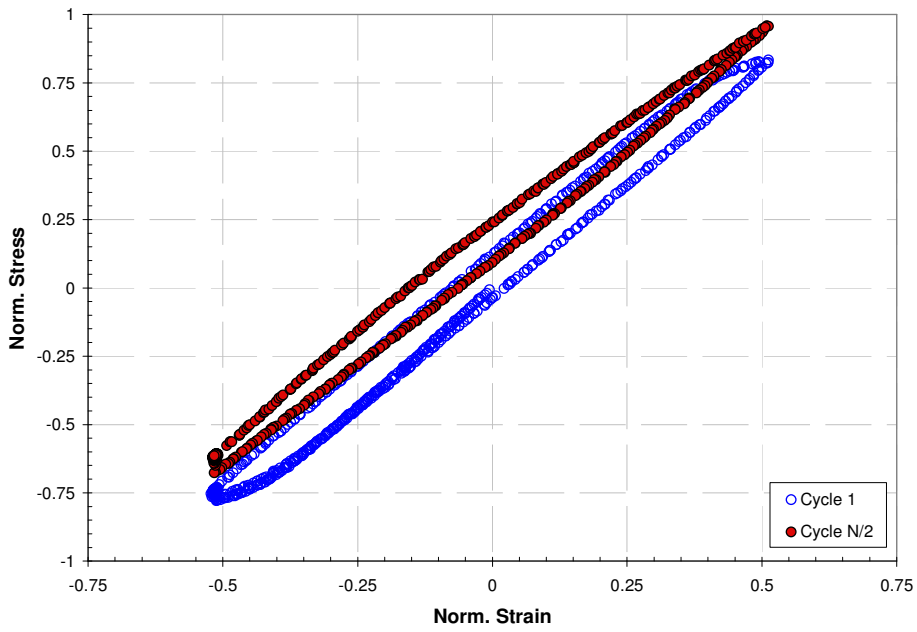

Figure 4.19: *T750 smooth specimen hysteresis with HC.*

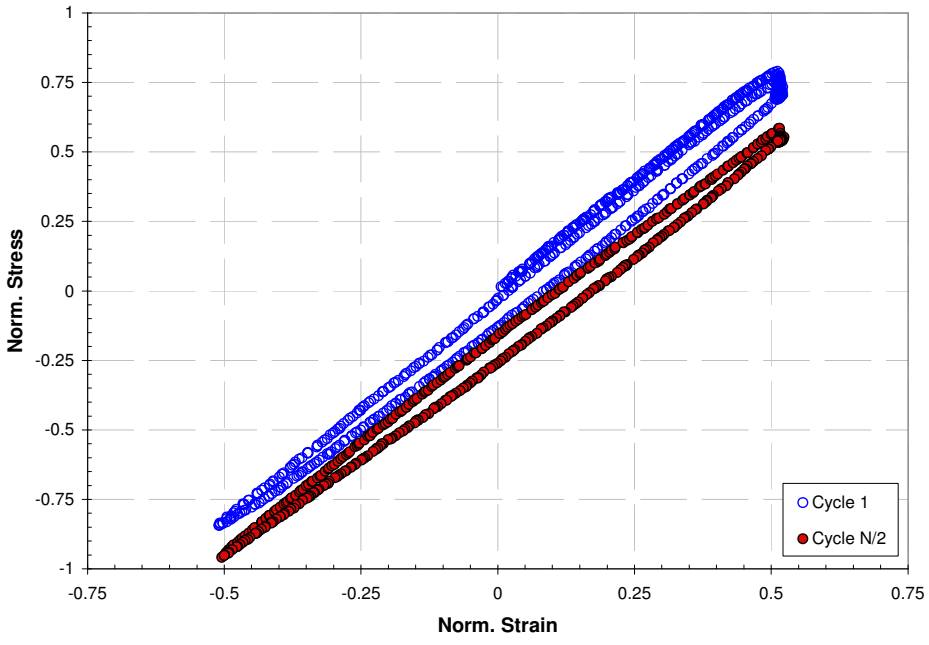

Figure 4.20: *T750 smooth specimen hysteresis with HT.*

For the L orientation at 950°*C* where time-dependent effects should be more apparent, the lives are reduced by a factor of about 4 for both SSR and HC tests. The rate effect on deformation and life is more significant at 950°*C* when compared to 750°*C*. The SSR specimen cyclically softened but developed very little mean stress as shown in Figure 4.21. In contrast, the HC specimen developed a tensile mean stress of 27% of the stress amplitude as shown in Figure 4.22. The lives of SSR and HC are similar, implying that the mean stress effect is reduced at higher temperatures and the reduction in fatigue life at 950°*C* is more controlled by rate effects.

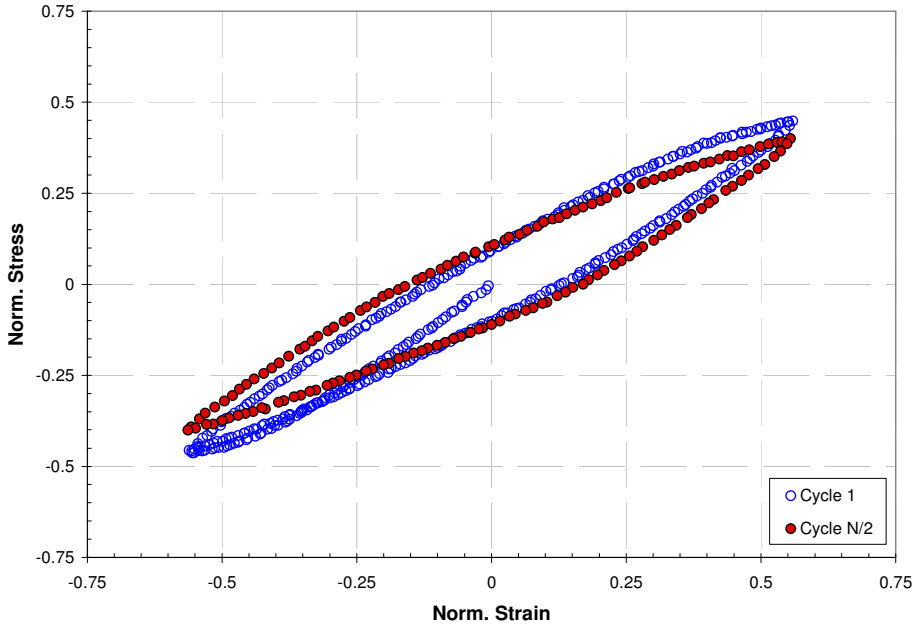

Figure 4.21: *L950 smooth specimen hysteresis at* $\dot{\varepsilon}$ *=5.0x10*$^{-5}$ *1/s.*

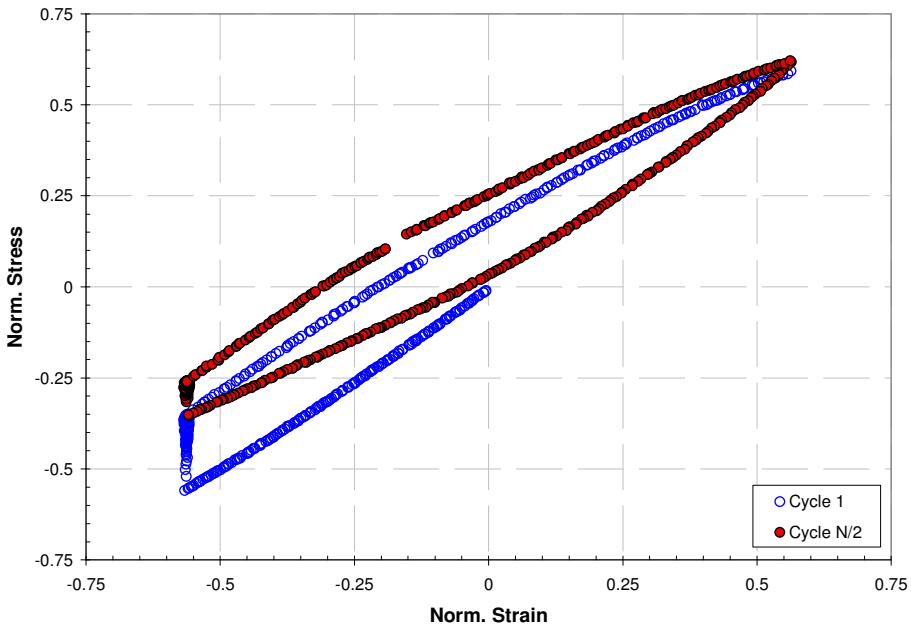

Figure 4.22: *L950 smooth specimen hysteresis with HC.*

The effects of SSR and HC on notched specimens at 750°*C* are shown in Figure 4.23 and Figure 4.24. In the L orientation, the SSR CC k_t=2 specimen showed no change in life as a result of the extended cycle time. This is consistent with the small rate-effect seen in the deformation response at 750°*C*. Life was reduced by a factor of 2 when a 10 *min* HC was added. This is likely due to a tensile mean stress that develops at the notch as a result of the compressive hold. A test with $\dot{\varepsilon}$=1.0x10^{-3} loading and $\dot{\varepsilon}$=5.0x10^{-5} was also performed on a k_t=2 specimen. This test had a longer life than the HC equivalent likely because a tensile mean stress developed at the notch. For k_t=3, the life of the SSR CC and HC are the same or perhaps even higher than the baseline. In the T orientation, the k_t=2 specimen showed no significant rate or dwell dependence on life for HC, HT, or SSR tests.

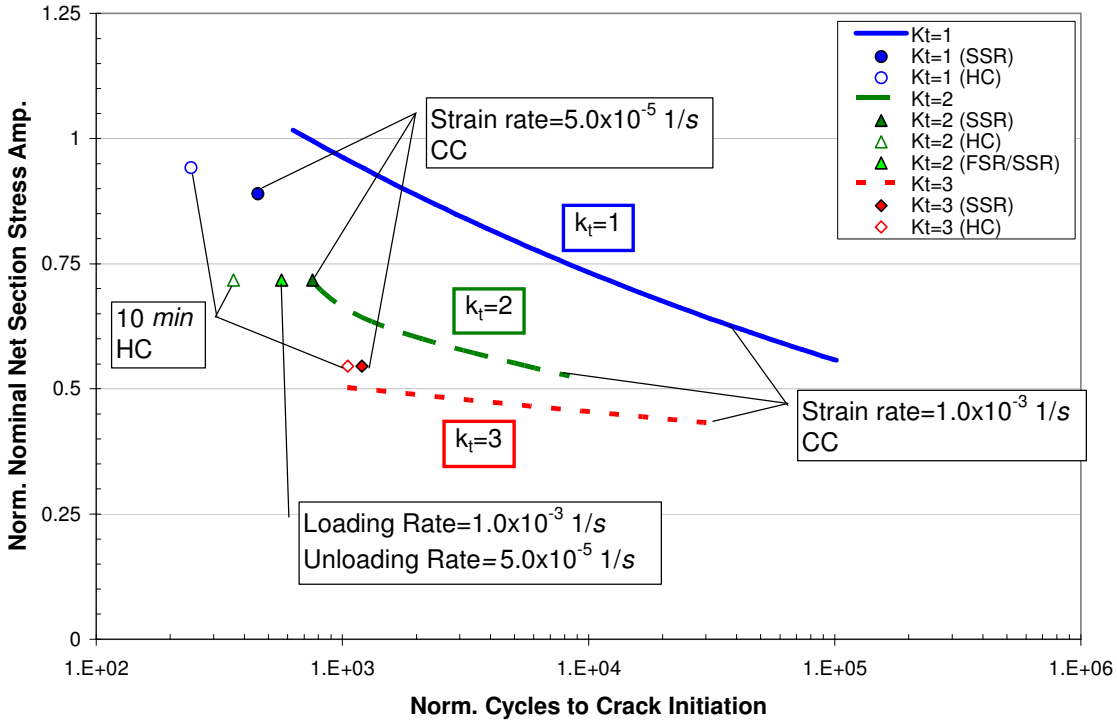

Figure 4.23: *L750 time-dependent notched specimen results.*

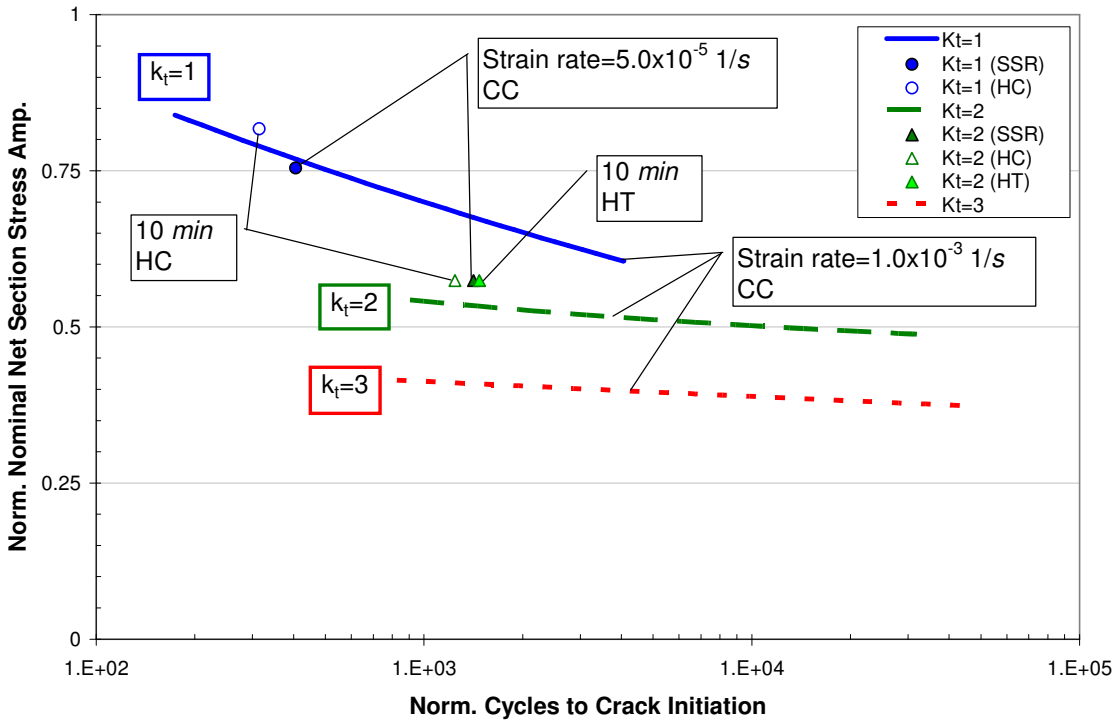

Figure 4.24: *T750 time-dependent notched specimen results.*

The time-dependent effects on the life of notched specimens at 950°*C* are shown in Figure 4.25. For k_t=2, the SSR decreases baseline CC life by a factor of 2, though the life reduction is smaller when compared to smooth specimen. The HC reduces the life by a factor of 4. A compressive strain develops as a result of creep ratcheting occurring during the hold as shown in Figure 4.26. This gross section creep only appeared during holds at 950°*C* and did not occur in the L750 tests as shown in Figure 4.27. This demonstrates that even the low stress levels outside of the stress concentration are enough to accumulate of creep strain and ratchet in the compressive direction as a result of the dwell. For k_t=3, the life reduction for both the SSR CC and HC tests was a factor of 2 from the baseline CC tests.

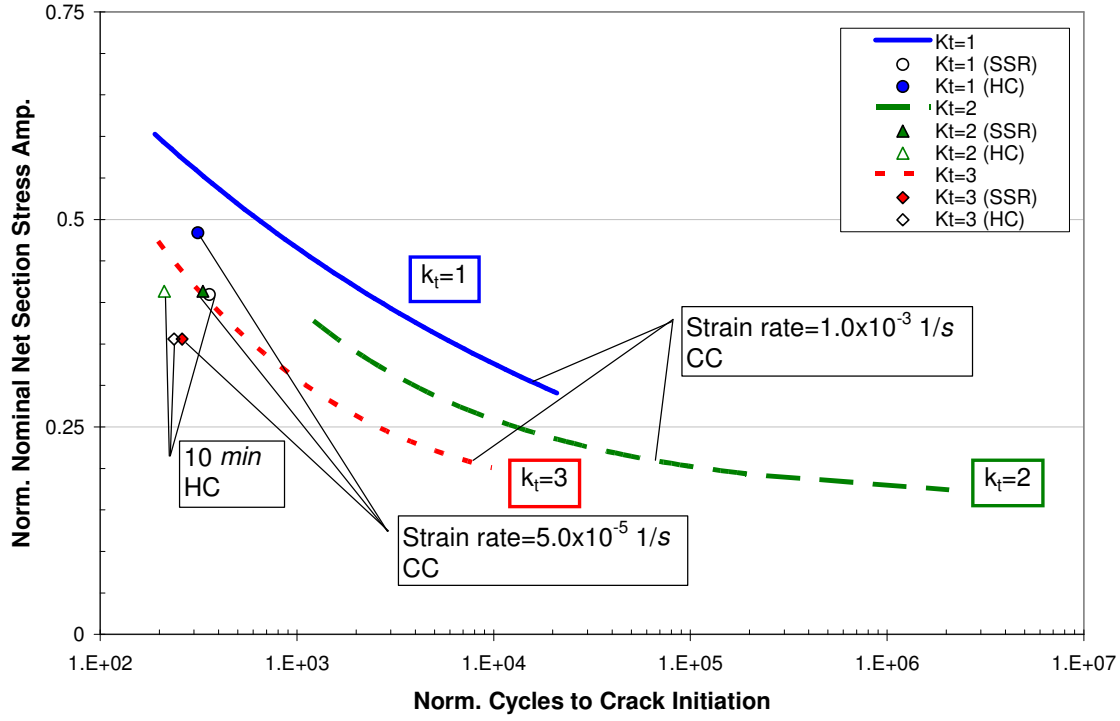

Figure 4.25: *L950 time-dependent notched specimen results.*

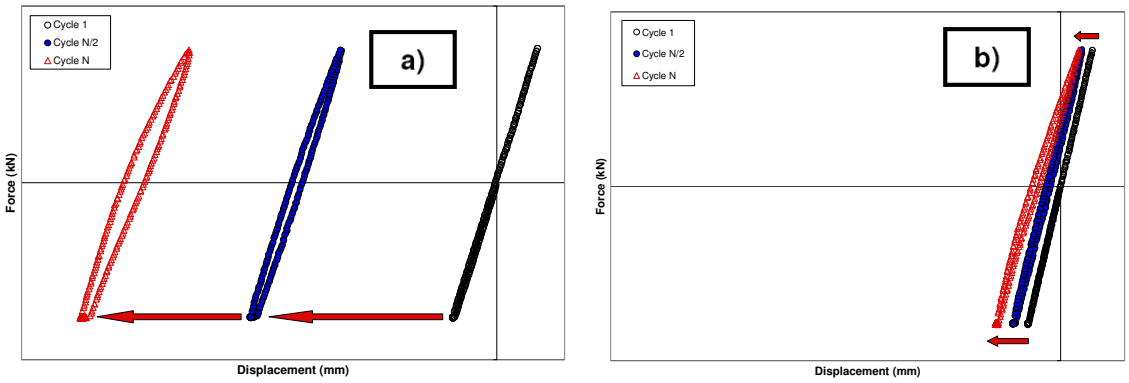

Figure 4.26: *Creep ratcheting of L950 HC a) k_t=2 specimen and b) k_t=3 specimen.*

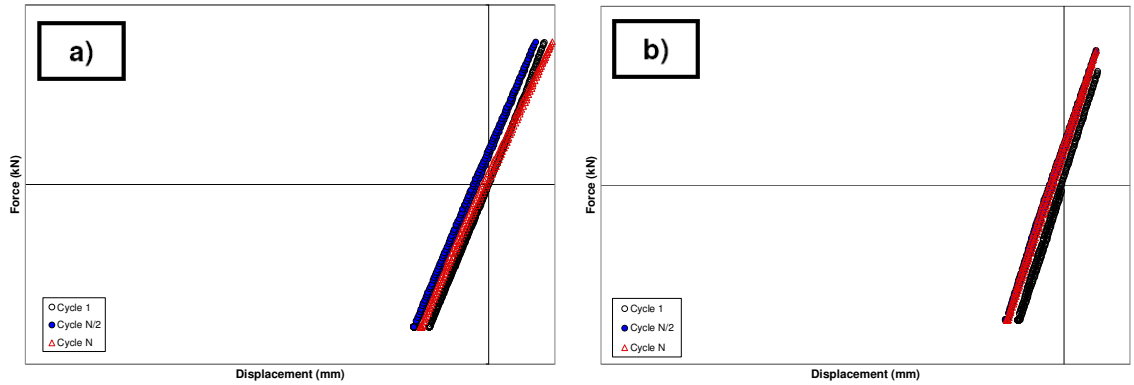

Figure 4.27: *Creep ratcheting of L750 HC a) k_t=2 specimen and b) k_t=3 specimen.*

4.4 Metallography Results

Figure 4.28 and Figure 4.29 compare the grain structures of L and T sections, respectively. The average grain size observed is 250-500 *μm* which is consistent with the literature [7].

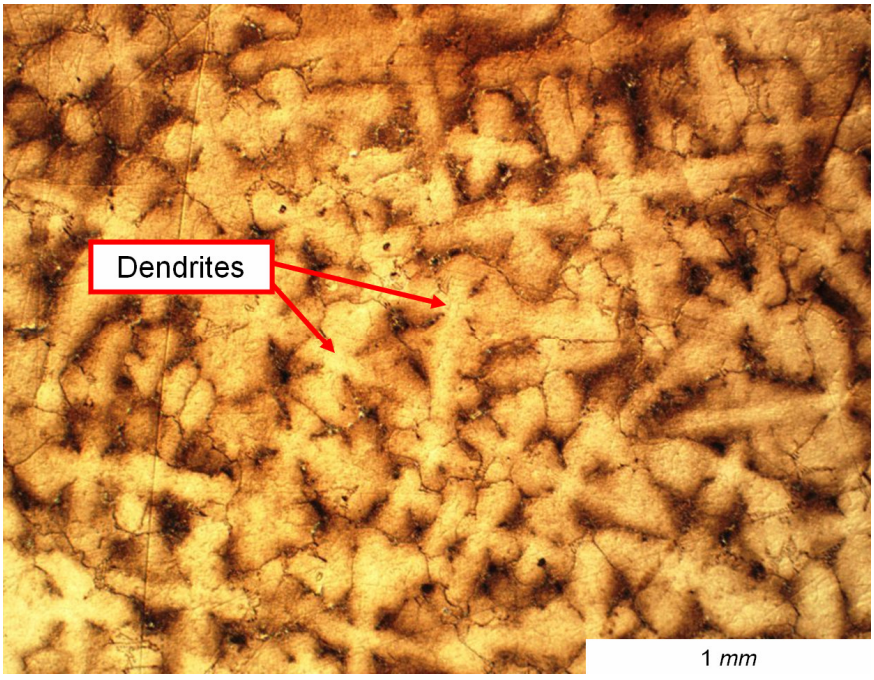

Figure 4.28: *Grain structure of cross section of L-orientated sample.*

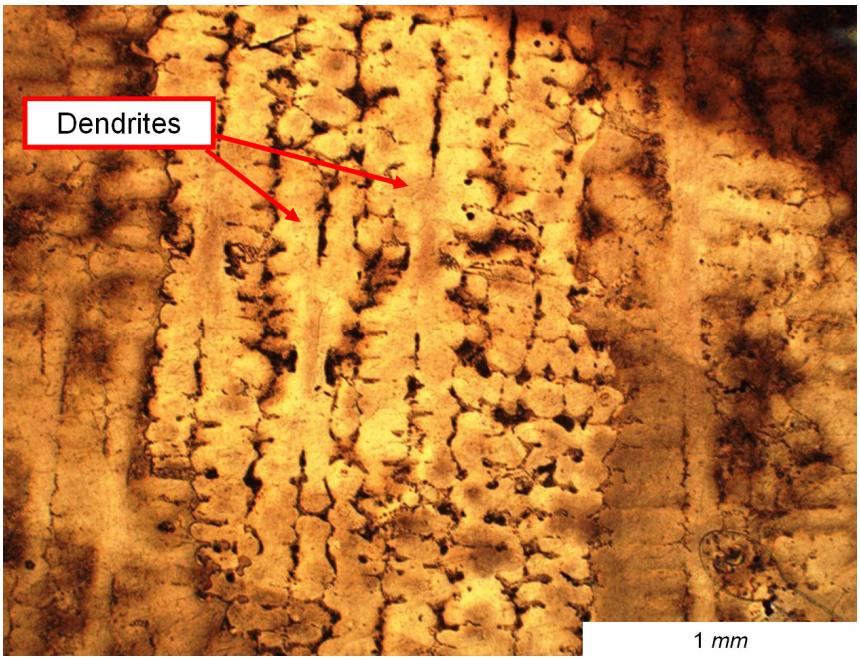

Figure 4.29: *Grain structure of cross section of T-oriented sample.*

Detailed pictures of the dendrites and interdendritic region are shown in Figure 4.30, Figure 4.31, and Figure 4.32.

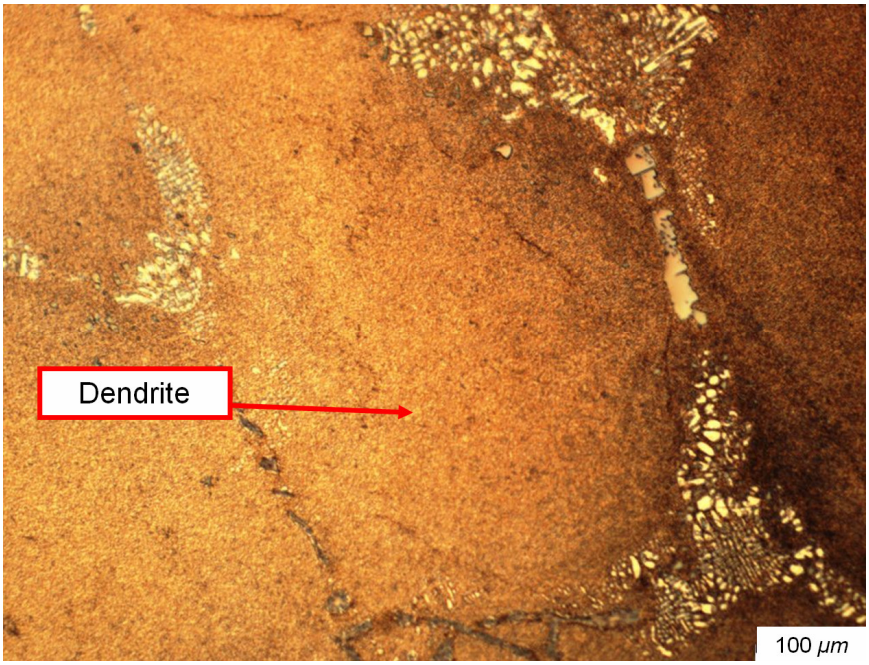

Figure 4.30: *Grain structure of cross section of L-oriented sample with interdendritic region.*

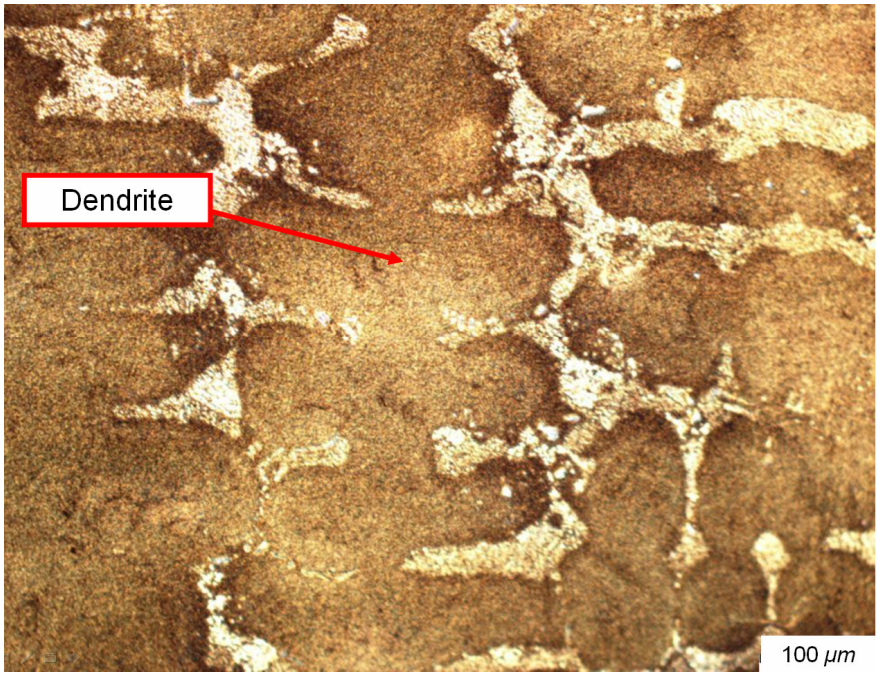

Figure 4.31: *Grain structure of cross section of T oriented sample with interdendritic region.*

Figure 4.32: *Interdendritic region of cross section of L-oriented sample.*

Images of crack sites of notched specimens are shown in Figure 4.33 to Figure 4.35. Figure 4.33a shows that the distance between two crack initiation sites of a k_t=2 specimen is 900 μm. Cracks initiate on both sides of the root of the notch as also shown in Figure 4.33b. This phenomenon is also seen in the k_t=3 specimens as shown in Figure 4.34 where cracks initiated 205 μm apart. This observation is consistent with the locations of maximum Hill's equivalent stress as discussed in Section 6.2.

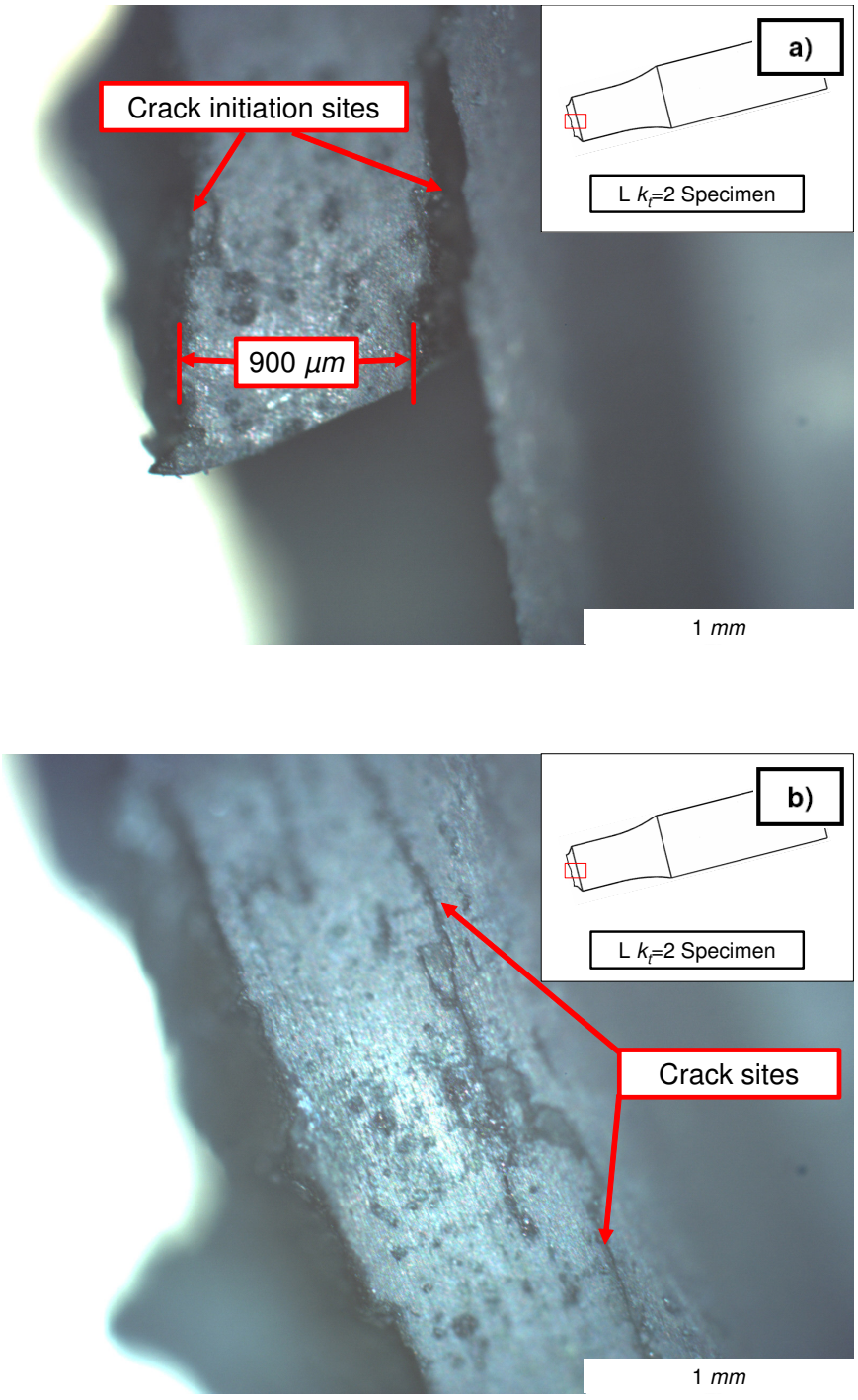

Figure 4.33: *Fracture surface of a longitudinal k_t=2 specimen.*

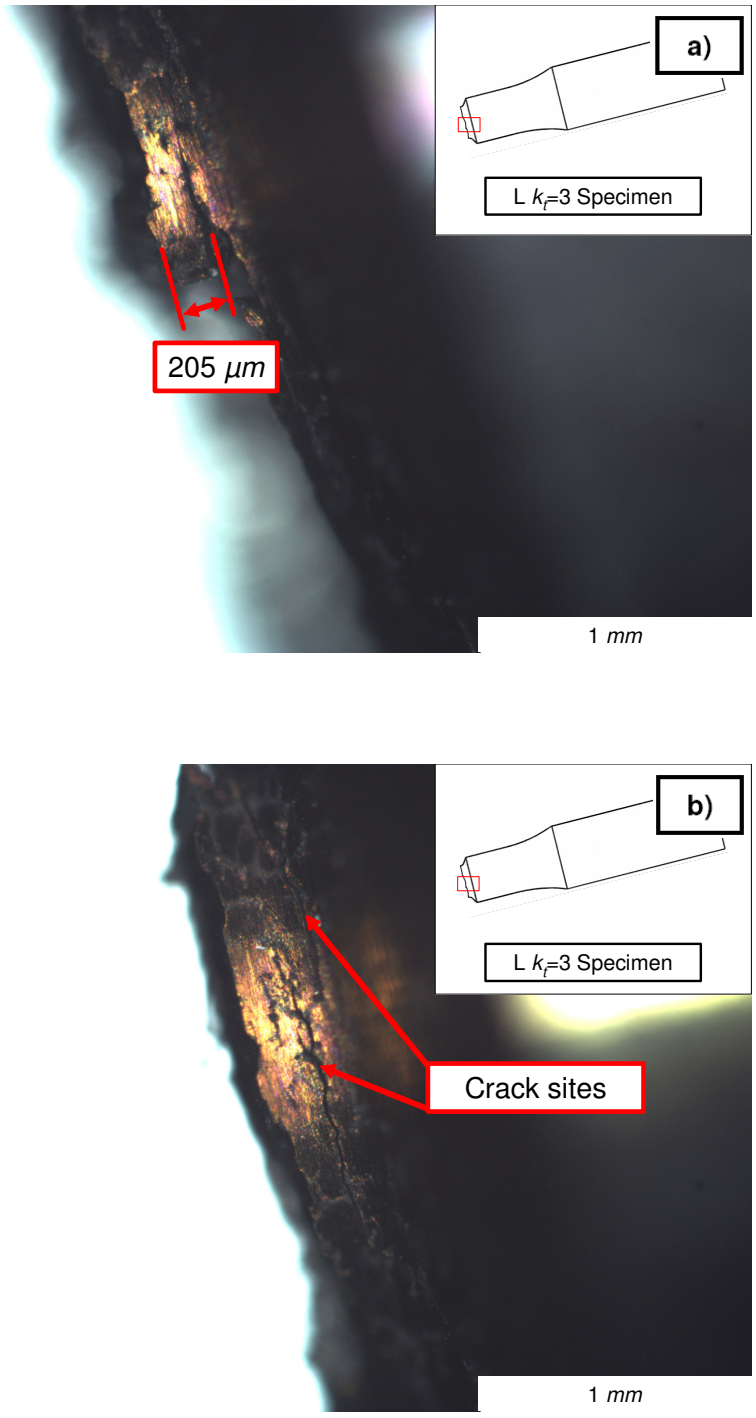

Figure 4.34: *Fracture surface of a longitudinal k_t=3 specimen.*

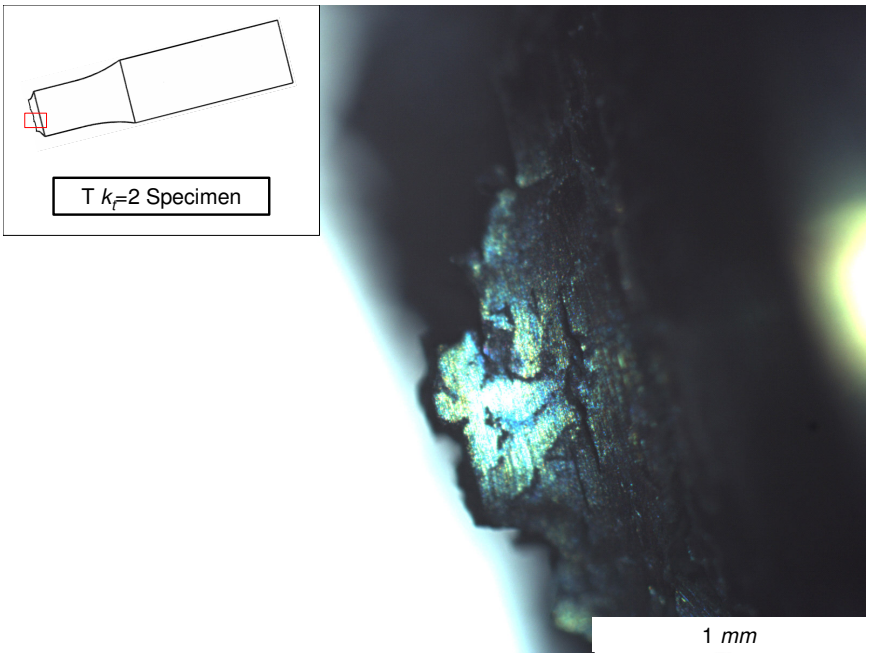

Figure 4.35: *Fracture surface of transverse k_t=2 specimen.*

Images of surface cracks of L and T smooth specimens are shown in Figure 4.36. In the T specimen, cracks nucleate at the interdendritic region.

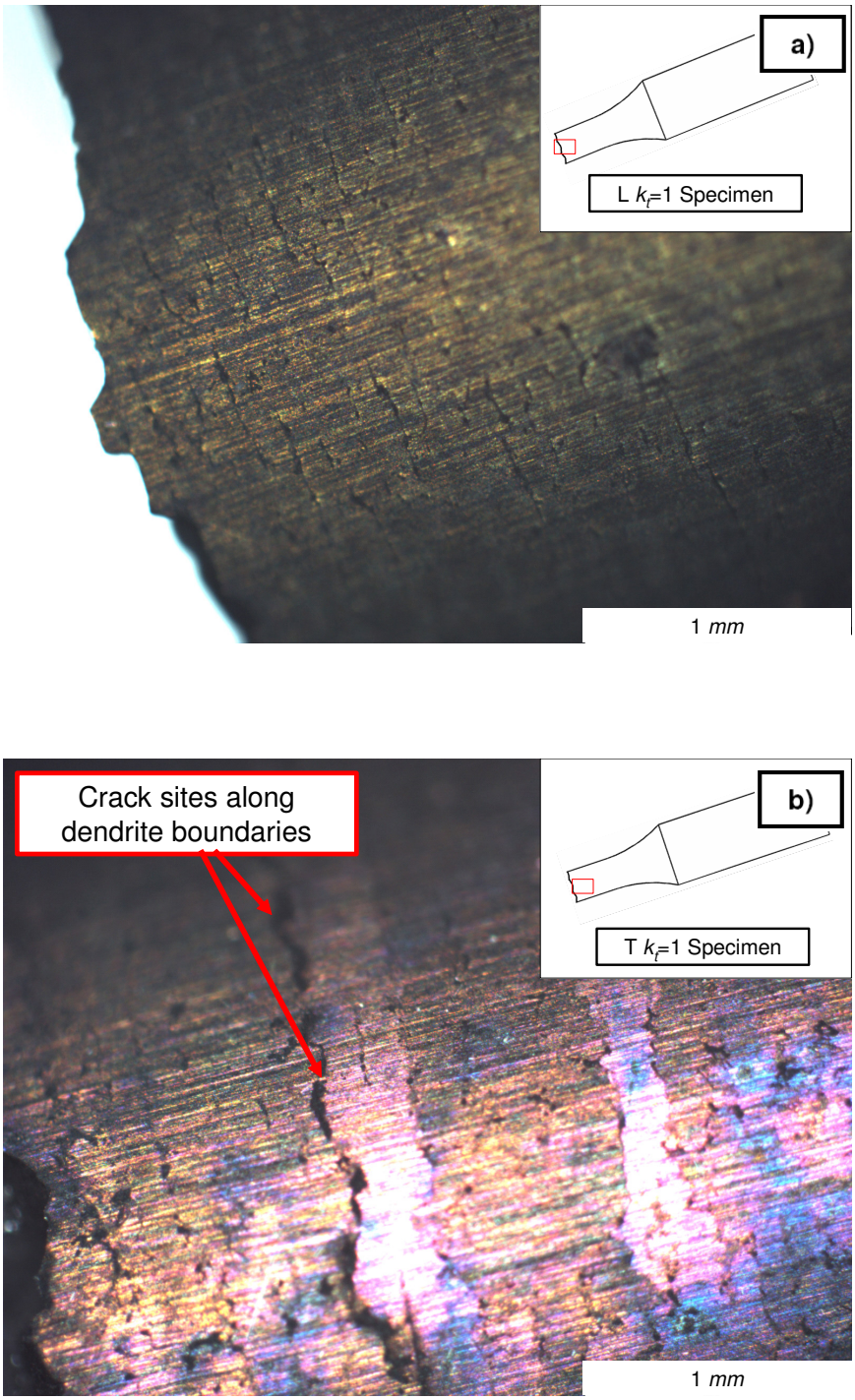

Figure 4.36: *Cracks along gage section of smooth specimen in the a) L orientation and b) T orientation.*

CHAPTER 5

ANALYTICAL MODELING

A simplified analytical model has been developed to quickly predict the stress-strain response at a notch while considering effects of high-temperature, dwells, and orientation. The model is based on a Neuber-based multiaxial constitutive model developed by Mucke and Bernhardi [2]. This multiaxial approach approximates the stress-strain response in the presence of stress concentrations. With the stress-strain response approximated a variety of life-models can be implemented. This fully three-dimensional approach is most suitable for anisotropic materials because orientation effects are considered.

5.1 Multiaxial Neuber Model

The multiaxial Neuber model [2] is a multiaxial extension of the classical Neuber analysis to three dimensions. The basis of the formulation is a multiaxial extension of the two fundamental components of the classic Neuber analysis, the Neuber rule and the stress-strain relationship.

The Neuber rule for the uniaxial case is represented as the product of the pseudo stress and strain, σ^* and ε^*, at a stress concentration determined by a linear elastic analysis is equal to the product of the actual elastic-plastic stress and strain, σ and ε,

$$\sigma^* \varepsilon^* = \sigma\varepsilon \tag{5.1}$$

The multiaxial Neuber rule for anisotropic materials comes from a tensorial generalization of the classic uniaxial Neuber hypothesis. Hoffmann and Seeger [24] applied an equivalent stress and strain leading to the modified Neuber assumption

$$\sigma_{eq}^{*}\varepsilon_{eq}^{*} = \sigma_{eq}\varepsilon_{eq} \tag{5.2}$$

A corresponding formulation for anisotropic materials can be written in tensor form [2]

$$\boldsymbol{\sigma}^{*dev} : \boldsymbol{\varepsilon}^{*}\left(\boldsymbol{\sigma}^{*dev}\right) = \boldsymbol{\sigma}^{dev} : \boldsymbol{\varepsilon}\left(\boldsymbol{\sigma}^{dev}\right) \tag{5.3}$$

where strains of the pseudo and actual elastic-plastic solution are related to the deviatoric stresses.

The stress-strain relationship often used is the Ramberg-Osgood (R-O) relation because it models the uniaxial stress-strain response well. Anisotropic materials require a generalization of this relationship for the multiaxial anisotropic case. This is done by using an anisotropic equivalent stress (σ_{eq}), which in general is given by

$$\sigma_{eq} = \sqrt{\boldsymbol{\sigma}^{dev} : \mathbf{M} : \boldsymbol{\sigma}^{dev}} \tag{5.4}$$

or using the Hill criterion, can be reduced to

$$\sigma_{eq} = \sqrt{F(\sigma_{22} - \sigma_{33})^2 + G(\sigma_{33} - \sigma_{11})^2 + H(\sigma_{11} - \sigma_{22})^2 + 2L\sigma_{23}^2 + 2M\sigma_{31}^2 + 2N\sigma_{12}^2} \tag{5.5}$$

where F, G, H, L, M, and N are material parameters. When F, G, and H are 0.5 and L, M, and N are 1.5, it reduces to the von Mises equivalent stress representing the isotropic case. In the general relation, $\boldsymbol{M}$ is a tensor of Hill parameters. There are at most six Hill parameters but for transversely isotropic material there are only three independent Hill parameters (G=F, M=L, N=F+2H). The σ_{eq} for the transversely isotropic case is given by,

$$\sigma_{eq} = \sqrt{F\left[(\sigma_{22} - \sigma_{33})^2 + (\sigma_{33} - \sigma_{11})^2\right] + H(\sigma_{11} - \sigma_{22})^2 + 2L\left(\sigma_{23}^2 + \sigma_{31}^2\right) + 2(F + 2H)\sigma_{12}^2} \tag{5.6}$$

The $\boldsymbol{M}$ tensor for this case using Voigt's matrix notation is given by,

$$[\mathbf{M}] = \begin{bmatrix} F+H & -H & -F & 0 & 0 & 0 \\ -H & H+F & -F & 0 & 0 & 0 \\ -F & -F & 2F & 0 & 0 & 0 \\ 0 & 0 & 0 & 2L & 0 & 0 \\ 0 & 0 & 0 & 0 & 2L & 0 \\ 0 & 0 & 0 & 0 & 0 & 2(F+2H) \end{bmatrix} \tag{5.7}$$

where $\boldsymbol{M}_{11}=\boldsymbol{M}_{1111}$, $\boldsymbol{M}_{22}=\boldsymbol{M}_{2222}$, $\boldsymbol{M}_{33}=\boldsymbol{M}_{3333}$, $\boldsymbol{M}_{44}=\boldsymbol{M}_{2323}$, $\boldsymbol{M}_{55}=\boldsymbol{M}_{1313}$, $\boldsymbol{M}_{66}=\boldsymbol{M}_{1212}$, etc. The 1-2 plane is the plane of isotropy and the 3 direction is the grain growth direction, as shown in Figure 5.1.

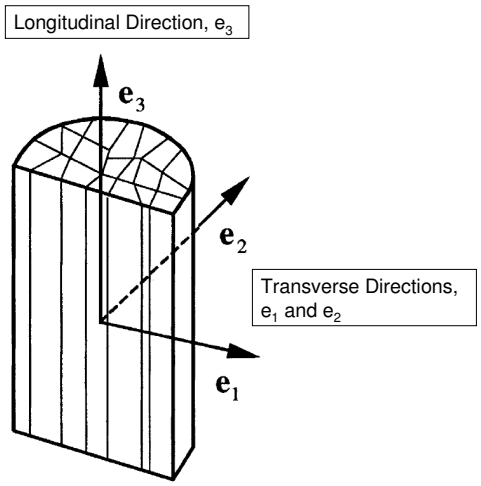

Figure 5.1: *Coordinate system diagram for DS alloy [2].*

The multiaxial Ramberg-Osgood law for anisotropic materials can be written as

$$\boldsymbol{\varepsilon} = \mathbf{H} : \boldsymbol{\sigma} + \frac{\alpha}{E_R}\left(\frac{\sigma_{eq}}{\sigma_0}\right)^{n-1} \mathbf{M} : \boldsymbol{\sigma}^{dev} \tag{5.8}$$

where the elastic anisotropy is represented by the compliance $\boldsymbol{H}$ whereas the plastic anisotropy is represented by the anisotropy tensor $\boldsymbol{M}$. E_R and σ_0 are a suitable reference stiffness and stress, respectively, and α and n are Ramberg-Osgood parameters. The elastic compliance for a transversely isotropic material can be represented as

$$[\mathbf{H}]=\begin{bmatrix} \frac{1}{E_1} & \frac{-\nu_{21}}{E_1} & \frac{-\nu_{31}}{E_3} & 0 & 0 & 0 \\ \frac{-\nu_{12}}{E_1} & \frac{1}{E_1} & \frac{-\nu_{31}}{E_3} & 0 & 0 & 0 \\ \frac{-\nu_{13}}{E_1} & \frac{-\nu_{13}}{E_1} & \frac{1}{E_3} & 0 & 0 & 0 \\ 0 & 0 & 0 & \frac{1}{G_{31}} & 0 & 0 \\ 0 & 0 & 0 & 0 & \frac{1}{G_{31}} & 0 \\ 0 & 0 & 0 & 0 & 0 & 2\left(\frac{1+\nu_{21}}{E_1}\right) \end{bmatrix} \tag{5.9}$$

This is a multiaxial representation of the stress-strain relationship. In the same manner as the classical Neuber approach, the Neuber rule and the stress-strain relationship, both now generalized to the multiaxial case, can be combined to formulate the constitutive model.

The derivation is explained in more detail in Mücke and Bernhardi [2] but an abridged approach goes as follows. The multiaxial Neuber rule states

$$\boldsymbol{\sigma}^{*\mathbf{dev}} : \boldsymbol{\varepsilon}^{*}\left(\boldsymbol{\sigma}^{*\mathbf{dev}}\right) = \boldsymbol{\sigma}^{\mathbf{dev}} : \boldsymbol{\varepsilon}\left(\boldsymbol{\sigma}^{\mathbf{dev}}\right) \tag{5.10}$$

The multiaxial stress-strain relationship can be substituted on both sides of the equation

$$\text{LHS:}\quad \boldsymbol{\varepsilon}^{*}\left(\boldsymbol{\sigma}^{*\mathbf{dev}}\right) = \mathbf{H} : \boldsymbol{\sigma}^{*\mathbf{dev}} \text{ (Hooke's law)} \tag{5.11}$$

$$\text{RHS:}\quad \boldsymbol{\varepsilon}\left(\boldsymbol{\sigma}^{\mathbf{dev}}\right) = \mathbf{H} : \boldsymbol{\sigma}^{\mathbf{dev}} + \frac{\alpha}{E_R}\left(\frac{\sigma_{eq}}{\sigma_0}\right)^{n-1} \mathbf{M} : \boldsymbol{\sigma}^{\mathbf{dev}} \quad \text{(multiaxial R-O relation)} \tag{5.12}$$

This substitution results in

$$\boldsymbol{\sigma}^{*\mathbf{dev}} : \mathbf{H} : \boldsymbol{\sigma}^{*\mathbf{dev}} = \boldsymbol{\sigma}^{\mathbf{dev}} : \mathbf{H} : \boldsymbol{\sigma}^{\mathbf{dev}} + \frac{\alpha}{E_R}\left(\frac{\sigma_{eq}}{\sigma_0}\right)^{n-1} \boldsymbol{\sigma}^{\mathbf{dev}} : \mathbf{M} : \boldsymbol{\sigma}^{\mathbf{dev}} \tag{5.13}$$

Using the definition for σ_{eq}

$$\boldsymbol{\sigma}^{*\mathbf{dev}} : \mathbf{H} : \boldsymbol{\sigma}^{*\mathbf{dev}} = \boldsymbol{\sigma}^{\mathbf{dev}} : \mathbf{H} : \boldsymbol{\sigma}^{\mathbf{dev}} + \frac{\alpha}{E_R}\sigma_{eq}^2\left(\frac{\sigma_{eq}}{\sigma_0}\right)^{n-1} \tag{5.14}$$

In order to solve this constitutive relationship the unknown elastic-plastic stress state, $\boldsymbol{\sigma}$, must be replaced by a single invariant scalar. Both the pseudo-elastic and elastic-plastic stress tensors ($\boldsymbol{\sigma}^*$ and $\boldsymbol{\sigma}$, respectively) are rewritten with a magnitude and direction

$$\sigma^* = \sqrt{\boldsymbol{\sigma}^* : \boldsymbol{\sigma}^*} \qquad \sigma = \sqrt{\boldsymbol{\sigma} : \boldsymbol{\sigma}} \tag{5.15}$$

$$\mathbf{D}^* = \frac{\boldsymbol{\sigma}^*}{\sigma^*} \qquad \mathbf{D} = \frac{\boldsymbol{\sigma}}{\sigma} \tag{5.16}$$

where $\boldsymbol{D}^*$ is the pseudo-elastic stress direction tensor and $\boldsymbol{D}$ is the elastic-plastic stress direction tensor and σ^* and σ are their corresponding magnitudes. In the same manner the σ_{eq}, $\boldsymbol{\sigma}^{*dev}$, and $\boldsymbol{\sigma}^{dev}$, can be written in terms of tensor directions and scalar magnitudes

$$\sigma_{eq} = \sqrt{\boldsymbol{\sigma}^{\mathbf{dev}} : \mathbf{M} : \boldsymbol{\sigma}^{\mathbf{dev}}} = \left(\sqrt{\mathbf{D}^{\mathbf{dev}} : \mathbf{M} : \mathbf{D}^{\mathbf{dev}}} \right) \sigma \tag{5.17}$$

$$\boldsymbol{\sigma}^{*\mathbf{dev}} : \mathbf{H} : \boldsymbol{\sigma}^{*\mathbf{dev}} = \left(\mathbf{D}^{*\mathbf{dev}} : \mathbf{H} : \mathbf{D}^{*\mathbf{dev}} \right) \sigma^{*2} \tag{5.18}$$

$$\boldsymbol{\sigma}^{\mathbf{dev}} : \mathbf{H} : \boldsymbol{\sigma}^{\mathbf{dev}} = \left(\mathbf{D}^{\mathbf{dev}} : \mathbf{H} : \mathbf{D}^{\mathbf{dev}} \right) \sigma^2 \tag{5.19}$$

An important assumption is that Neuber hypothesis is limited to localized plasticity. Stress redistribution due to gross plastic flow is negligible. For this reason, it is reasonable to assume that the same stress direction tensor applies for both the pseudo-elastic and elastic-plastic solution,

$$\mathbf{D} = \mathbf{D}^* \tag{5.20}$$

With these final substitutions Eq. 5.14 becomes,

$$\left(\mathbf{D}^{*\mathbf{dev}} : \mathbf{H} : \mathbf{D}^{*\mathbf{dev}} \right) \sigma^{*2} = \left(\mathbf{D}^{*\mathbf{dev}} : \mathbf{H} : \mathbf{D}^{*\mathbf{dev}} \right) \sigma^2 + \frac{\alpha}{E_R} \left(\mathbf{D}^{*\mathbf{dev}} : \mathbf{M} : \mathbf{D}^{*\mathbf{dev}} \right) \sigma^2 \left(\frac{\left(\sqrt{\mathbf{D}^{*\mathbf{dev}} : \mathbf{M} : \mathbf{D}^{*\mathbf{dev}}} \right) \sigma}{\sigma_0} \right)^{n-1} \tag{5.21}$$

If the pseudo-elastic stress state and material properties are known, the only unknown is σ. This magnitude can be solved by iteration. From this value the actual elastic-plastic stress state is determined using Eq. 5.16 and Eq. 5.20,

$$\boldsymbol{\sigma} = \mathbf{D}^{*}\sigma \tag{5.22}$$

and the strain state is determined from Eq. 5.8,

$$\boldsymbol{\varepsilon} = \mathbf{H} : \boldsymbol{\sigma} + \frac{\alpha}{E_R}\left(\frac{\sigma_{eq}}{\sigma_0}\right)^{n-1} \mathbf{M} : \boldsymbol{\sigma}^{dev} \tag{5.23}$$

The final output of this method is the local stress and strain state in tensor form, fully generalized for multiaxial loading and anisotropic materials.

The multiaxial Neuber-based approach was coded using MATLAB [47]. This allowed for easy modifications to quickly investigate and validate the multiple facets of the model. A formatted spreadsheet fed all the necessary inputs into the program.

The model requires inputs for the pseudo-elastic stress state in tensor form and the material behavior, which include the tensor of elastic compliance (***H***), anisotropy tensor (***M***), reference modulus and stress (E_R and σ_0, respectively), and Ramberg-Osgood parameters (α and n). For transversely isotropic materials there are only five independent elastic parameters and three independent Hill parameters. Four Ramberg-Osgood parameters are necessary but not all of the parameters are independent. A summary of the required parameters is given in Table 5.1.

Table 5.1: *Multiaxial Neuber-based model inputs.*

Material Properties:

Elastic

$\boldsymbol{H}(E_1, E_3, \nu_{21}=\nu_{12}, \nu_{31}=(E_3/E_1)\nu_{13}, G_{31})$

Plastic

$\boldsymbol{M}(F, H, L)$, Hill parameters

Reference stress and modulus

- σ_0 = Reference stress
- E_R = Reference modulus

Ramberg-Osgood parameters

- α = Flow parameter
- n = Flow exponent

Elastic Stress State:

$\boldsymbol{\sigma}^*$, Linear elastic solution (pseudo-elastic solution)

For a transversely isotropic material, the Hill parameters can be obtained from three uniaxial tests, one in the L direction, one in the T direction, and one in an off-axis direction (e.g., 45° orientation). The Hill parameters are calculated relative to the L orientation, therefore F is assumed to equal ½ and H is dependent on the yield strengths in the L direction (σ_{YS}^{L}) and T direction (σ_{YS}^{T}),

$$H = \left(\frac{\sigma_{YS}^{L}}{\sigma_{YS}^{T}}\right)^2 - \frac{1}{2} \tag{5.24}$$

L can be determined by an off-axis test (e.g., 45° orientation),

$$L = 2\left(\frac{\sigma_{YS}^{L}}{\sigma_{YS}^{45}}\right)^2 - \frac{1}{2}\left(\frac{\sigma_{YS}^{L}}{\sigma_{YS}^{T}}\right)^2 \tag{5.25}$$

where σ_{YS}^{45} is the yield strength in the 45° direction.

This approach requires modifications to incorporate the effects of temperature and rate dependencies. Temperature dependence can be captured by defining material parameters as a function of temperature. Both the elastic response as well as the Hill and R-O parameters can depend on temperature. A temperature dependent life model can be used to relate the temperature dependent material response to life, fully integrating temperature dependence into the model.

The multiaxial Ramberg-Osgood law was tested to ensure that the stress-strain response of CM247LC DS was appropriately modeled. The multiaxial R-O relation does not reduce exactly to the uniaxial equivalent in the L and T directions. This is because the same flow parameter, *n*, is used for both the L and T directions. The Hill parameters account for the change in yield behavior for different orientations. The cyclic R-O fits explained in Chapter 4 can be implemented into analytical model to capture the cyclic behavior of the material at a variety of temperatures. The multiaxial R-O model in the L orientation is given as,

$$\varepsilon_{33} = \frac{\sigma_{33}}{E_3} + \frac{\alpha}{E_R}\left(\frac{1}{\sigma_0}\right)^{n-1}\sigma_{33}^{n} \tag{5.26}$$

To solve for α and *n*, this equation is set equal to the cyclic R-O relation for the L orientation,

$$\alpha = \frac{E_R}{\sigma_0}\left(\frac{\sigma_0}{K'}\right)^{1/n^*} \text{ and } n = \frac{1}{n^*} \tag{5.27}$$

where n^* is the R-O exponent from Eq. 2.17. The multiaxial R-O fit is independent of σ_0 and E_R. For this study, E_R was set to E_3 (elastic modulus in the L direction) and σ_0 is σ_{YS}^L (yield strength in the L direction). Figure 5.2 demonstrates that the multiaxial Ramberg-Osgood model captures the experimental stress-strain response in both L and T directions well.

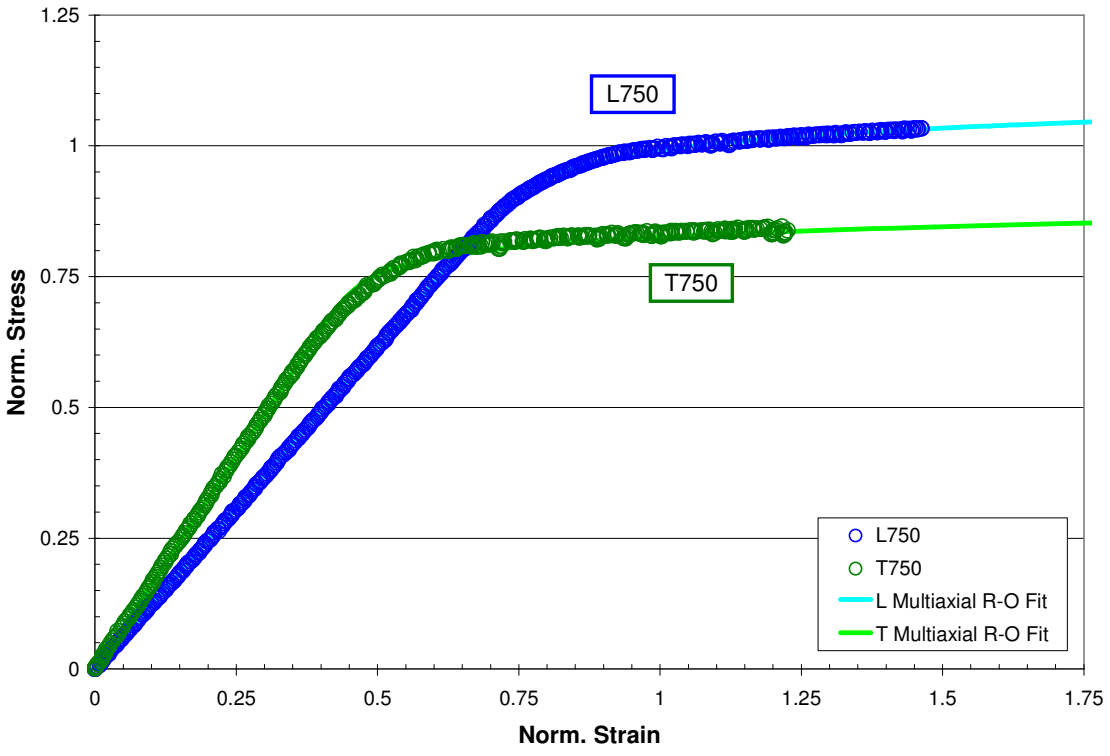

Figure 5.2: *Multiaxial Ramberg-Osgood fits for L750 and T750.*

The above method relates the linear elastic solution providing the pseudo stress and strain to an approximate elastic-plastic solution via a multiaxial Neuber-based approach. This elastic-plastic stress-strain state can be interpreted as stress and strain amplitude and applied to cyclic loading to estimate fatigue life. Masing's behavior [48] is assumed where the cyclic response is twice the monotonic response. This is analogous to the extension of the uniaxial Neuber rule to fatigue problems demonstrated in Section 2.4. For initial demonstration, the tensile-based critical plane multiaxial fatigue parameter, the Smith-Watson-Topper (SWT) parameter [49], will be used to correlate the loading condition at a critical point to fatigue life. This one is selected because it is the simplest approach that considers the effect of mean stress. The driving force for fatigue crack initiation is the product of maximum normal stress and total strain amplitude on the critical plane,

$$SWT = \sigma_{\max} \varepsilon_a \tag{5.28}$$

Cycles to crack initiation is assumed to be a function of SWT. The critical value of SWT, SWT_{crit}, captures the anisotropy of the material resistance. This anisotropy arises from the tendency of fatigue cracks to form along weak planes in the microstructure (e.g., along interdendritic channels). $SWT_{crit}(\omega,T)$, the critical value for any orientation, is written in terms of $SWT_{crit}(0°,T)$, the critical value for the L orientation, and a function $f(\omega,T)$ that depends on both orientation (ω) and temperature (T)

$$SWT_{crit}(\omega,T) = f(\omega,T) SWT_{crit}(0°,T) \tag{5.29}$$

The factor ω is the angle measured from the L direction (i.e., 0° is the L direction and 90° is the T orientation) and is used to account for orientation effects. The function $f(\omega,T)$ is determined using smooth specimen life data in different orientations (e.g., 0°, 45°, 90°). For CM247LC DS, Siemens data along with some limited data in the literature was used [5, 15]. DS Ni-base superalloys exhibit the trend: $N_i(45°) < N_i(90°) < N_i(0°)$. Figure 2.3 shows that orientation has little effect on the slope of the $\Delta\varepsilon$-N_f curves and that an orientation dependent scalar (i.e., f) should accurately account for the orientation effect. A sixth order polynomial is used to best fit the $f(\omega,T)$

$$f(\omega,T) = f_6(T)\omega^6 + f_5(T)\omega^5 + f_4(T)\omega^4 + f_3(T)\omega^3 + f_2(T)\omega^2 + 1 \qquad (5.30)$$

where ω is in *radians* and T is in $°C$. The polynomial is fit by determining values of $f(0°,T)$, $f(45°,T)$, and $f(90°,T)$ as well as fixing $f'(0°,T)$, $f'(45°,T)$, $f'(90°,T)$, and $f''(67.5°,T)$ to zero so there are enough conditions to solve analytically. Figure 5.3 shows $f(\omega,500°C)$.

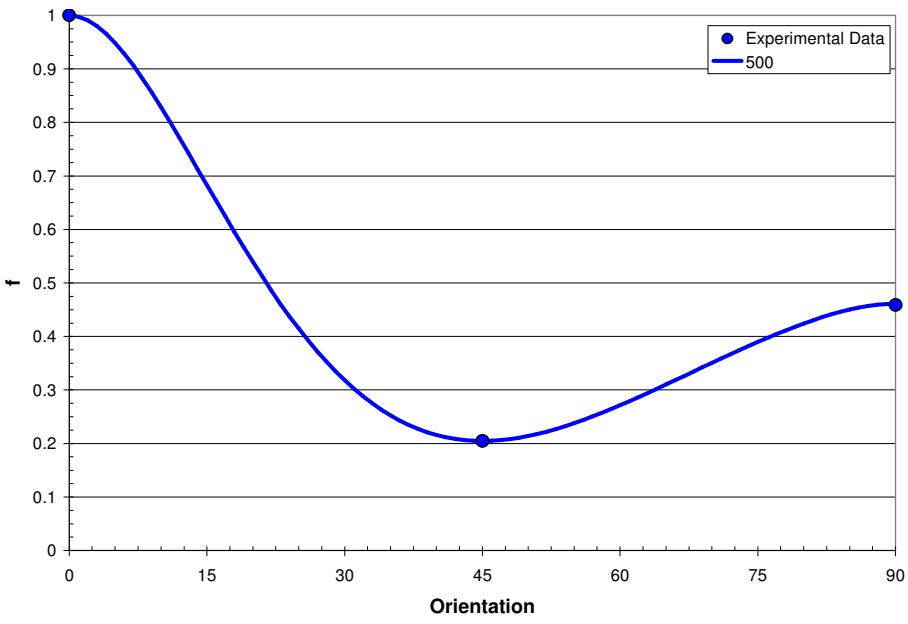

Figure 5.3: *f(ω,500°C) using experimental data from Siemens, Georgia Tech, Erickson and Harris [5], and Bernhardi and Mücke [50].*

Initially a power fit, similar to a Coffin-Manson type relationship, is used to describe the life curve:

$$SWT_{crit}(0°,T) = A(T)(2N_i)^{b(T)} \tag{5.31}$$

Alternatively, a double power fit, such as one derived from the product of the Basquin and Coffin-Manson relationships, can be used,

$$SWT_{crit}(0°) = \frac{(\sigma'_f(T))^2}{E(T)}(2N_i)^{2b(T)} + \sigma'_f(T)\varepsilon'_f(T)(2N_i)^{b(T)+c(T)} \tag{5.32}$$

The simpler single power fit will be used because it yields nearly identical predictions as the double power fit but without the complexity of iterative solving.

The SWT parameter is used in the critical plane approach. Stress and strain tensors are iteratively transformed in 5° increments over all three dimensions. The transformations are denoted by three Euler angles (ψ,θ,φ), which represent rotations about (1) the global X-axis, (2) the new local Y'-axis, and (3) the new local Z''-axis, respectively. The rotation matrix is given by $\boldsymbol{R}$,

$$[\mathbf{R}] = \begin{bmatrix} \cos\theta\cos\phi & \cos\theta\sin\phi & -\sin\theta \\ \sin\psi\sin\theta\cos\phi - \cos\psi\sin\phi & \sin\psi\sin\theta\sin\phi + \cos\psi\cos\phi & \cos\theta\sin\psi \\ \cos\psi\sin\theta\cos\phi + \sin\psi\sin\phi & \cos\psi\sin\theta\sin\phi - \sin\psi\cos\phi & \cos\theta\cos\psi \end{bmatrix} \quad (5.33)$$

where the transformed stress or strain tensor ($\overline{\boldsymbol{\sigma}}$ and $\overline{\boldsymbol{\varepsilon}}$, respectively) is given by,

$$\overline{\boldsymbol{\sigma}} = \mathbf{R} \cdot \boldsymbol{\sigma} \cdot \mathbf{R}^T \text{ and } \overline{\boldsymbol{\varepsilon}} = \mathbf{R} \cdot \boldsymbol{\varepsilon} \cdot \mathbf{R}^T \quad (5.34)$$

The angle between the trial critical plane's normal and the L direction, as illustrated in Figure 5.4, is used to calculate ω, which is then used to calculate f for each plane. A SWT value is calculated for each plane and the maximum value is chosen and the corresponding plane is identified as the critical plane. The critical plane SWT approach was coded into a MATLAB [47] function within the MNM program.

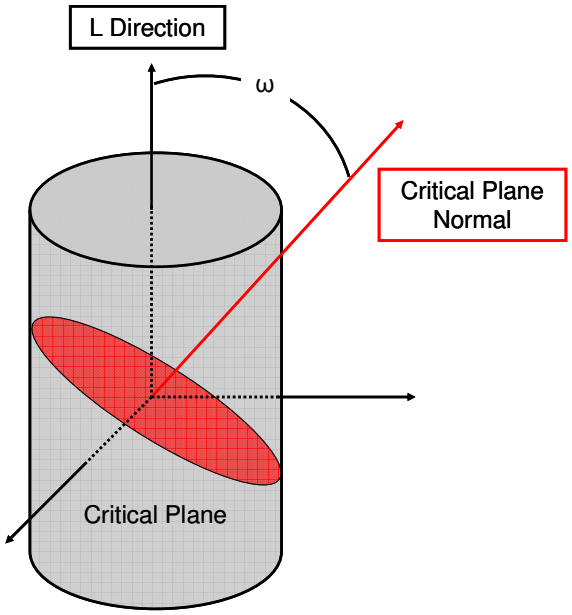

Figure 5.4: *Critical plane approach diagram.*

To account for the notch size effect, a simple critical distance approach is used. Larger notches result in a larger highly stressed volume. This effect is accounted for by correlating life to the cyclic response at a critical distance away from the notch root. L was determined by fitting the non-local life predictions to experimental data. This non-local approach should account for the notch size effect, predicting both k_t=2 and k_t=3 notches. The use of a non-local approach is analogous to the use of k_f instead of k_t in uniaxial notch analysis. The use of k_t is the equivalent to using the elastic stress response (pseudo stress), whereas the use of k_f results in a reduced pseudo stress. The MNM requires only one pseudo stress state, to more accurately predict the life at a notch an averaged pseudo stress needs to be used. For 3D geometries, predictions using volume method were just the same as from point method, line method, and area method [38]. The slight increase in accuracy is not worth the additional computational complexity, so the simplest approaches, point method and line method, are used. The focus path concept

[38] is used where the critical regions are chosen as likely areas of fatigue failure. Locations of maximum Hill's equivalent stress were used because the MNM uses this condition.

In summary, the multiaxial model is based on a multiaxial Ramberg-Osgood model that captures the stress-strain response and a multiaxial Neuber rule that captures the cyclic elastic-plastic response near the stress concentration. A critical distance approach captures the size effect at a notch. Finally, a SWT parameter is used to relate the local cyclic stress-strain response to a fatigue life. Anisotropy of the microstructure is accounted for both in the driving force and material resistance relationships.

5.2 Anisotropic Elastic Finite Element Model

Linear elastic modeling is necessary for the analytical model to provide the pseudo-elastic response at the notch. Anisotropy of the material must be considered because it is a multiaxial model. For this reason, a transversely isotropic elastic model of the notched specimens was performed.

Transversely isotropic materials have five independent elastic constants: two elastic moduli (E_1 and E_3), two Poisson's ratios (ν_{12} and ν_{13}), and one shear modulus (G_{31}), where the isotropic plane is defined by the 1-2 directions. From these five constants, the entire compliance matrix can be determined

$$\begin{bmatrix} \frac{1}{E_1} & \frac{-\nu_{21}}{E_1} & \frac{-\nu_{31}}{E_3} & 0 & 0 & 0 \\ \frac{-\nu_{12}}{E_1} & \frac{1}{E_1} & \frac{-\nu_{31}}{E_3} & 0 & 0 & 0 \\ \frac{-\nu_{13}}{E_1} & \frac{-\nu_{13}}{E_1} & \frac{1}{E_3} & 0 & 0 & 0 \\ 0 & 0 & 0 & \frac{1}{G_{31}} & 0 & 0 \\ 0 & 0 & 0 & 0 & \frac{1}{G_{31}} & 0 \\ 0 & 0 & 0 & 0 & 0 & 2\left(\frac{1+\nu_{21}}{E_1}\right) \end{bmatrix} \tag{5.35}$$

Here, the longitudinal axis is the third axis. Due to orthotropic symmetry

$$\nu_{21} = \nu_{12} \text{ and } \nu_{31} = \frac{E_3}{E_1}\nu_{13} \tag{5.36}$$

For CM247LC DS, most of these parameters were calculated using experimental data. Some Poisson's ratios were not available from experimental data, so the values for MarM247 DS were used instead [2]. A detailed study of the elastic anisotropy of DS superalloys, including MarM247LC DS, has been performed by Hasebe et al. [51]. The elastic parameters for CM247LC DS are given in Table 5.2.

Table 5.2: *CM247LC DS elastic parameters.*

Elastic Property	500°C	750°C	850°C	950°C
E_1 (MPa)	152550	134523	132200	119517
E_2 (MPa)	152550	134523	132200	119517
E_3 (MPa)	111280	102203	92520	85819
ν_{12}	0.175	0.175	0.175	0.175
ν_{13}	0.561	0.585	0.594	0.601
ν_{21}	0.175	0.175	0.175	0.175
ν_{23}	0.561	0.585	0.594	0.601
ν_{31}	0.409	0.445	0.416	0.431
ν_{32}	0.409	0.445	0.416	0.431
G_{12} (MPa)	64915	57244	56255	50858
G_{23} (MPa)	110600	99700	94300	87500
G_{31} (MPa)	110600	99700	94300	87500

The anisotropic elastic analysis was performed in both L and T directions using a high density mesh consisting of ~1.7 million 4-noded three-dimensional, linear, solid tetrahedral elements designated as C3D4 by ABAQUS [46]. The mesh used for elastic analysis is shown in Figure 5.5. The stresses through the net section for the L orientation for two different stress concentrations are shown in Figure 5.6. Figure 5.6 demonstrates the difference between the stress profiles of k_t=2 and k_t=3 in the L orientation. A much sharper stress gradient is observed at the sharper k_t=3 notch. The Hill's equivalent stress demonstrates the propensity of the material to yield while considering anisotropy. Even though k_t=3 is a sharper notch, the larger k_t=2 notch has a higher Hill's effective stress from a point 90 μm and deeper into the notch. For a T oriented specimen, the highest stresses at the notch are seen in the short T direction because of the higher stiffness as shown in Figure 5.7.

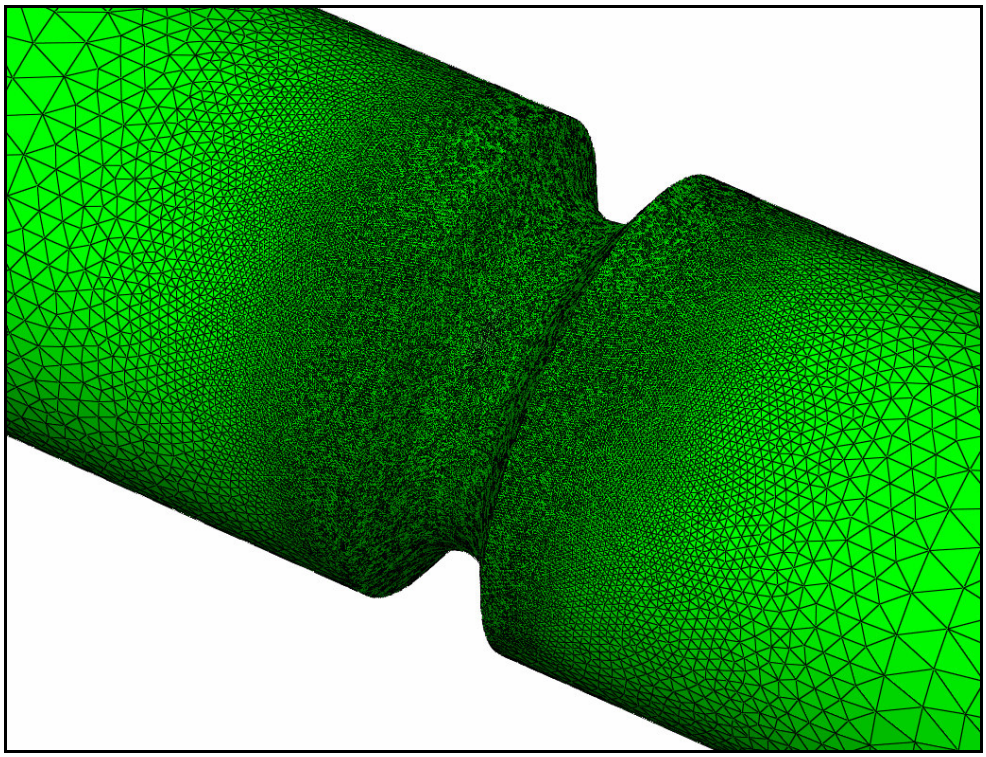

Figure 5.5: *Anisotropic elastic finite element mesh.*

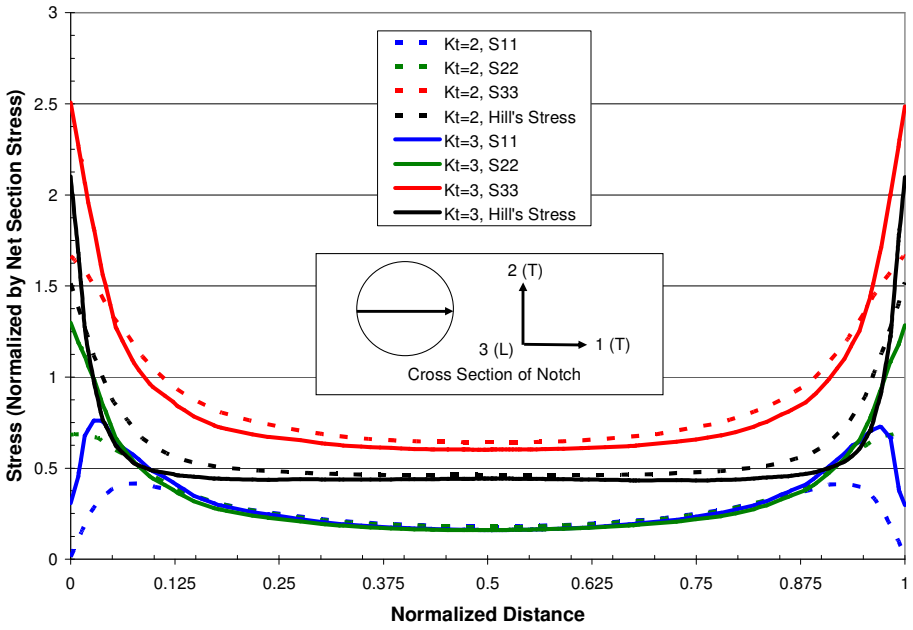

Figure 5.6: *Stresses for longitudinal k_t=2 and k_t=3 specimens across the notch net-section.*

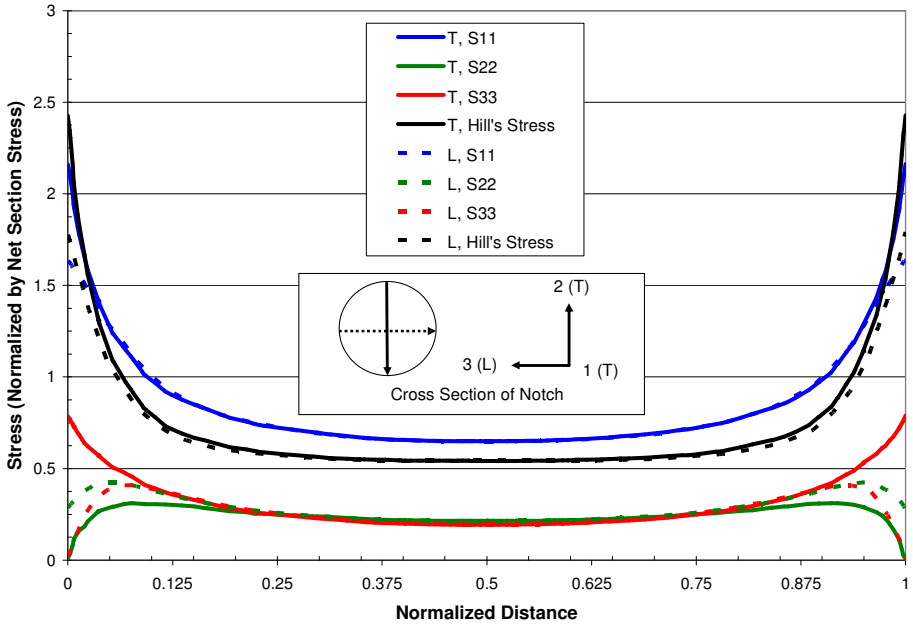

Figure 5.7: *Stresses for transverse k_t=2 specimen across the notch net-section in L and T directions.*

The Hill's stress in the vicinity of the notch root shows that the most critically stressed regions may not be at the root of the notch. The highly stressed region is 490 μm offset vertically from the center of the k_t=2 notch and 170 μm from the k_t=3 notch at L750 conditions. This phenomenon is shown for k_t=2 specimen in Figure 5.8 and Figure 5.9 and for a k_t=3 specimen in Figure 5.10.

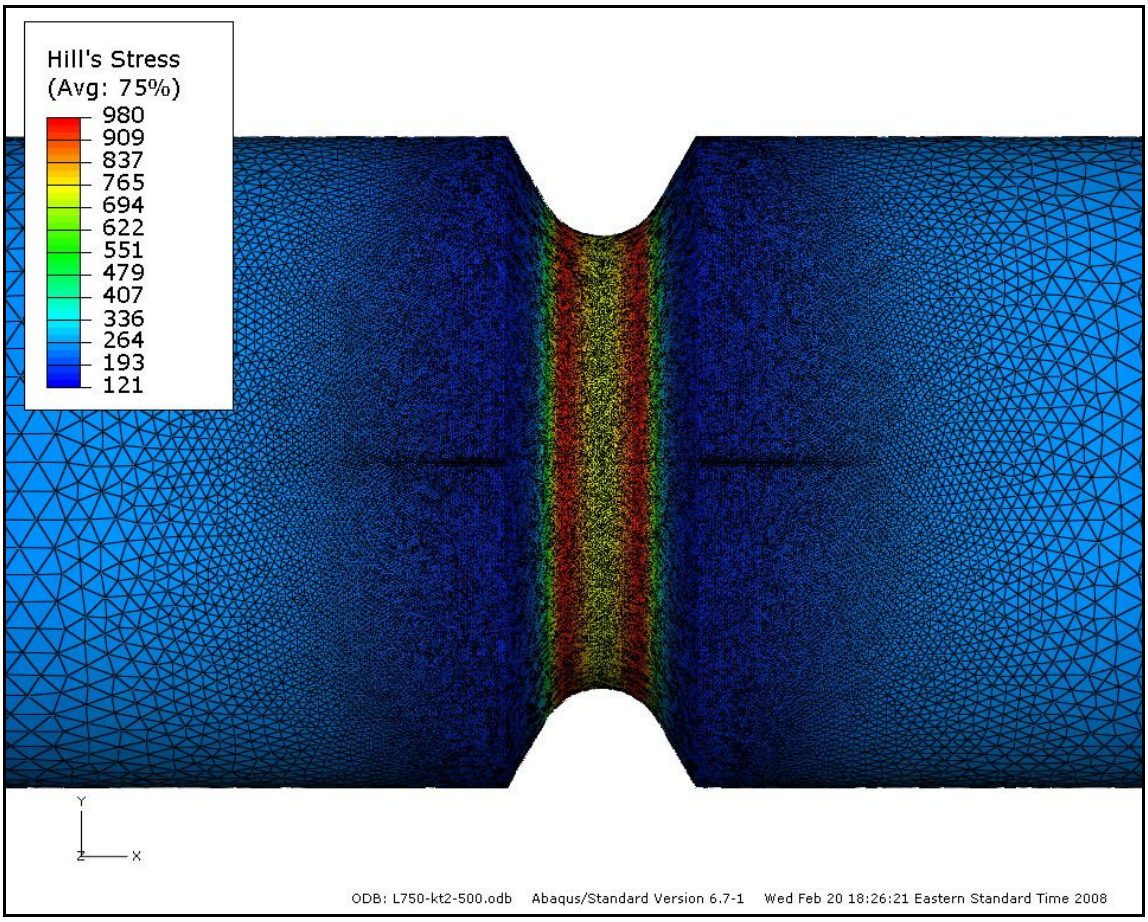

Figure 5.8: *Hill's stress in L750 k_t=2 specimen from an elastic anisotropic FEA.*

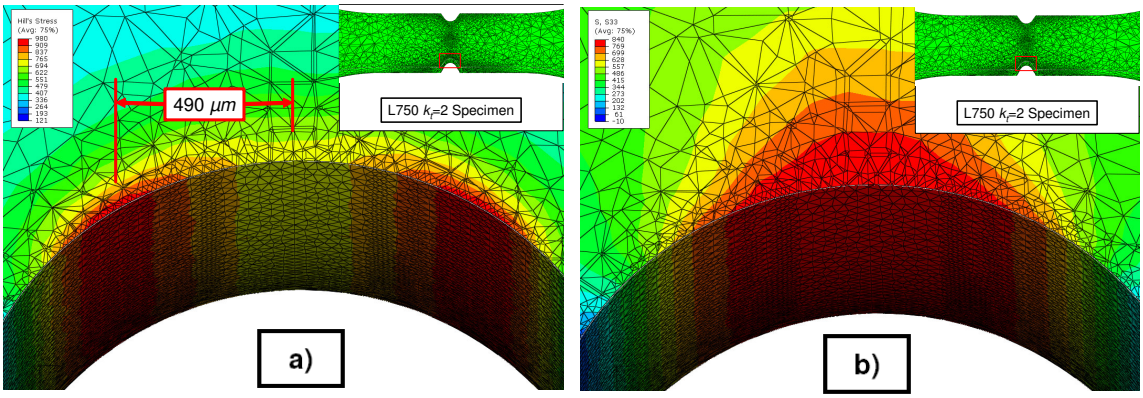

Figure 5.9: *Anisotropic elastic FEA of L750 k_t=2 specimen showing a) Hill's equivalent stress and b) S_{33} stress.*

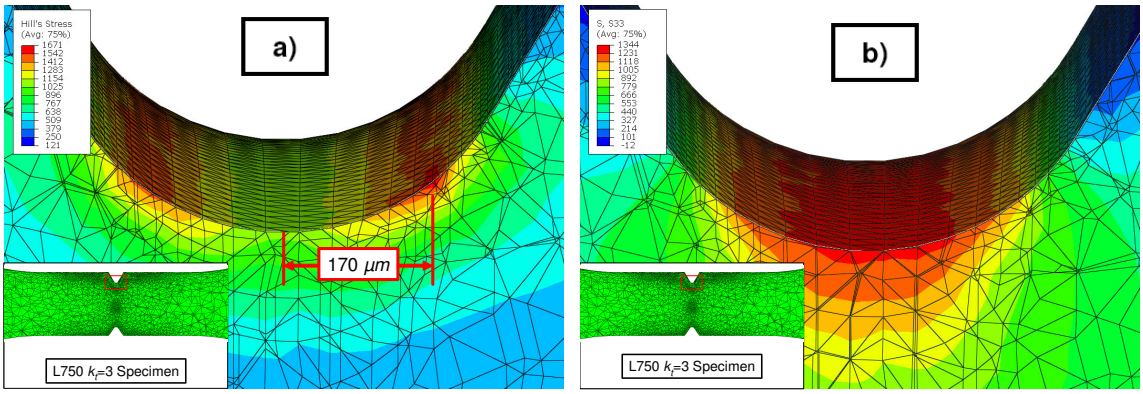

Figure 5.10: *Anisotropic elastic FEA of L50 k_t=3 specimen showing a) Hill's equivalent stress and b) S_{11} stress.*

The multiaxial Neuber-based model recognizes areas of highest Hill's equivalent stress as critical regions. The elastic analysis has shown that these critical regions are outside the root of the notch. When performing fatigue analysis, these critical regions must be considered as likely crack initiation locations. Microscopy results discussed in Section 4.4 show that cracks form at regions of high Hill's stress demonstrated by elastic FEA simulations. Table 5.3 lists the maximum normal stress, von Mises' stress, and Hill's stress based on the linear anisotropic elastic simulations. For three-dimensional problems, in general the stress concentration factors will change with different materials because the Poisson's ratio is often involved in three-dimensional stress analysis [17]. For this reason k_t is not based on isotropic properties but on anisotropic elastic maximum normal stress (i.e., S_{11} for T simulations and S_{33} for L simulations) and net section nominal stress.

Table 5.3: *Maximum normal, von Mises', and Hill's stress of the linear anisotropic elastic simulations.*

Test Specimen			Max Stress Normalized by Net Section Stress		
Temp (^oC)	Notch Type	Orient.	Max Normal Stress	Max VM's Stress	Max Hill's Stress
750	k_t=2	L	1.68	1.72	1.96
		T	2.18	1.90	2.44
	k_t=3	L	2.69	2.89	3.34
		T	3.41	2.82	3.57
950	k_t=2	L	1.66	1.72	1.97
		T	2.18	1.90	1.93
	k_t=3	L	2.65	2.90	3.37
		T	3.41	2.83	3.23

5.3 Multiaxial Neuber Model Results

Uniaxial Neuber results, shown in Figure 5.11 to Figure 5.13, are used as the baseline notch lifing method. The uniaxial Neuber approach (Eq. 2.16) and a uniaxial Ramberg-Osgood relationship (Eq. 2.17) are used but with a k_t based on the maximum normal stress from anisotropic elastic analysis shown in Table 5.3. The modified Coffin-Manson relationship (Eq. 4.1) is then used to predict life. Material and life parameters are based on the loading direction (i.e., predictions for T specimens use material and life parameters based on T properties). This method gives highly conservative results. T life predictions are more conservative than the L predictions because decreased notch sensitivity of T specimens shown in Figure 4.13.

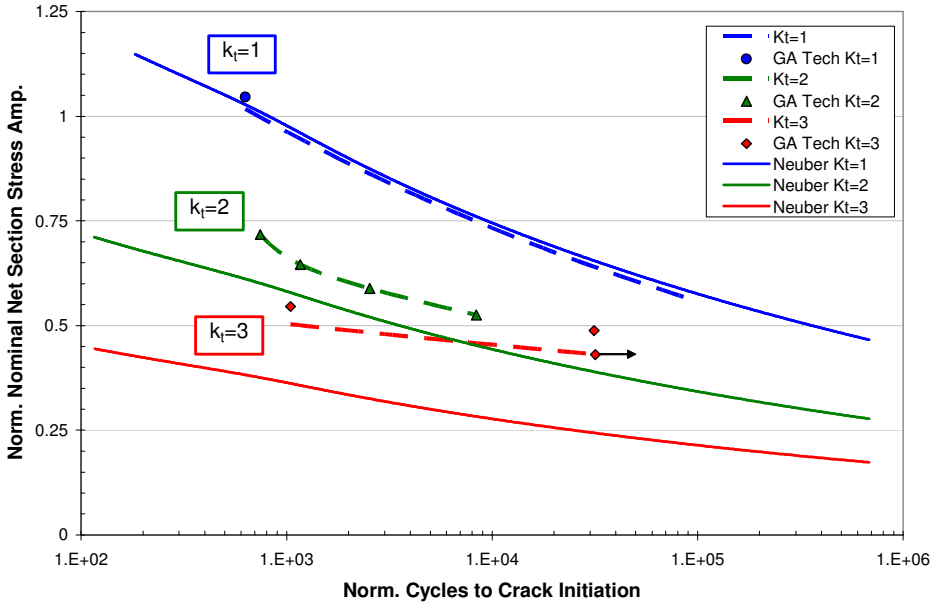

Figure 5.11: *L750 uniaxial Neuber model results.*

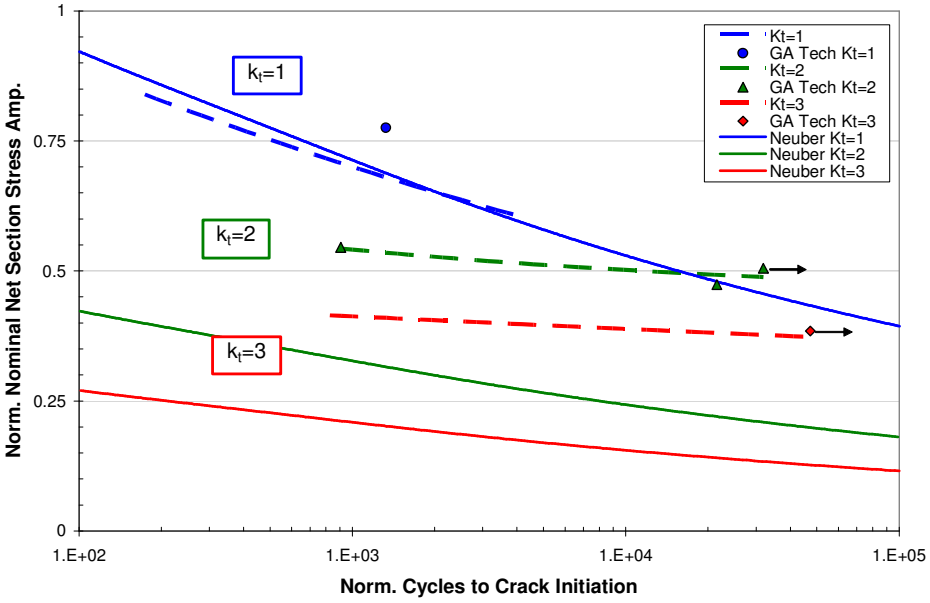

Figure 5.12: *T750 uniaxial Neuber model results.*

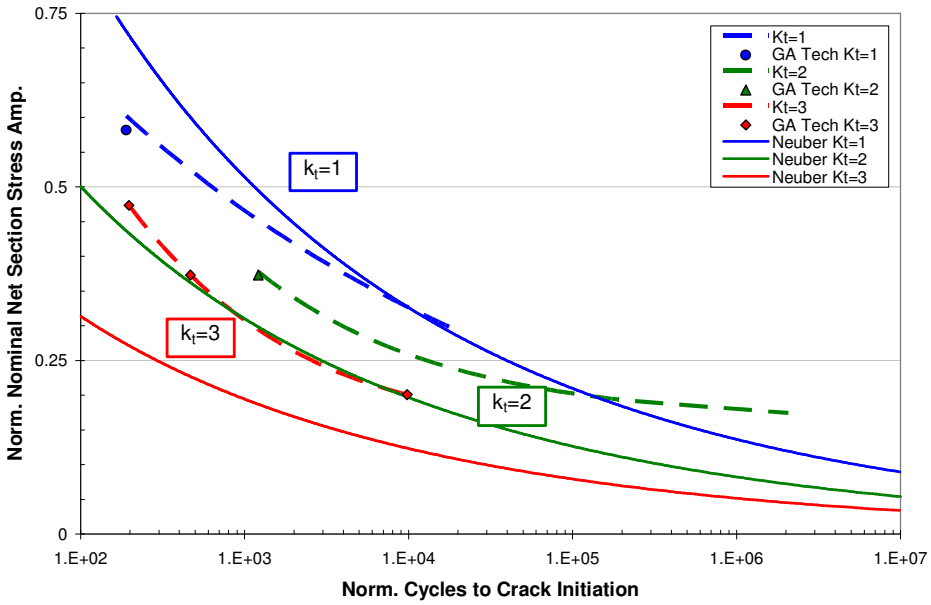

Figure 5.13: *L950 uniaxial Neuber model results.*

Multiaxial Neuber-based model (MNM) results are shown in Figure 5.14 to Figure 5.16. Using a non-local method gives less conservative results. Life predictions in the L direction are good for shorter lives but become overly conservative at long lives. The reduced notch effect at higher cycles is under predicted by the MNM approach. In the T orientation, the MNM fails to follow the flat *S-N* trends observed in experiments. At 950°*C*, the MNM predicts the life well until 10^4-10^5 *cycles*, where predictions become overly conservative. This is the same behavior observed in L750 MNM predictions. The non-local critical distance approach successfully predicted the size effect of k_t=2 and k_t=3 notches. A length scale of 200 μm was used for both L750 and L950 tests. This length scale successfully accounts for the notch size effect in k_t=2 and k_t=3 notches. Point method and line method techniques produced nearly identical results. This length scale is 22% ρ for the k_t=2 notch and 63% ρ for the k_t=3 notch and is 40% the grain size. The

length scale was chosen by fitting the non-local life predictions to experimental data. The resulting length scales were larger than the methods described in Section 2.4 predict. A larger length scale of 250 μm was used for T750. This was necessary to account for the reduced notch effect observed in the T experimental results and avoid overly conservative predictions. This increased length scale accounts for the differences in k_t=2 and k_t=3 notches. The model does not predict the flat *S-N* curves observed in T oriented tests.

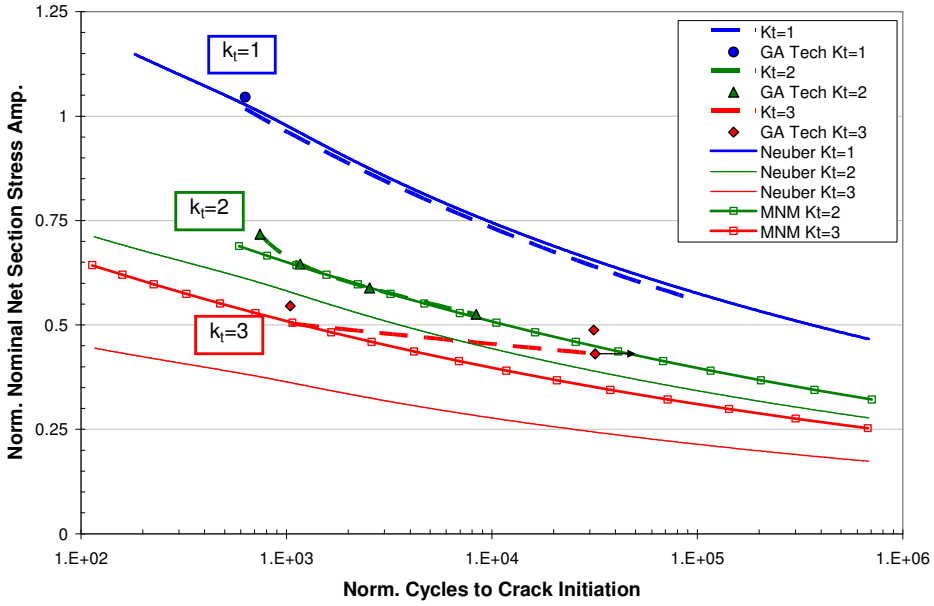

Figure 5.14: *L750 MNM results.*

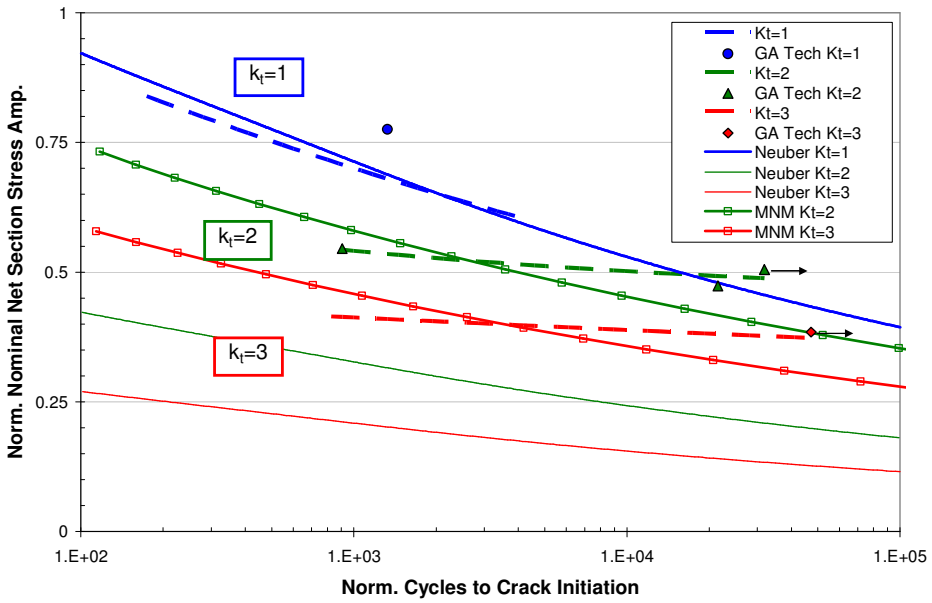

Figure 5.15: *T750 MNM results.*

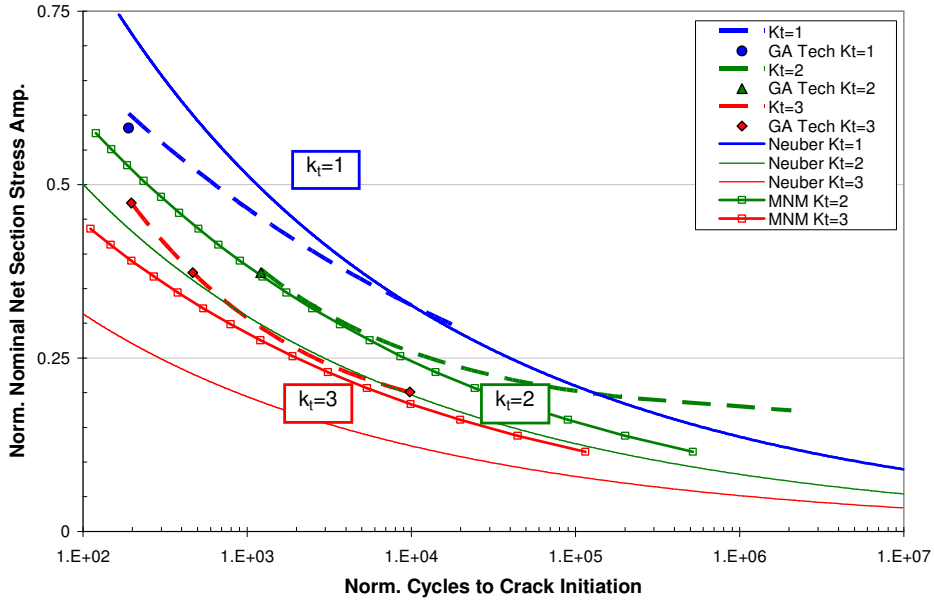

Figure 5.16: *L950 MNM results.*

5.4 Time-dependent Neuber Model Results

The MNM incorporates rate dependence by using rate-dependent material parameters. The effect of dwells is modeling by simulating the hold cycle as a SSR continuous cycle. This will capture the mean stress and strain behavior as a result of the dwell without explicitly modeling creep. In other words, the effect of dwells is approximated by continuous loading at different rates. Much of the dwell effects seen at $750°C$ and $950°C$ can be accounted for by the development of mean stress. Figure 5.17 demonstrates how rate-dependent consideration can predict the mean stress development of a dwell. Using the SWT parameter, the model will not predict any change in life due to rate effects. This is because even though at slower rates the stress-strain response is different, the Neuber approach will predict a solution with the same $\sigma\varepsilon$, which coincidentally corresponds to the same SWT when the mean stress is zero. To better capture the effects of mean stress and rate, the Walker parameter can be used,

$$\sigma_{\max}^{1-\gamma}\varepsilon_a^{\gamma} \tag{5.37}$$

where γ is fit to experimental data. This allows the weight of the maximum stress and strain amplitude components to be varied. When γ is ½, the Walker equation reduces to the SWT parameter. For the purpose of this study, SWT will be used to avoid the complexity of another fitting parameter.

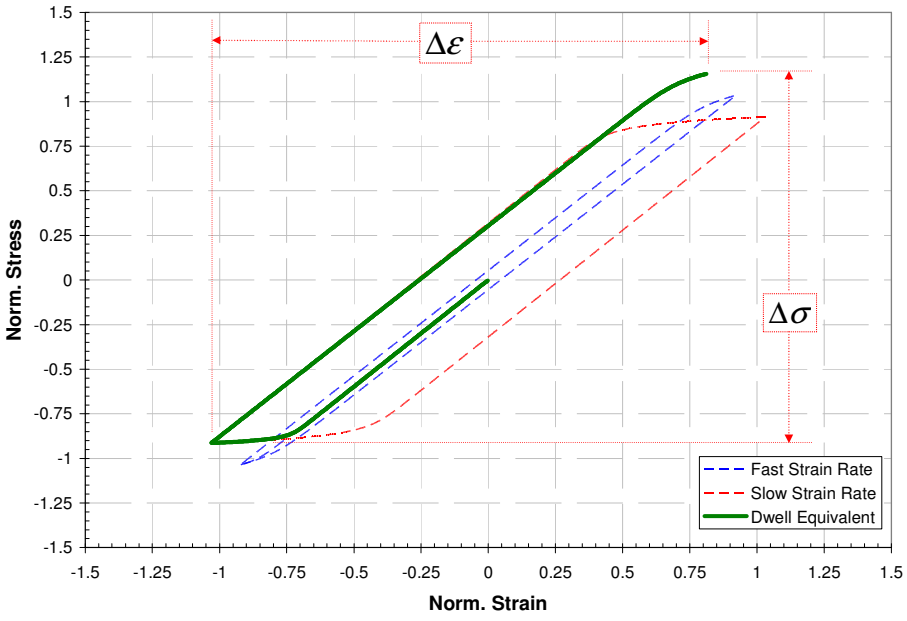

Figure 5.17: *Method for simulating a dwell in the MNM.*

Life predictions for L750 are shown in Figure 5.18. For L750 notched dwells, the analytical model successfully predicts the effects of mean stress and resulting reduction in life. Dwell results for T750 are shown in Figure 5.19. In the T orientation the model predicts a negligible effect of the dwell. This is because in the T orientation there is very little cyclic plastic deformation (i.e., very little hysteresis), so dwell effects would only be predicted by the model at very short lives. At 950°*C*, the effects of creep are more significant. The model, because it does not explicitly account for creep damage, under predicts the reduction in life due to the dwell as shown in Figure 5.20.

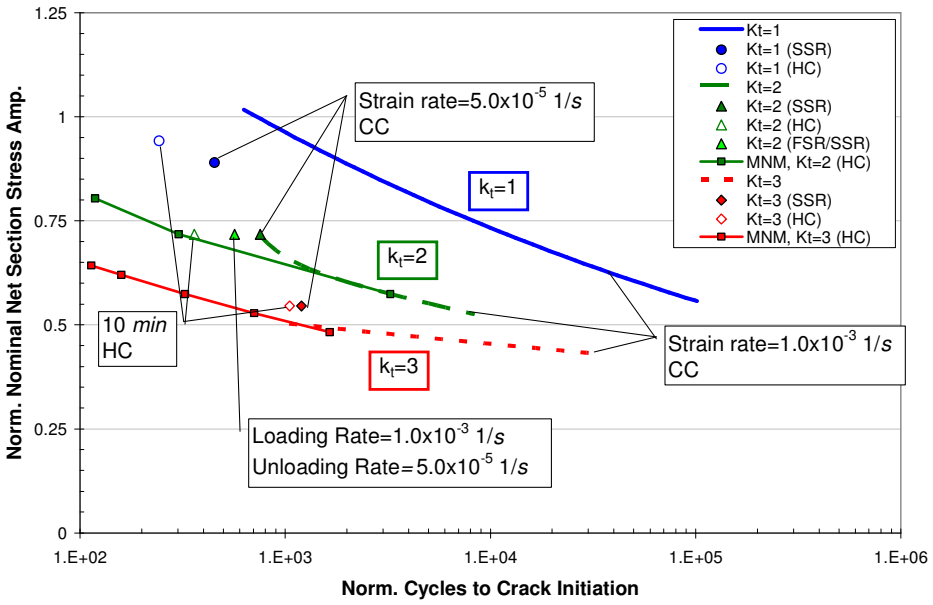

Figure 5.18: *L750 MNM dwell results.*

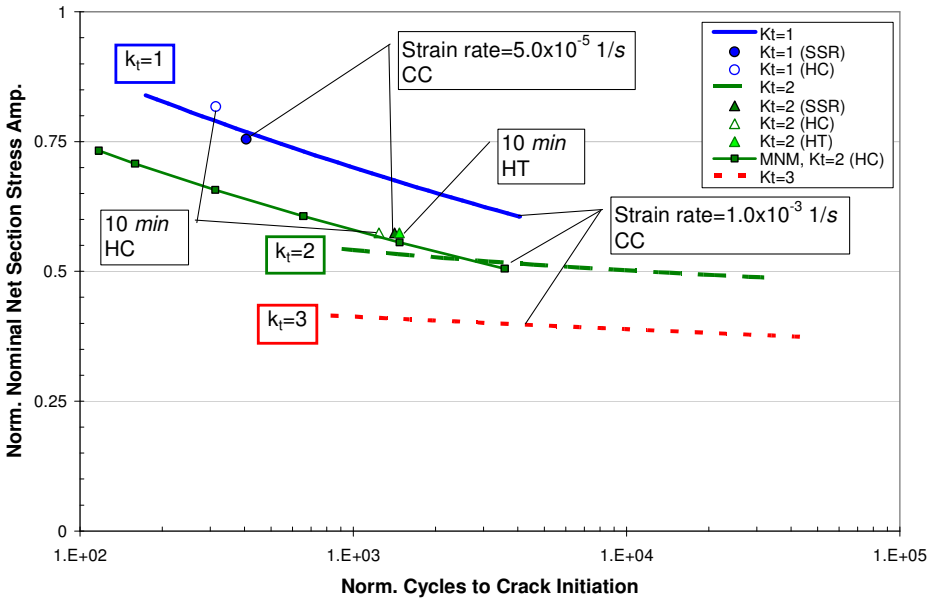

Figure 5.19: *T750 MNM dwell results.*

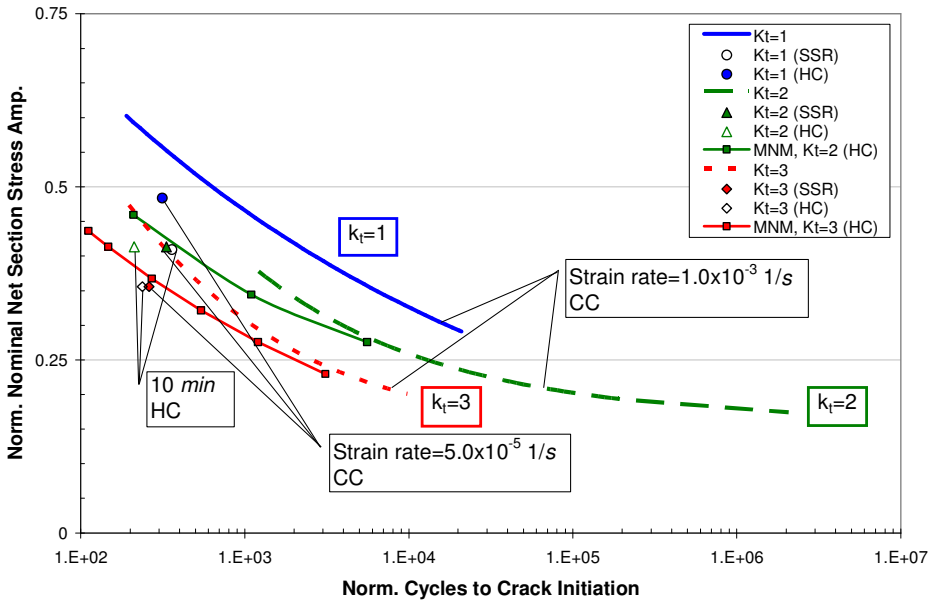

Figure 5.20: *L950 MNM dwell results.*

CHAPTER 6

COMPUTATIONAL MODELING

Multiple types of numerical simulation were necessary to develop and validate the analytical model. Anisotropic elastic modeling was necessary to obtain the necessary input for the multiaxial Neuber-based model and to characterize the stress concentrations. The multiaxial Neuber model modifies the simple linear elastic response at the notch to incorporate the effects of plasticity. Elastic-plastic modeling is necessary to fully assess the stress-strain response at the notch and determine the effect of time-dependent mechanisms. All of these approaches must consider orientation effects.

It is impractical to instrument the stress concentration to adequately measure the local notch response. Instead, a series of computational simulations are employed to study the stress-strain response in the presence of a stress concentration. An accurate constitutive model calibrated to the material characteristics was used to simulate the response.

To capture the effects of crystal orientation on notch visco-plasticity and time-dependent phenomenon, a crystal visco-plasticity (CVP) model developed by Shenoy et al. [16] was used. This constitutive model can account for the effects of microstructure, including the slip activity controlled by crystalline orientation. Shenoy et al. developed the constitutive model for the study of DS GTD-111, a similar DS alloy.

6.1 Crystal Plasticity Model

A crystal visco-plasticity (CVP) model is used because it includes the effects of elasticity, plasticity, and time-dependent effects. A crystal plasticity model is needed because it can more accurately account for the crystallographic orientation dependence on slip. There is no easy way to experimentally record the response in the neighborhood of the notch, instead a series of simulations will approximate the phenomenon occurring at the stress concentration and help explain experimental results and identify the limitations of the simplified analytical model.

The crystal plasticity framework was reviewed in Chapter 2. This constitutive model developed by Shenoy et al. [16] has been implemented in ABAQUS/Analysis [46] as a user-defined material subroutine (UMAT). The UMAT implemented by Shenoy was based upon the scheme used by McGinty [52]. For each integration point at each time step increment, the UMAT updates stresses, internal state variable (ISVs), and the Jacobian matrix.

All crystal plasticity simulations were modeled with three-dimensional, linear, solid elements. Eight-noded hexahedral elements were used outside of the notch and 4-noded tetrahedral elements were used inside the notch designated C3D8R and C3D4 by ABAQUS, respectively. The finite element mesh is shown in Figure 6.1. A different mesh was used for the crystal plasticity simulations to limit the number of elements to less than 100,000 because of the computational complexity of the model. The material behavior of the elements inside the notch was modeled by crystal plasticity whereas the regions outside of the notch were modeled as anisotropic elastic. The simulations in L direction were performed as a single crystal (i.e., one grain). The symmetry of specimens

allows for this single crystal simulation to represent a columnar grain anywhere at the surface of the notch. It is the response near the notch root that is of primary interest. The orientation of the grains relative to the stress axis is described using three parameters known as Euler angles, which are designated by (φ, θ, ψ). Smooth specimen simulations were performed in displacement control which simulates uniaxial strain-controlled experiments. Notched specimens were performed under a distributed force control which simulates uniaxial force-controlled experiments.

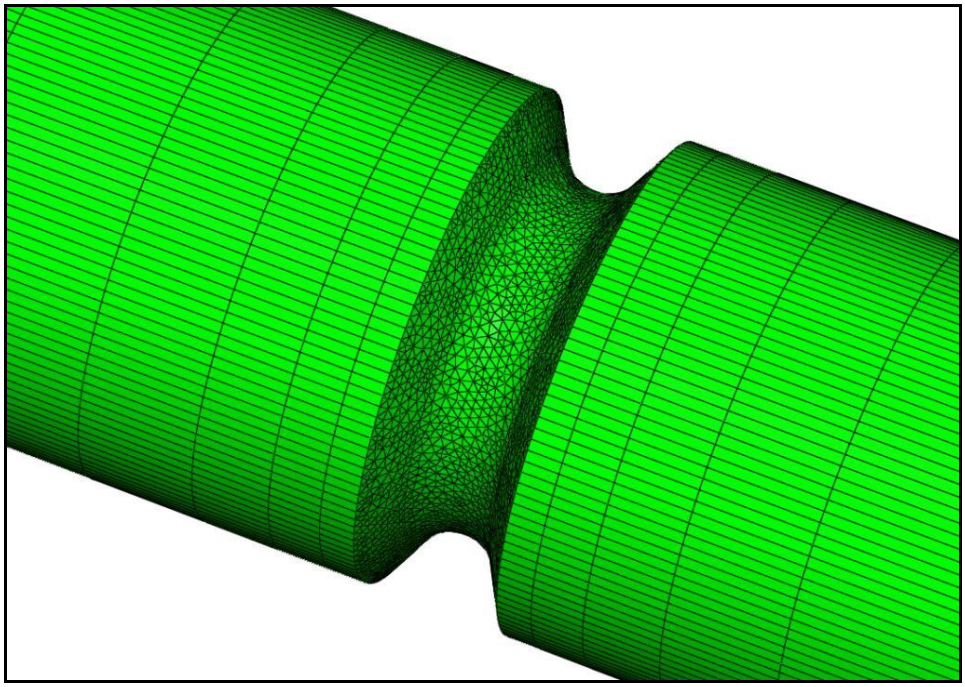

Figure 6.1: *CVP finite element mesh.*

The simulations were performed using DS GTD-111 material constants. These material constants have been previously determined by Shenoy using an automated optimization scheme involving a myriad of experimental data including isothermal LCF, creep-fatigue, and creep deformation. This technique is discussed in great detail by

Shenoy [53] and Gordon [1]. The crystal plasticity simulation results are compared to experimental data in Figure 6.2 to demonstrate how well the crystal plasticity model captures the material response. These temperatures were used because material parameters were only available for certain discrete temperatures. The crystal plasticity material parameters for temperatures 760°*C*, 871°*C*, and 982°*C* are given in Table 6.1.

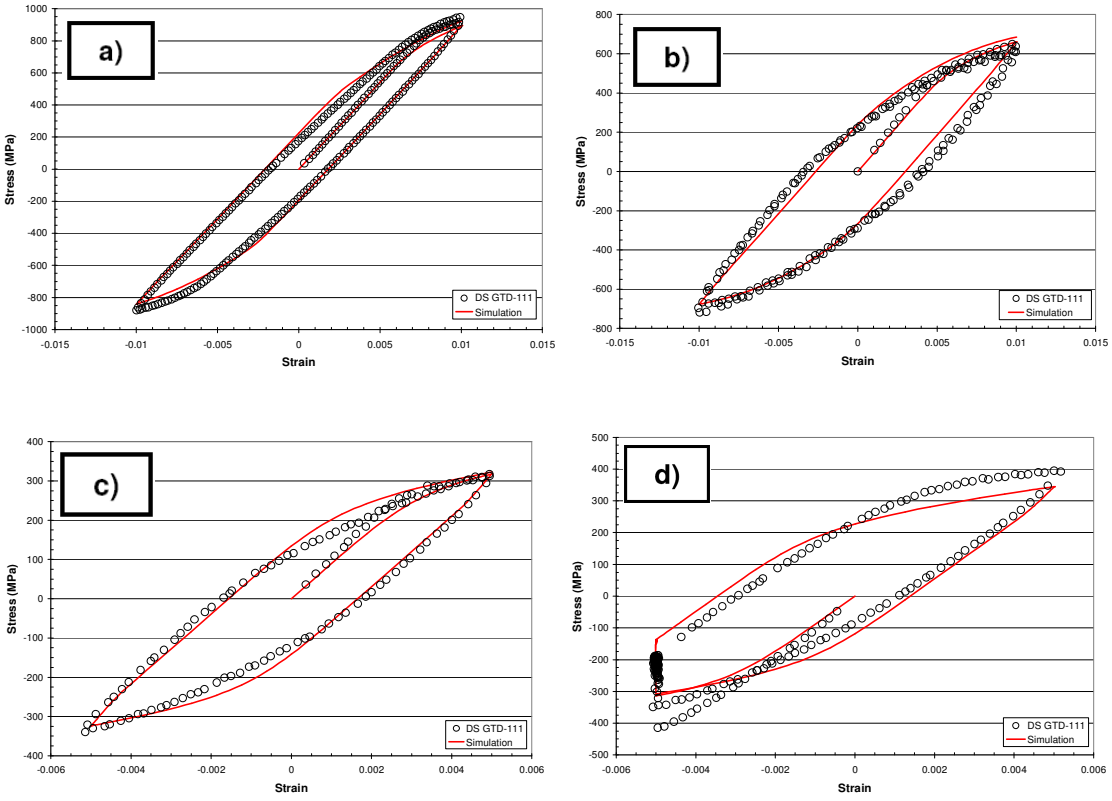

Figure 6.2: *Comparison of experimental and simulation results for DS GTD-111 a) L760, b) L871, c) L982, and d) L982 with HC.*

Table 6.1: *Material parameters for DS GTD-111 [16].*

	Material Parameter	760°C	871°C	982°C
Common Constants	C_{11} (MPa)	151690	138830	134450
	C_{12} (MPa)	70329	69980	67770
	C_{44} (MPa)	125750	120360	113880
	n	5	4	4
	B_0	0.05	0.05	0.05
	μ (MPa)	125750	120360	113880
	h_{pe}	0.15	0	0
	h_{cb}	0.1	0	0
	h_{se}	-0.03	0	0
	Q_0 (KJ/mol)	309	309	309
	R (J/mol K)	8.314	8.314	8.314
	μ_0 (MPa)	166000	166000	166000
	$\dot{\gamma}_0 (s^{-1})$	$1.15\text{x}10^9$	$1.15\text{x}10^9$	$1.15\text{x}10^9$
	κ_{th} (MPa)	0	0	0
	D_0 (MPa)	102	102	102
Octahedral Slip System Constants	h_χ (MPa)	186165	137900	41370
	R_χ (MPa)	148	92	69
	$h_{\chi S}$	2.37x10-7	7.77x10-8	-
	$r_{\chi S}$	1	1	-
	κ_0^α (MPa)	148	70	14
	h_0 (MPa)	0	0	0
	$h_{\kappa S}$	0	0	0
	h_s	-	-	-
	r_s	-	-	-
	$q^{\alpha\beta}$	-	-	-
Cube Slip System Constants	h_χ (MPa)	-	172400	55160
	R_γ (MPa)	-	81.2	54.5
	$h_{\chi S}$	-	7.77x10-8	-
	$r_{\chi S}$	-	1	-
	$\kappa_0^\alpha(T)$ (MPa)	-	64.2	11
	h_0 (MPa)	-	0	0
	$h_{\kappa S}$	-	0	0
	h_s	-	-	-
	r_s	-	-	-
	$q^{\alpha\beta}$	-	-	-

Cyclic loading simulations were performed on k_t=2 and k_t=3 notches at both 760°*C* and 982°*C*. These conditions most closely simulate the experimental test

conditions for CM247LC DS. Stress-strain hysteresis response was taken for three cycles at the root of the notch. As shown in Figure 6.3, under continuously cycling conditions, the stress-strain hysteresis is immediately stabilized which agrees with the limited softening of CM247LC DS observed in experiments. The effect of a hold in compression (HC) is shown in Figure 6.4a. The hold generates a compressive mean strain but no mean stress. During the dwell the plastic zone of the notch experiences a combination of force and displacement control. This is evidenced by simultaneous stress and strain relaxation. The Neuber approach assumes constrained plasticity, where the plastic zone is constrained in a much larger elastic region. The larger elastic zone dictates the displacement of the plastic zone; therefore it is common to assume that the highly stressed material at a stress concentration is experiencing displacement control. Creep within the plastic zone redistributes the local stresses and strains resulting in a hybrid force-displacement control scenario. The effects of a tensile dwell produce the same effect as seen with the compressive dwell. As shown in Figure 6.4b, the hold in tension (HT) produces a tensile mean strain but no mean stress. The dwell behavior at the notch root can be described as a combination of force and displacement control and produces ratcheting in the tensile direction. A CVP simulation of a k_t=2 specimen at 982°*C* with a dwell, shown in Figure 6.5, predicts the global creep ratcheting observed experimentally in Figure 4.26a.

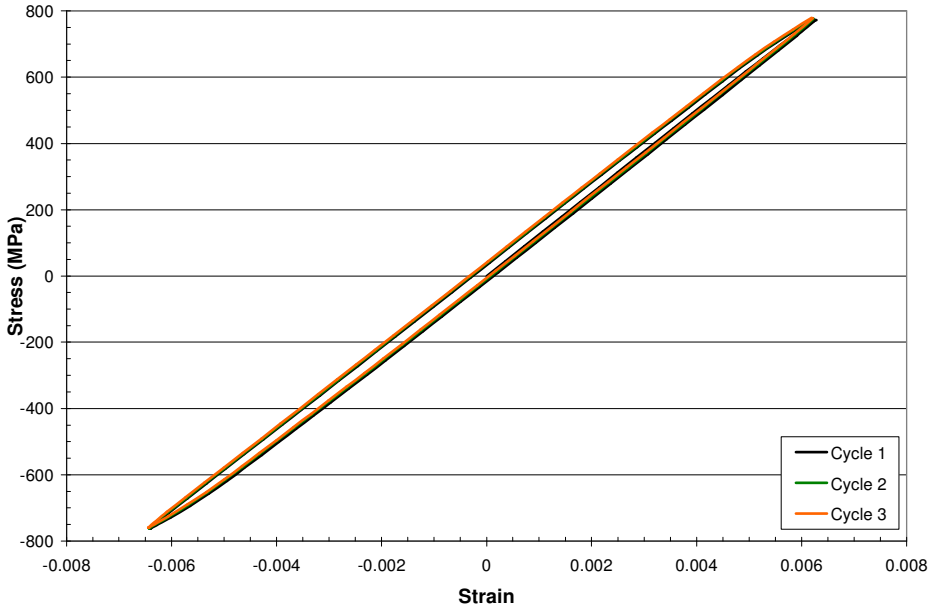

Figure 6.3: *CVP stress-strain response at notch root of L760 GTD-111 k_t=2 in [100] direction.*

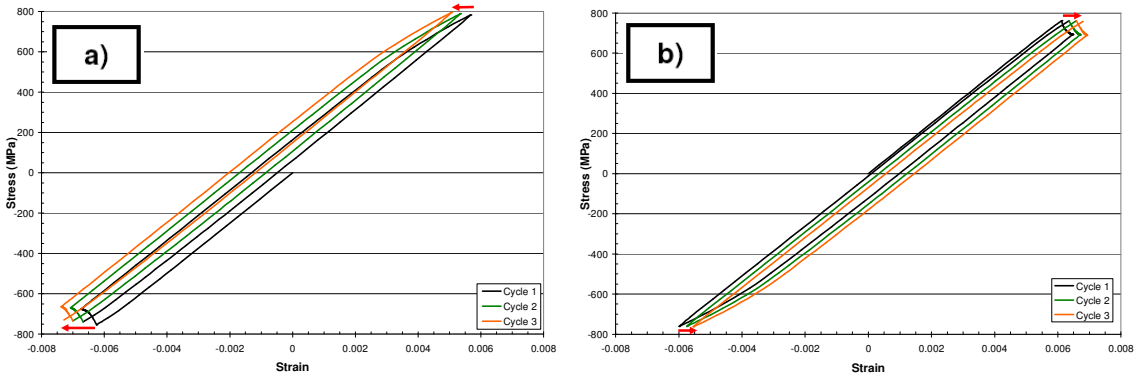

Figure 6.4: *CVP stress-strain response at notch root of L760 GTD-111 k_t=2 in [100] direction with a) HC and b) HT.*

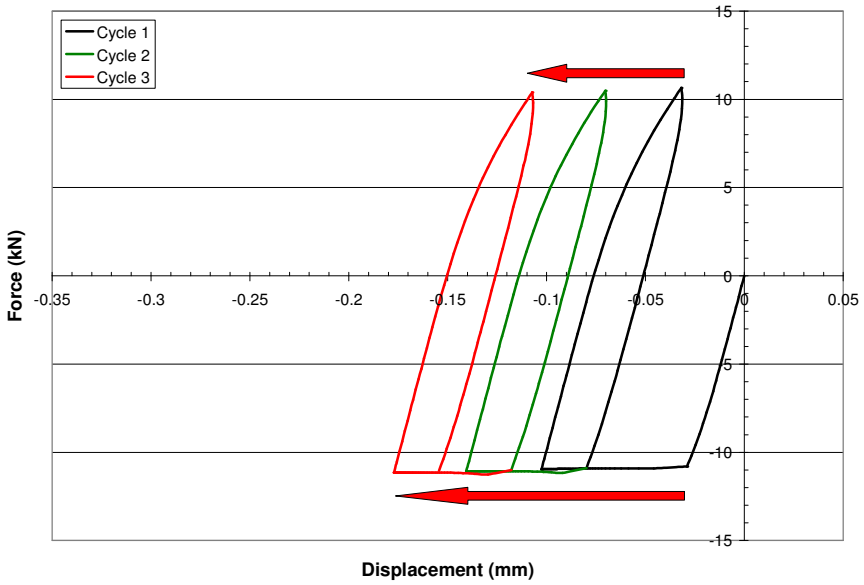

Figure 6.5: *Creep ratcheting of a L982 GTD-111 k_t=2 HC CVP simulation.*

Figure 6.6 describes the effect of the compressive hold on stress behavior across the notch net-section. Stress redistribution occurs during the dwell and is shown to stabilize after two cycles. In Figure 6.6, "Before HC" represents the stresses at the beginning of the dwell and "After HC" represent the stresses at the end of the dwell.

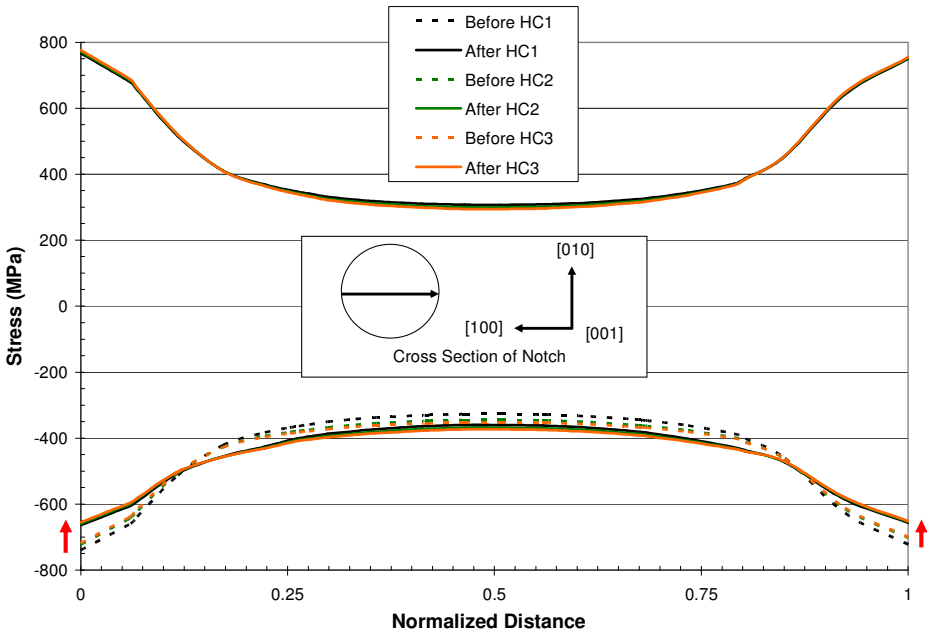

Figure 6.6: *CVP stress across the notch net-section of L760 GTD-111 k_t=2 with HC.*

Accumulated plastic strain was the metric used to determine the hot spots of the crystal plasticity simulation of the notch. Plastic strain is an important driver for fatigue and can be used to qualitatively illustrate the critical regions of the notch. Figure 6.7 shows the hot spots at the notch of the single crystal plasticity simulation for a k_t=2 specimen. The areas exhibiting the greatest amount of plastic deformation are away from the notch root in the <110> orientations. This is where the single crystal is stiffest but also has a lower yield strength. This single crystal simulation is very useful because it shows the effect of crystal orientation in the presence of a stress concentration. DS superalloys are macroscopically considered transversely isotropic but the columnar grains are large and crystal orientation will have an effect on small notches since fatigue cracks will often form in a single grain.

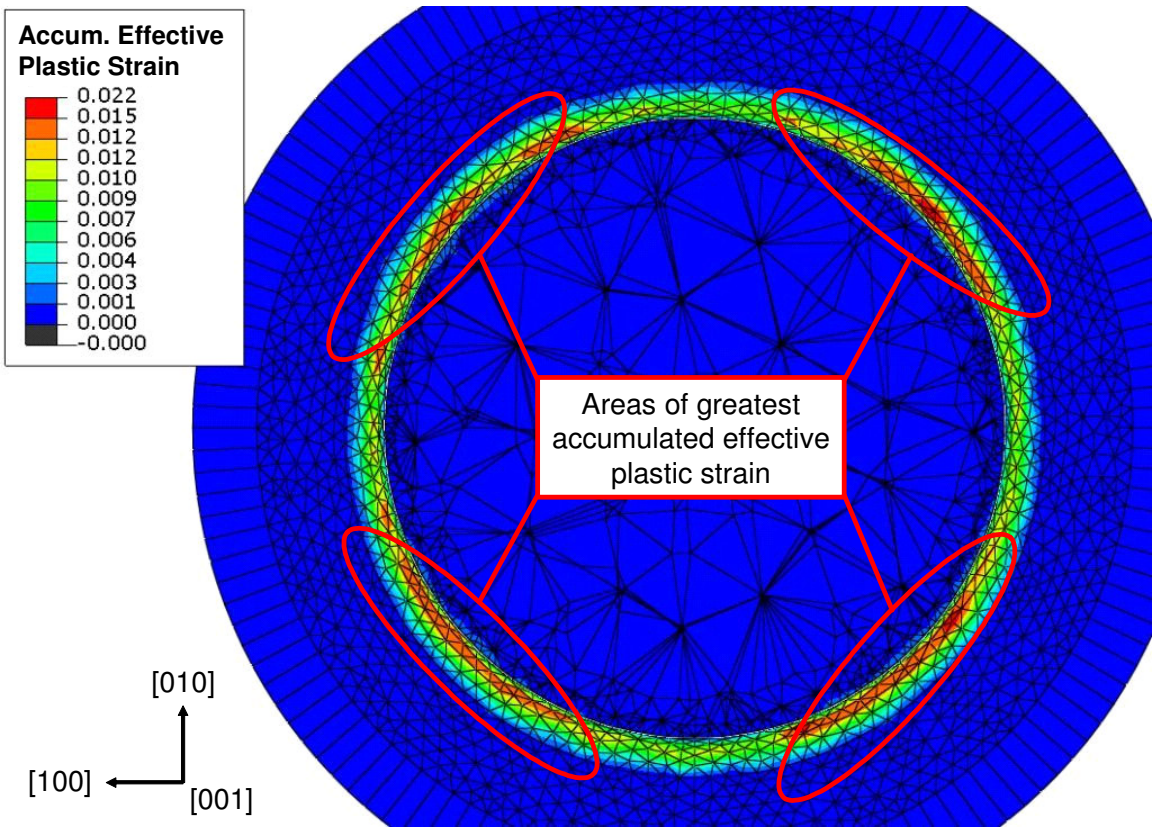

Figure 6.7: *CVP accumulated effective plastic strain for L760 GTD-111 k_t=2 under a net-section nominal stress of 500 MPa.*

When compared to the multiaxial Neuber model (MNM) solution as shown in Figure 6.8, the CVP approach predicts more plasticity and reduced stress levels. The CVP simulation captures the effects of slip on each slip plane which results in more sensitivity and yielding at lower stress levels. The multiaxial Neuber model detects yielding only when the Hill's stress reaches a critical value. The MNM also predicts that yielding proportionally reduces the elastic solution's stress state (i.e., S_{11}, S_{22}, etc. are all reduced by the same percentage in the presence of plastic deformation). The CVP solution predicts that plastic deformation has a greater effect on stress components of small magnitude. The CVP solution's S_{22} does not go to zero because mesh refinement

does not capture the sharp stress gradient. The stresses are highest in the <110> direction. This demonstrates the stress disparities that can develop in individual grains. Similarly, Figure 6.9 shows that the accumulated effective plastic strain is much greater in the <110> direction when compared to the <010> direction. This is congruous with the findings shown Figure 6.7. The plastic strain and stress gradients observed in the single crystal have implications regarding the importance of relationship between crack initiation locations and favorably oriented grains.

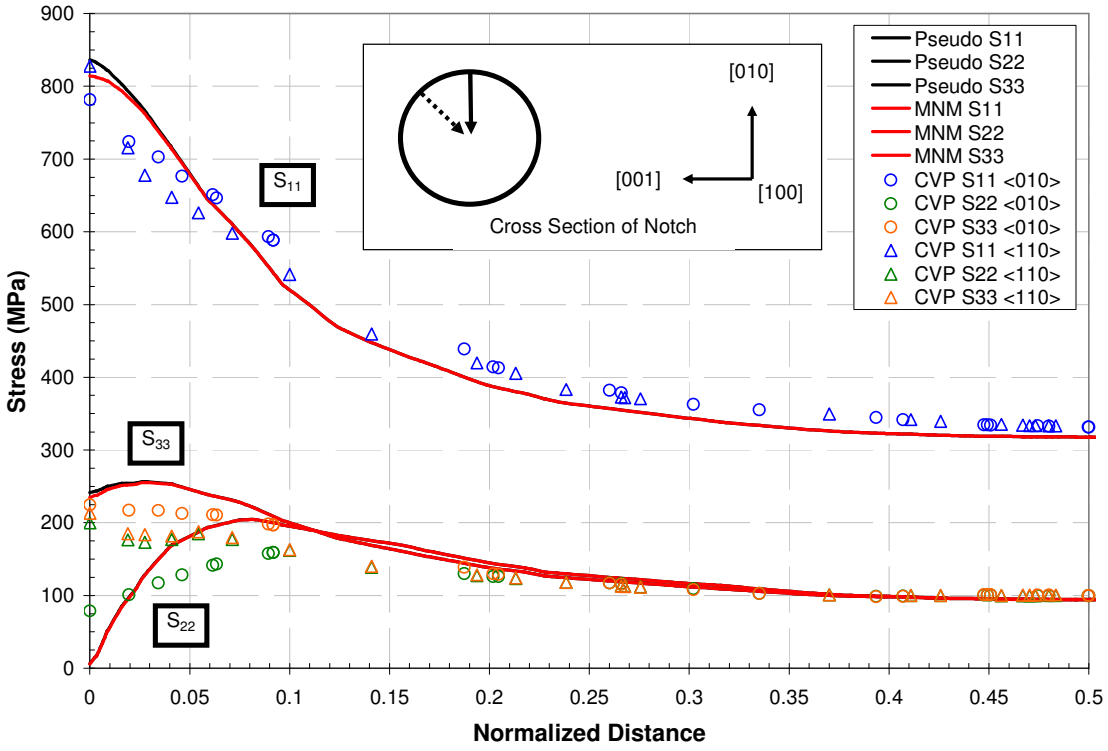

Figure 6.8: *Elastic, CVP, and MNM solution comparison of L760 k_t=2 notch stress profiles across the net-section under a nominal stress of 500 MPa.*

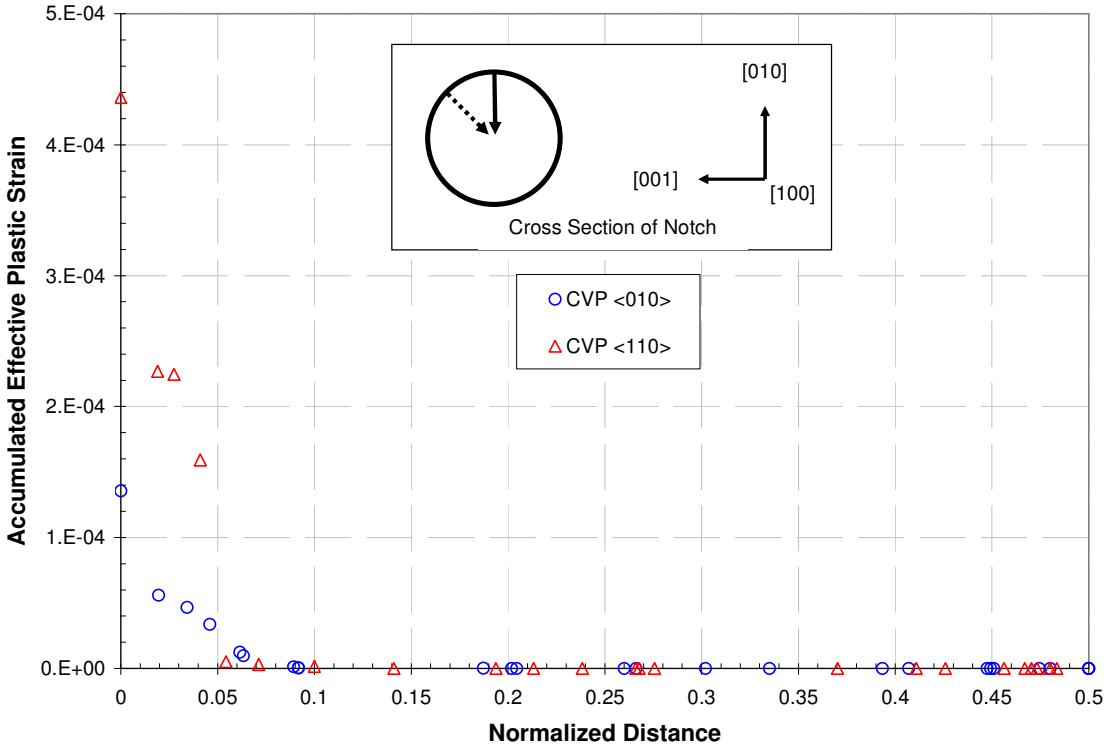

Figure 6.9: *L760 k_t=2 CVP simulation's accumulated effective plastic strain profiles across the notch net-section under a nominal stress of 500 MPa.*

CHAPTER 7

CONCLUSIONS

Turbine blades endure high temperature LCF in the presence of dwells, stress concentrations, and orientations effects during operation. Experiments were performed that described the effects of the high temperature, rate, dwell, orientation, and stress concentration effects in the DS Ni-base superalloy, CM247LC DS. A simplified analytical life-model was developed to provide stress-strain state and life predictions while considering the effects mentioned above. The model uses a multiaxial Neuber-based approach to incorporate the effects of stress concentrations and anisotropy while the temperature and rate dependence is captured through rate and temperature dependent material parameters. Single crystal CVP simulations were performed to determine the time-dependent response at the notch. These simulations were used to explain experimental results and determine weaknesses of the simplified analytical approach.

The outcomes of this research are as follows:

(1) Performed experiments that define high temperature LCF, notch, and creep-fatigue behavior of CM247LC DS. Experiments were used to simulate the material behavior under a variety of service conditions. The temperatures that were considered were 750°*C* and 950°*C*. Tests were performed on both smooth and notched specimens. Experiments described the effects of orientation, rate, dwells, notches, and temperature on the LCF of CM247LC DS. Some key observations include:

- The transverse orientation had a reduced sensitivity to notches.
- There is a reduced notch effect at higher cycles.

- At 750°*C*, much of the dwell effect can be accounted for by a development of mean stress.
- At 950°*C*, there is more mean stress relaxation when compared to 750°*C* and more creep effects.
- There is more dwell effect on life in the L orientation than the T orientation.
- Global creep ratcheting occurred in the 950°*C* k_t=2 dwell test. This was not observed in any other experiments.

(2) Developed and validated a simplified analytical life model for CM247LC DS. A multiaxial Neuber-based approach was used to predict the 3D stress-strain response in the presence of a stress concentration. Time, orientation, and temperature dependence were implemented by using material and life parameters that were functions of rate, orientation, and temperature. Interpolation of these parameters generalizes the model to a range of temperatures, orientations, and rates. Some key findings include:

- The model makes reasonable life predictions in the L orientation.
- Life predictions become overly conservative at 10^4-10^5 *cycles*.
- In the T orientation, the model does not capture the flat *S-N* behavior observed in experiments.
- The critical distance non-local approach successfully accounted for the notch size effect of both notches.
- A larger characteristic length for the T orientation was necessary to account for the reduced notch sensitivity observed in experiments.
- Modeling a dwell as continuous loading but at different rates accounted for the mean stress development without explicitly considering creep.

(3) Characterized the material and notch response using computational simulations. Single crystal CVP simulations demonstrated the time-dependent response of the notch. Simulations included tensile and compressive holds of notched specimens at multiple temperatures to observe the notch response. The effects of grain orientation were determined from the simulations. Some key findings include:

- The location of maximum Hill's equivalent stress correlates with location of cracks observed in experiments.
- The local notch response is a combination of force and displacement control with some ratcheting.
- A 982°*C* simulation predicts the global creep ratcheting observed in an experiment.
- Simulations showed the highest accumulated effective plastic strains and stresses occur in the <110> directions demonstrating the importance of orientations of favorably oriented grains at the notch surface.

CHAPTER 8

RECOMMENDATIONS

There are several areas of further research that would augment and broaden the context of this study. Listed below are possible future objectives that would further the understanding of high temperature fatigue of DS alloys in the presence of stress concentrations and time-dependent phenomenon.

Determine the Effect of Thermomechanical Fatigue on Notched DS Ni-base Superalloys

All the modeling and experimentation of the present study was isothermal. Future work will include the effects of thermomechanical fatigue (TMF) on smooth and notched CM247LC DS. During the transient regimes of start-up and shut-down operations turbine blades are subjected to TMF. The extension of the analytical model to non-isothermal conditions would improve the robustness of the model. The future study will include three components:

1. Perform in-phase and out-of-phase TMF experiments on smooth and notched CM247LC DS specimens to quantify the non-isothermal fatigue behavior.
2. Extend the multiaxial Neuber-based model to include the effects of TMF.
3. Use non-isothermal computational simulations to explore the effects of TMF on DS Ni-base superalloys.

Conduct Off-axis Experiments of DS Ni-base Superalloys

The multiaxial Neuber-based model developed in this work incorporates the effects of orientation and is capable of predicting the effects of notches for all material directions. Due to limited time and resources, all experiments were performed in L or T orientations only. Future work could include performing tests in alternative orientations

(e.g., 45°, 30°, 60°) and verifying that the model produces adequate life predictions. Off-axis data is needed to fully calibrate the model for all orientations.

Implement Analytical Model into an FEM Post-processor

The life-modeling methodology described in detail in this work is a useful turbine blade design tool. The model needs to be implemented into an FEM post-processor before it can be used for design use. More tests are necessary to fully calibrate the model for all necessary temperature ranges and conditions. With the necessary material parameters known, a post-processor can use the linear elastic FEM results and create an approximate elastic-plastic solution to be used in early design iterations.

Incorporate Improved Creep Functionality into the Model

This work presents a simplified approach to handling rate and dwell effects. Future work could include expanding the capabilities of the model to incorporate an explicit creep term to broaden the functionality of the approach. This type of approach would predict an elastic-plastic-creep solution from a linear elastic input. Under loading scenarios where far-field creep or creep-dominated failure mechanisms are present, this type of approach could improve the accuracy of the life-model.

Determine Success of Model under Multiaxial and Non-Proportional Loading

An extension of the study to include multiaxial and non-proportional loading could broaden the applicability of the model. The model is generalized for multiaxial loading and biaxial notched tests would further validate the predictive capability of the presented approach.

REFERENCES

1. Gordon, A.P., *Crack Initiation Modeling of a Directionally-Solidified Nickel-Base Superalloy*, in *George W. Woodruff School of Mechanical Engineering*. 2006, Georgia Institute of Technology: Atlanta, GA.

2. Mucke, R. and O.-E. Bernhardi, *A constitutive model for anisotropic materials based on Neuber's rule.* Computer Methods in Applied Mechanics and Engineering, 2003. **192**(37-38): p. 4237-4255.

3. Ibanez, A.R., V.S. Srinivasan, and A. Saxena, *Creep deformation and rupture behaviour of directionally solidified GTD 111 superalloy.* Fatigue and Fracture of Engineering Materials and Structures, 2006. **29**(12): p. 1010-1020.

4. Engler-Pinto, C.C., Jr., C. Noseda, M.Y. Nazmy, and F. Rezai-Aria. *Interaction between creep and thermo-mechanical fatigue of CM247LC-DS*. 1996. Champion, PA, USA: TMS.

5. Erickson, G.L. and K. Harris. *DS and SX superalloys for industrial gas turbines*. 1994. Liege, Belg: Kluwer Academic Publishers.

6. Kurz, W. and D.J. Fisher, *Fundamentals of Solidification*. 1998, Switzerland: Trans Tech Publications.

7. Maldini, M., M. Marchionni, M. Nazmy, M. Staubli, and G. Osinkolu. *Creep and fatigue properties of a directionally solidified nickel base superalloy at elevated temperature*. 1996. Champion, PA, USA: TMS.

8. Marchionni, M., G.A. Osinkolu, and M. Maldini, *High temperature cyclic deformation of a directionally solidified Ni-base superalloy.* Fatigue and Fracture of Engineering Materials & Structures, 1996. **19**(8): p. 955-962.

9. Blumm, M., C. Engler-Pinto, F. Meyer-Olbersleben, and F. Rezai-Aria. *Grain orientation and size effects on thermal fatigue behavior of CM247LCDS*. 1994. Liege, Belg: Kluwer Academic Publishers.

10. Erickson, G.L., K. Harris, and R.E. Schwer. *DS CM 247 LC - Characteristic Properties with Optimized Solutioning Techniques*. 1984. Bethesda, MD, USA: Metallurgical Soc of AIME, Warrendale, PA, USA.

11. Erickson, G.L., K. Harris, and R.E. Schwer. *Directionally Solidified DS CM 247 LC - Optimized Mechanical Properties Resulting from Extensive Gamma Prime Solutioning*. 1985. Houston, TX, USA: ASME, New York, NY, USA.

12. Harris, K., *High Ductility Nickel Alloy Directional Casting of Parts for High Temperature and Stress Operation*. 1984, Cannon-Muskegon Corporation: United States Patent No. 4,461,659.

13. Esser, W. *Directional solidification of blades for industrial gas turbines*. 1994. Liege, Belg: Kluwer Academic Publishers.

14. Vasseur, E. and L. Remy, *High temperature low cycle fatigue and thermal-mechanical fatigue behaviour of an oxide-dispersion-strengthened nickel-base superalloy.* Materials Science & Engineering A: Structural Materials: Properties, Microstructure and Processing, 1994. **A184**(1): p. 1-5.

15. Hasebe, T., M. Sakane, and M. Ohnami, *High temperature low cycle fatigue and cyclic constitutive relation of MAR-M247 directionally solidified superalloy.* Journal of Engineering Materials and Technology, Transactions of the ASME, 1992. **114**(2): p. 162-167.

16. Shenoy, M.M., A.P. Gordon, D.L. McDowell, and R.W. Neu, *Thermomechanical fatigue behavior of a directionally solidified Ni-base superalloy.* Journal of Engineering Materials and Technology, Transactions of the ASME, 2005. **127**(3): p. 325-336.

17. Pilkey, W.D., *Peterson's Stress Concentration Factors*. 2nd ed. 1997, New York: John Wiley & Sons, Inc.

18. Peterson, R.E., *Stress-concentration phenomena in fatigue of metals.* American Society of Mechanical Engineers -- Transactions -- Applied Mechanics, 1933. **1**(4): p. 157-167.

19. Dowling, N.E., *Mechanical Behavior of Materials*. 2nd ed. 1999, Upper Saddle River: Prentice Hall.

20. Kuhn, P. and H.F. Hardrath, *Engineering method for estimating notch-size effect in fatigue tests on steel*. 1952, National Advisory Committee for Aeronautics, Washington, DC, United States. p. 35.

21. Neuber, H., *Theory of Stress Concentration for Shear-Strained Prismatical Bodies With Arbitrary Nonlinear Stress-Strain Law.* Journal of Applied Mechanics, 1961. **4**: p. 554-550.

22. Topper, T.H., R.M. Wetzel, and J. Morrow, *Neuber's rule applied to fatigue of notched specimens.* Journal of Materials, 1969. **4**(1): p. 200-209.

23. Molski, K. and G. Glinka, *A method of elastic-plastic stress and strain calculation at a notch root.* Material Science and Engineering, 1981. **50**(1): p. 93-100.

24. Hoffmann, M. and T. Seeger, *Generalized Method for Estimating Multiaxial Elastic-Plastic Notch Stresses and Strains. Part 1: Theory; Part 2: Application*

and General Discussion. Journal of Engineering Materials and Technology, Transactions of the ASME, 1985. **107**(4): p. 250-260.

25. Kottgen, V.B., M.E. Barkey, and D.F. Socie, *Pseudo stress and pseudo strain based approaches to multiaxial notch analysis.* Fatigue and Fracture of Engineering Materials & Structures, 1995. **18**(9): p. 981-1006.

26. Chaudonneret, M., *Calcul de concentrations de contrainte en elastoviscoplasticitè*. 1978, Office Natl d'Etudes et de Recherches Aerospatiales (ONERA): Chatillon, France.

27. Chaudonneret, M. and J.P. Culie, *Adaptation Neuber's theory of for stress concentration in viscoplasticity.* Recherche Aerospatiale, 1985(4): p. 243-50.

28. Kurath, P., *Extension of the local strain fatigue analysis concepts to incorporate time dependent deformation in Ti-6Al-4V at room temperature.* T&AM Report no. 464, The University of Illinois, 1984.

29. Moftakhar, A.A., G. Glinka, D. Scarth, and D. Kawa. *Multiaxial stress-strain creep analysis for notches*. 1994. Miami, FL, USA: ASTM, Philadelphia, PA, USA.

30. Moftakhar, A., A. Buczynski, and G. Glinka, *Calculation of elasto-plastic strains and stresses in notches under multiaxial loading.* International Journal of Fracture, 1994. **70**(4): p. 357-73.

31. Harkegard, G. and S. Sorbo, *Applicability of Neuber's rule to the analysis of stress and strain concentration under creep conditions.* Journal of Engineering Materials and Technology, Transactions of the ASME, 1998. **120**(3): p. 224-229.

32. Nunez, J.E. and G. Glinka, *Analysis of non-localized creep induced strains and stresses in notches.* Engineering Fracture Mechanics, 2004. **71**(12): p. 1791-1803.

33. Norton, F.H., *Creep of Steel at High Temperatures*. 1929, New York: McGraw-Hill.

34. Taylor, D. *The theory of critical distances*. in *Proc. 16th European Conference on Fracture (ECF16)*. 2006. Alexandroupolis, Greece.

35. Neuber, H., *Theory of notch stresses: principles for exact calculation of strength with reference to strutural form and material*. 2 ed. 1958, Berlin: Springer Verlag.

36. Dowling, N.E., *Fatigue at Notches and the Local Strain and Fracture Mechanics Approaches.* ASTM Special Technical Publication, 1979(677): p. 247-273.

37. Susmel, L. and D. Taylor, *A novel formulation of the theory of critical distances to estimate lifetime of notched components in the medium-cycle fatigue regime.*

Fatigue and Fracture of Engineering Materials and Structures, 2007. **30**(7): p. 567-581.

38. Bellett, D., D. Taylor, S. Marco, E. Mazzeo, J. Guillois, and T. Pircher, *The fatigue behaviour of three-dimensional stress concentrations.* International Journal of Fatigue, 2005. **27**(3): p. 207-221.

39. Mucke, R. and H. Kiewel. *Non-local cyclic life prediction for gas turbine components with sharply notched geometries*. 2007. Montreal, Que., Canada: American Society of Mechanical Engineers, New York, NY 10016-5990, United States.

40. Suresh, S., *Fatigue of Materials*. 2nd ed. 1998, Cambridge: Cambridge University Press.

41. Murthy, H., G. Gao, and T.N. Farris, *Fretting fatigue of single crystal nickel at 600 C.* Tribology International, 2006. **39**(10): p. 1227-1240.

42. Naik, R.A., D.P. DeLuca, and D.M. Shah, *Critical plane fatigue modeling and characterization of single crystal nickel superalloys.* Journal of Engineering for Gas Turbines and Power, 2004. **126**(2): p. 391-400.

43. Tjiptowidjojo, Y., C. Przybyla, M. Shenoy, and D. McDowell, *Microstructure-sensitive notch root analysis for Ni-base superalloys.* TMS (The Minerals, Metals & Materials Society), 2007.

44. Shenoy, M.M., R.S. Kumar, and D.L. McDowell, *Modeling effects of nonmetallic inclusions on LCF in DS nickel-base superalloys.* International Journal of Fatigue, 2005. **27**(2): p. 113-127.

45. Shenoy, M.M., D.L. McDowell, and R.W. Neu, *Transversely isotropic viscoplasticity model for a directionally solidified Ni-base superalloy.* International Journal of Plasticity, 2006. **22**(12): p. 2301-2326.

46. *ABAQUS v6.7*. 2007, Dassault Systèmes.

47. *MATLAB R2006a*. 2006, The MathWorks.

48. Lemaitre, J. and J.-L. Chaboche, *Mechanics of solid materials*. 1990: Cambridge University Press.

49. Smith, K.N., P. Watson, and T.H. Topper, *A stress-strain function for the fatigue of metals.* Journal of Materials, 1970. **5**(4): p. 767-78.

50. Bernhardi, O.-E. and R. Muecke, *Lifetime prediction procedure for anisotropic materials.* Communications in Numerical Methods in Engineering, 2000. **16**(8): p. 519-527.

51. Hasebe, T., M. Sakane, and M. Ohnami, *Elastic anisotropy of directionally solidified superalloy.* Journal of Engineering Materials and Technology, Transactions of the ASME, 1992. **114**(2): p. 141-146.

52. McGinty, R.D., *Multiscale Representation of Polycrystalline Inelasticity*. 2001, Georgia Institute of Technology: Atlanta, GA.

53. Shenoy, M.M., *Constitutive Modeling and Life Prediction in Ni-Base Superalloys*, in *George W. Woodruff School of Mechanical Engineering*. 2006, Georgia Institute of Technology: Atlanta, GA.